Radioactive source measurements in a liquid xenon time projection chamber

UNIVERSITY *of the*
WESTERN CAPE

by

Mr. Odwa Azizipho Tyuka

A thesis submitted in conformity with the requirements for
the degree of Master in Physical Science.

in the

Faculty of Science
Department of Physics and Astronomy

Supervisor: Prof. S. Triambak

Co-supervisor: Dr. B.G. Lenardo

November 2024

Declaration

I, Odwa Azizipho Tyuka, declare that this thesis "Radioactive source measurements in a liquid xenon time projection chamber." is my own work, that it has not been submitted before for any degree or assessment at any other university, and that all the sources I have used or quoted have been indicated and acknowledged by means of complete references.

Signature:..... Date: November 2024

To my parents, Nondumiso and Zola Tyuka.

Abstract

Double beta decay is a rare nuclear process that can occur in two different modes. The first is known as the two-neutrino double beta decay, which is a second-order weak interaction process and has already been observed in several nuclei. The second one is called neutrinoless double beta decay. This is a yet-to-be observed lepton number violating process, which can only be described by new physics, not included in the current standard model that describes elementary particles and their interactions. One attractive case for such studies is the double beta decay of ^{136}Xe to ^{136}Ba. Currently there are several international projects under development that aim to observe ^{136}Xe neutrinoless double beta decay. This project aims to contribute to such research with a study of charge-collection energy resolution, with radioactive source measurements in a liquid xenon time projection chamber (TPC).

Acknowledgements

- I would like to thank my supervisor, Smarajit Trimabak, for being a kind and supportive mentor. I will always be grateful for his patience and encouragement.

- I also would like to thank my co-supervisor, Brian Lenardo, and the entire Giorgio Gratta group for their helpful discussions and ideas that made this work possible.

- I am thankful to the nEXO collaboration for giving me the opportunity to grow and learn in this exciting field of research.

- A big thank you to Bernadette Burns and Deep Mukherjee, who were like family to me while I was at Stanford University. Their kindness and care made my time away from home much easier.

- To my office mates, Jespere Calderone Ndzobadila Ondze, Bhivek Singh, Mohamed Kamil, Esmond Craig Vyfers, Enkosi Xolisani Ngwadla, Lwazikazi Maqungo, and Sumeera Gopal, thank you for your friendship and support. You all made the hard days better, and I feel lucky to have worked alongside you.

- I would like to thank my friends for their encouragement and for making my time at University of the Western Cape so enjoyable and memorable.

- I am so grateful to my family, ooMaya namaGiqwa, for always supporting and believing in me. Ndiyabulela ngentliziyo yam yonke.

- While physicists may work with vacuums, we do not work in isolation. My work would not have been possible without the support of all the staff in the Physics department at University of the Western Cape. Thank you all!

- Finally, I would like to thank my father and mother, Zola and Nondumiso Tyuka, for always being there for me. Their love and encouragement have been my biggest source of strength, and I dedicate this work to them.

Contents

Declaration of Authorship i

Abstract iii

Acknowledgements iv

List of Figures vii

List of Tables x

1 Introduction 1
- 1.1 Neutrino properties . . . 2
- 1.2 Neutrino Oscillations . . . 6
- 1.3 Neutrinoless double β decays . . . 8

2 The nEXO experiment 14
- 2.1 Overview . . . 14
- 2.2 TPC working principle . . . 16
- 2.3 Detector design . . . 17
- 2.4 nEXO sensitivity . . . 19

3 Experimental details 22
- 3.1 The Stanford prototype TPC . . . 22
  - 3.1.1 Scintillation channel . . . 25
  - 3.1.2 Ionization channel . . . 26
- 3.2 Radioactive source injection . . . 27
  - 3.2.1 Data collection . . . 30

4 Data analysis and Results 33
- 4.1 Analysis cuts . . . 34
- 4.2 Electron lifetime measurement . . . 38
  - 4.2.1 Charge Reconstruction . . . 39
  - 4.2.2 Noise measurements . . . 41
  - 4.2.3 Energy Resolution . . . 42
- 4.3 Comparison with simulations . . . 42

4.3.1 NEST simulations 43
4.3.2 The *nexo-offline* simulations 44

5 Conclusions and Future work **55**
5.1 Future work 55

A Electron lifetime measurement plots **56**
A.1 Charge energy Spectrum 56

B Noise Measurements **58**

Bibliography **68**

List of Figures

1.1 Energy distribution for β particles emitted from a Radium E source. Figure taken from Ref. [2]. . . . 2
1.2 Two possible arrangements of neutrino masses, the normal and inverted hierarchies. Figure taken from Ref. [14]. . . . 8
1.3 $A = 136$ mass multiplet. As the level structure shows a single β-decay transition from ^{136}Xe to ^{136}Cs is energetically forbidden. However the second-order $\beta\beta$ decay to ^{136}Ba is still allowed. Figure taken from Ref. [20]. 9
1.4 Feynman diagrams for $2\nu\beta\beta$ decay (left-panel) and $0\nu\beta\beta$ decay (right-panel). Figure taken from Ref. [21]. . . . 10
1.5 The $\beta\beta$-decay scheme of ^{136}Xe to ^{136}Ba. . . . 12
1.6 The effective Majorana neutrino mass $\langle m_{\beta\beta}\rangle$ as a function of the lightest neutrino mass m_{light}, based on available mixing angle data. IH stands for inverted hierarchy, while NH stands for the normal mass hierarchy. Figure taken from Ref. [22]. . . . 13

2.1 Conceptual design of the nEXO experiment. Figure taken from Ref. [23]. 14
2.2 A $0\nu\beta\beta$ decay peak relative to the continuous $2\nu\beta\beta$ decay spectrum. Figure taken from Ref. [27]. . . . 15
2.3 A schematic representation of the nEXO TPC, illustrating the photon and charge collection system. The charge collecting tiles gather the ionization electrons at the anode, while the photons are detected by SiPMs positioned at the detector barrel behind the high voltage field rings. Figure taken from Ref [24]. . . . 18
2.4 Left-panel: The relationship between reconstructed charge and light. Events with a high light-to-charge ratio are events that are between the FSR and the TPC vessel, where only scintillation light is detected. These events are removed by the diagonal cut highlighted by the dashed lines. The clear anti-correlation between reconstructed light and charge is evident. Right-panel: The rotated energy, obtained as a linear combination of the charge and light signals, yields an energy resolution $\sigma_E/E \approx 0.8\%$. Figures taken from Ref. [24] . . . 19
2.5 nEXO's projected sensitivity and discovery potential after 10 years of data collection. Figure taken in Ref. [24]. . . . 20
2.6 The sensitivity reach of the nEXO experiment. The horizontal band in the lower-limit arises from a spread in calculated values of the nuclear matrix element (NME) for ^{136}Xe $0\nu\beta\beta$ decay. Figure taken from Ref. [24]. 21

3.1 The cylindrical stainless steel chamber that contains the TPC and the semi-cylindrical copper plate that surrounds the TPC. . . . 23
3.2 The Stanford TPC inside its cylindrical chamber. . . . 24

3.3 The TPC dewar filled with HFE-7000. . . . 25
3.4 Schematic representation of The LXe. Figure taken from Ref. [37]. . . . 26
3.5 SiPMs on the Stanford prototype TPC. . . . 27
3.6 Charge tile section of the Stanford TPC. . . . 28
3.7 Schematic of a prototype charge tile. Figure taken from Ref. [39] . . . 29
3.8 Schematic representation of the charge tile, showing how the strips are grouped together. . . . 30
3.9 Schematic diagram of the ^{220}Rn source installed on the Stanford TPC recirculation system in an isolated loop [40]. . . . 31
3.10 The ^{220}Rn decay chain, highlighting ^{212}Bi to ^{208}Tl decay. Figure taken from Ref. [43]. . . . 31

4.1 The top panel (blue) shows the scintillation output (in ADC units) vs drift time, prior to the application of analysis cuts. The bottom panel (red) show the data after implementation of the cuts. . . . 34
4.2 A 2D histogram of charge energy in ADC units vs drift time. These events arise from BiPo and alpha branch interactions. The dense band below 1000 ADC units are from the alpha branch interactions, as the ionization is localized for such events. The other events are mainly from the BiPo branch. . . . 36
4.3 Final 2D charge-energy histogram after all the analysis cuts have been applied. The dense band below 1000 ADC units will be studied. This band mainly arises from the charge energy detected by the anode. . . . 37
4.4 1D projections for the data corresponding to Fig. 4.3, for different time intervals. . . . 38
4.5 The electron lifetime, τ_e in the Stanford TPC, extracted from the charge tile data shown in Fig. 4.3. . . . 39
4.6 2D Histogram for charge energy vs drift time after correcting for the electron lifetime. As mentioned previously, the band below 2000 ACD units will be studied as these data correspond to 6 MeV α's from the source interacting with LXe. . . . 40
4.7 Projected charge energy spectrum from Fig. 4.6. . . . 40
4.8 Charge energy spectrum for a single channel, with a Gaussian fit to the noise peak at 0 ADC units. . . . 41
4.9 σ_{noise} obtained for each tile strip, also showing the noisy strip X19. . . . 42
4.10 This figure shows the inconsistency between NEST predictions and the experimental data from Aprile *et al.* [46]. On the other hand, our measured value is in reasonable agreement with the NEST results. Our study is limited to a drift field of 400 V/cm, considering its relevance to nEXO's future implementation. . . . 43
4.11 Simulated waveforms from an α energy deposition. Left panel: Without electronic noise. Right panel: With electronic noise added [40]. . . . 45
4.12 Simulated 2D histogram for charge energy vs drift time, after all the analysis cuts are applied. . . . 45
4.13 τ_e determination from the simulated data. . . . 46
4.14 The simulated charge energy spectrum reconstructed using the value for the electron lifetime. These data correspond to 5×10^5 ^{212}Bi decays. . . . 46
4.15 The energy resolution obtained from *nexo-offline* compared with experimental measurements and NEST predictions. . . . 47

4.16 The top panel shows the spectrum of the simulated charge energy when a ^{212}Bi source is simulated in the *nexo-offline* simulation. The bottom panel shows the peak for 6 MeV α's, instead of the ^{212}Bi source. It is clear that the first peak is from the alpha branch. 48
4.17 ^{212}Bi α decay scheme from NuDat3 [56] 49
4.18 Left panel: Individual α and summed α and γ energies used in the NEST simulation. The right peak is from summing with 40 keV γ-rays. Right panel: From the same simulation, ionization electron yields for the α energies, compared with the yields when both α and γ energies are summed together. 50
4.19 The results in Fig. 4.18, with smeared Gaussian widths. 50
4.20 Comparison of NEST generated electron yields shown in Fig. 4.19 and the *nexo-offline* simulated charge for ^{212}Bi decays in LXe. 51
4.21 2D histogram for charge energy vs drift time when the ^{212}Bi source in the *nexo-offline simulation* is replaced with the 6 MeV α particles uniformly distributed inside the TPC. These data are produced after all the analysis cuts have been made, similar to our experimental data. 52
4.22 The reconstructed charge energy spectrum for 6 MeV α's as a source in *nexo-offline* simulations. 52
4.23 Our measured experimental resolution compared with previous measurements and various simulated values. 53
4.24 Zoomed version of Fig. 4.23, in the range $0 - 1$ kV/cm 54

A.1 This figure depicts a Gaussian fit to extract the peak centroid. 56
A.2 This figure depicts a Gaussian fit to extract the peak centroid. 57

B.1 This figure illustrates the charge energy spectrum for a single channel, with a Gaussian fit to the peak, centered at 0 ADC units. 58
B.2 This figure illustrates the charge energy spectrum for a single channel, with a Gaussian fit to the peak, centered at 0 ADC units. 59
B.3 This figure illustrates the charge energy spectrum for a single channel, with a Gaussian fit to the peak, centered at 0 ADC units. 60
B.4 This figure illustrates the charge energy spectrum for a single channel, with a Gaussian fit to the peak, centered at 0 ADC units. 61
B.5 This figure illustrates the charge energy spectrum for a single channel, with a Gaussian fit to the peak, centered at 0 ADC units. 62
B.6 This figure illustrates the charge energy spectrum for a single channel, with a Gaussian fit to the peak, centered at 0 ADC units. 63
B.7 This figure illustrates the charge energy spectrum for a single channel, with a Gaussian fit to the peak, centered at 0 ADC units. 64
B.8 This figure illustrates the charge energy spectrum for a single channel, with a Gaussian fit to the peak, centered at 0 ADC units. 65
B.9 This figure illustrates the charge energy spectrum for a single channel, with a Gaussian fit to the peak, centered at 0 ADC units. 66
B.10 This figure illustrates the charge energy spectrum for a single channel, with a Gaussian fit to the peak, centered at 0 ADC units. 67

List of Tables

1.1 Elementary particles in the SM. The Baryon and Lepton numbers of the corresponding anti-baryons and anti-leptons (their antiparticles) have a negative sign. 1

4.1 Measured parameters to determine the energy resolution for 6 MeV α's in the Stanford LXe TPC. 42
4.2 Measured parameters from the *nexo-offline* simulation data. 48
4.3 Measured parameters from the *nexo-offline* simulations when 6 MeV α's were used. 51

Chapter 1

Introduction

The development of the Standard Model (SM) [1] in the 1970s marked a significant milestone in our understanding of particle physics. At its core, the SM classified elementary particles into groups of spin-1/2 fermions, called quarks and leptons. Present knowledge shows that there exist three generations of quarks and leptons, which are summarized below. In the table below, the neutral leptons (labeled as ν_x, where $x = e, \mu, \tau$) were assumed to be massless in the SM [1], and are known to only interact with matter via weak interactions. Since these particles motivate the work described in this thesis, below I present a brief summary of our present knowledge in neutrino physics.

Leptons				
Generation	Particle	Charge	Baryon number	Lepton number
1^{st}	electron (e^-)	$-e$	0	1
	electron neutrino (ν_e)	0	0	1
2^{nd}	muon (μ^-)	$-e$	0	1
	muon neutrino (ν_μ)	0	0	1
3^{rd}	tau (τ^-)	$-e$	0	1
	tau neutrino (ν_τ)	0	0	1
Quarks				
1^{st}	up (u)	$(2/3)e$	1/3	0
	down (d)	$(-1/3)e$	1/3	0
2^{nd}	charm (c)	$(2/3)e$	1/3	0
	strange (s)	$(-1/3)e$	1/3	0
3^{rd}	top (t)	$(2/3)e$	1/3	0
	bottom (b)	$(-1/3)e$	1/3	0

TABLE 1.1: Elementary particles in the SM. The Baryon and Lepton numbers of the corresponding anti-baryons and anti-leptons (their antiparticles) have a negative sign.

1.1 Neutrino properties

Following the discovery of radioactivity in the late 1800s, there were several studies of α, β and γ-ray emission from radioactive materials. These studies showed that the energies of the α particles were centered around discrete values, and consistent with the quantum mechanical theories developed during the early part of the 20^{th} century. In contrast, a breakthrough experiment by Ellis and Wooster [2] showed that unlike the α particles, β particles have a continuous energy spectrum, as illustrated in Figure 1.1. This discrepancy challenged fundamental conservation laws (such as those of energy, angular momentum, etc.). In 1930, Wolfgang Pauli provided an explanation for the continuous β spectrum by proposing the existence of an undetected particle that was also emitted during β decay. This proposal preserved energy conservation and opened up a captivating new frontier: the world of neutrinos. Pauli's proposition sparked great curiosity regarding the existence of this mysterious particle. The explanation of the simultaneous emission of an electron and this mystery particle was provided by Enrico Fermi [1], who named the particle a neutrino, which means "little neutral one" in Italian. It is now known that there are three modes of β decay [3]:

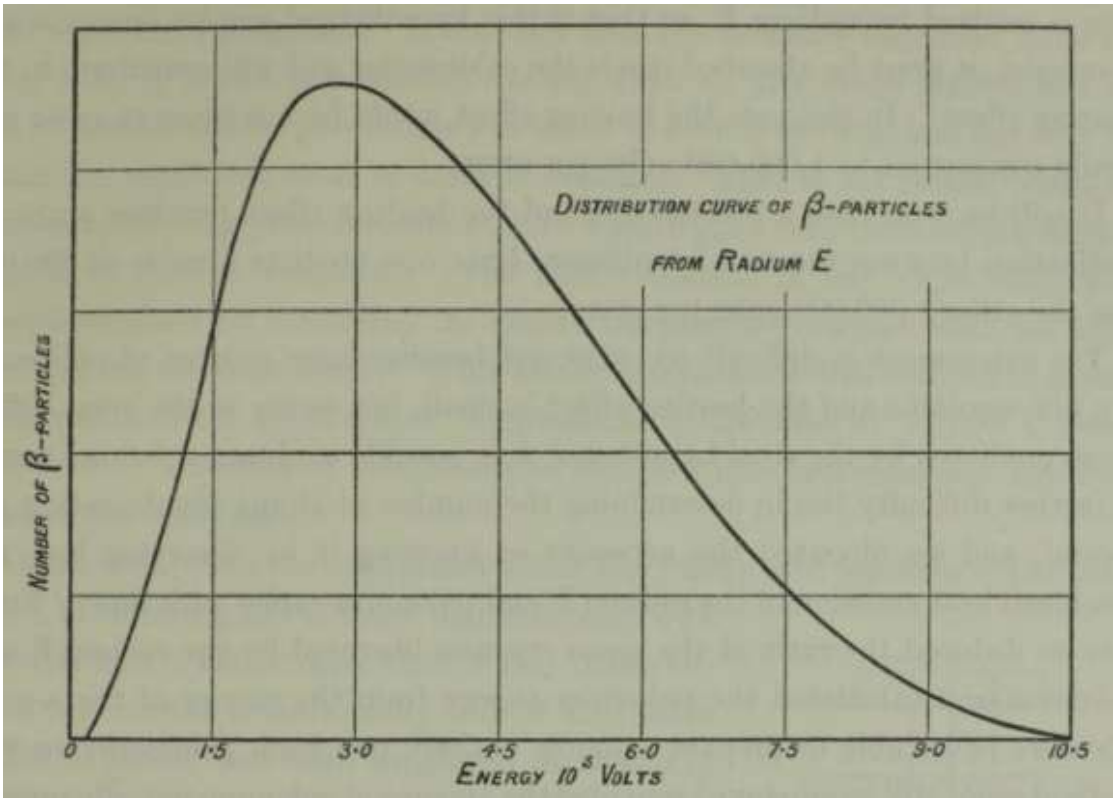

FIGURE 1.1: Energy distribution for β particles emitted from a Radium E source. Figure taken from Ref. [2].

1. β^- decay: ${}^{\mathrm{A}}_{\mathrm{Z}}\mathrm{X}_{\mathrm{N}} \rightarrow {}^{\mathrm{A}}_{\mathrm{Z+1}}\mathrm{X}'_{\mathrm{N-1}} + e^- + \bar{\nu}_e$.
2. β^+ decay: ${}^{\mathrm{A}}_{\mathrm{Z}}\mathrm{X}_{\mathrm{N}} \rightarrow {}^{\mathrm{A}}_{\mathrm{Z-1}}\mathrm{X}'_{\mathrm{N+1}} + e^+ + \nu_e$.
3. Electron capture: ${}^{\mathrm{A}}_{\mathrm{Z}}\mathrm{X}_{\mathrm{N}} + e^- \rightarrow {}^{\mathrm{A}}_{\mathrm{Z-1}}\mathrm{X}'_{\mathrm{N+1}} + \nu_e$.

The original assumption within the Standard Model was that neutrinos are massless spin-1/2 fermions. This requires them to be treated relativistically, which is achieved using the free particle Dirac equation

$$i\frac{\partial\psi}{\partial t} = (\vec{\alpha}\cdot\vec{p} + \beta m)\psi. \tag{1.1}$$

In the above, we set $\hbar = c = 1$ for convenience. The 4×4 $\vec{\alpha}$ and β matrices may be represented in the Weyl representation as,

$$\vec{\alpha} = \begin{pmatrix} -\vec{\sigma} & 0 \\ 0 & \vec{\sigma} \end{pmatrix}; \quad \beta = \begin{pmatrix} 0 & I \\ I & 0 \end{pmatrix}, \tag{1.2}$$

with $\vec{\sigma}$ being the well-known Pauli spin matrices:

$$\sigma_1 = \begin{pmatrix} 0 & 1 \\ 1 & 0 \end{pmatrix}; \quad \sigma_2 = \begin{pmatrix} 0 & -i \\ i & 0 \end{pmatrix}; \quad \sigma_3 = \begin{pmatrix} 1 & 0 \\ 0 & -1 \end{pmatrix}. \tag{1.3}$$

Because of the assumed massless nature of neutrinos, the βm term in the Dirac equation vanishes. Expanding $\vec{p} = -i\vec{\nabla}$, one obtains a system of four decoupled linear equations

$$\frac{\partial\psi}{\partial t} = -(\alpha_1\frac{\partial}{\partial x_1} + \alpha_2\frac{\partial}{\partial x_2} + \alpha_3\frac{\partial}{\partial x_3})\psi, \tag{1.4}$$

whose solutions may be expressed as

$$\psi = U(\vec{p})e^{i(\vec{p}\cdot\vec{x} - Et)}, \tag{1.5}$$

where the $U(\vec{p})$ is a 4-component Dirac spinor,

$$U(\vec{p}) = \begin{pmatrix} U_1 \\ U_2 \\ U_3 \\ U_4 \end{pmatrix}. \tag{1.6}$$

Writing Eqn. (1.4) in matrix form we get,

$$\begin{pmatrix} \frac{\partial U_1}{\partial t} \\ \frac{\partial U_2}{\partial t} \\ \frac{\partial U_3}{\partial t} \\ \frac{\partial U_4}{\partial t} \end{pmatrix} = - \begin{pmatrix} 0 & -1 & 0 & 0 \\ -1 & 0 & 0 & 0 \\ 0 & 0 & 0 & 1 \\ 0 & 0 & 1 & 0 \end{pmatrix} \begin{pmatrix} \frac{\partial U_1}{\partial x_1} \\ \frac{\partial U_2}{\partial x_1} \\ \frac{\partial U_3}{\partial x_1} \\ \frac{\partial U_4}{\partial x_1} \end{pmatrix} - \begin{pmatrix} 0 & i & 0 & 0 \\ -i & 0 & 0 & 0 \\ 0 & 0 & 0 & -i \\ 0 & 0 & i & 0 \end{pmatrix} \begin{pmatrix} \frac{\partial U_1}{\partial x_2} \\ \frac{\partial U_2}{\partial x_2} \\ \frac{\partial U_3}{\partial x_2} \\ \frac{\partial U_4}{\partial x_2} \end{pmatrix} - \begin{pmatrix} -1 & 0 & 0 & 0 \\ 0 & 1 & 0 & 0 \\ 0 & 0 & 1 & 0 \\ 0 & 0 & 0 & -1 \end{pmatrix} \begin{pmatrix} \frac{\partial U_1}{\partial x_3} \\ \frac{\partial U_2}{\partial x_3} \\ \frac{\partial U_3}{\partial x_3} \\ \frac{\partial U_4}{\partial x_3} \end{pmatrix}. \quad (1.7)$$

In terms of two-component spinors, these equations may be re-written as

$$\frac{\partial}{\partial t} \begin{pmatrix} U_1 \\ U_2 \end{pmatrix} = \left(-\vec{\sigma} \cdot \vec{\nabla} \right) \begin{pmatrix} U_1 \\ U_2 \end{pmatrix}, \quad (1.8)$$

and

$$\frac{\partial}{\partial t} \begin{pmatrix} U_3 \\ U_4 \end{pmatrix} = \left(\vec{\sigma} \cdot \vec{\nabla} \right) \begin{pmatrix} U_3 \\ U_4 \end{pmatrix}, \quad (1.9)$$

or as a single eigenvalue matrix equation,

$$E \begin{pmatrix} U_a \\ U_b \end{pmatrix} = \begin{pmatrix} -\vec{\sigma} \cdot \vec{p} & 0 \\ 0 & \vec{\sigma} \cdot \vec{p} \end{pmatrix} \begin{pmatrix} U_a \\ U_b \end{pmatrix}, \quad (1.10)$$

where U_a and U_b are simply

$$U_a = \begin{pmatrix} U_1 \\ U_2 \end{pmatrix}; \quad U_b = \begin{pmatrix} U_3 \\ U_4 \end{pmatrix}. \quad (1.11)$$

Since, $E^2 = p^2$ for massless neutrinos, one obtains a positive energy solution for $E = |\vec{p}|$ and a negative energy solution for $E = -|\vec{p}|$. Substituting $E = |\vec{p}|$ into Eqn. (1.10) yields

$$\frac{\vec{\sigma} \cdot \vec{p}}{|\vec{p}|} U_a = -U_a. \quad (1.12)$$

On the other hand, if we substitute $E = -|\vec{p}|$ in Eqn. (1.10) we get

$$\frac{\vec{\sigma} \cdot \vec{p}}{-|\vec{p}|} U_b = U_b. \quad (1.13)$$

In the Feynman-Stueckelberg approach [3], the negative energy solution represents an antiparticle moving backwards in time, with positive energy $E = |\vec{p}|$. This results in the

eigenvalue equation for the antiparticle

$$\frac{\vec{\sigma}\cdot\vec{p}}{|\vec{p}|}U_b = U_b. \tag{1.14}$$

The above equations allow the definition of an observable called helicity, represented by $\frac{\vec{\sigma}\cdot\vec{p}}{|\vec{p}|}$. It is essentially the projection of a particle's spin along the direction of its linear momentum $\vec{p}$. When the spin is aligned in the opposite direction to the momentum, the equations yield a left-handed particle (a neutrino), with helicity -1. Conversely, a right-handed antiparticle (antineutrino) has helicity $+1$. Similarly, one can obtain helicity solutions for a right-handed neutrino and a left-handed antineutrino. The helicity of a particle is a conserved quantity, as it commutes with the Dirac Hamiltonian in Eqn. (1.1). It allows one to define an operator

$$\hat{H}_e = \frac{1}{2}\left(I \pm \frac{\vec{\sigma}\cdot\vec{p}}{|\vec{p}|}\right), \tag{1.15}$$

which projects out negative or positive helicity states from the general solutions. However the above arguments change if a particle has mass. The mass terms ($m \neq 0$) will appear in the off-diagonal elements of the matrix in Eqn. (1.10). As a result, $\vec{\sigma}\cdot\vec{p}$ will include space-like components, which destroys Lorenz invariance. In such cases, helicity is no longer a good quantum number, which emphasizes the requirement for another observable to describe massive particles along similar lines. In such case one relies on the γ^5 operator, which projects out "chiral" left-handed and right-handed states, with γ^5 defined as

$$\gamma^5 = \begin{pmatrix} -I & 0 \\ 0 & I \end{pmatrix}, \tag{1.16}$$

where I is a 2×2 identity matrix. This chirality operator is Lorentz invariant, making it a suitable candidate for describing massive particles. It is then useful to define the projection operator

$$\hat{P} = \frac{1}{2}\left(I \pm \gamma^5\right), \tag{1.17}$$

which projects out specific chiral eigenstates, with certain handedness. However γ^5 does not commute with the Dirac Hamiltonian, and is consequently not conserved. A famous experiment by Goldhaber, Grodzins and Sunyar [4] showed that neutrinos are left-handed and have negative helicity. Their corresponding antiparticles would have positive helicity on account of the properties of the charge-conjugation operator. In the ultra-relativistic limit where $E \gg m$, the γ^5 operator and the helicity operator both quantify the handedness of particles equally well. Below we first describe one important set of experimental observations which determined that neutrinos have mass. As described further in Section 1.3, this distinction between chirality and helicity is important for massive neutrinos.

1.2 Neutrino Oscillations

A nuclear β decay is essentially the transformation of an up-quark to a down-quark or vice-versa. In the classification shown in Table 1.1, one might expect that the quarks transform within their generations. For example, an up quark can only transform into a down quark, a charm quark into a strange quark, etc. However, decays such as

$$\Sigma^- \rightarrow n + e^- + \bar{\nu}_e, \tag{1.18}$$

and

$$K^- \rightarrow \mu^- + \bar{\nu}_\mu, \tag{1.19}$$

have been experimentally observed, which show that the strange quarks can also decay to up quarks, Therefore, the three generation of quarks are instead listed as

$$\begin{pmatrix} u \\ \mathrm{d}' \end{pmatrix} \begin{pmatrix} c \\ \mathrm{s}' \end{pmatrix} \begin{pmatrix} t \\ \mathrm{b}' \end{pmatrix}, \tag{1.20}$$

where d', s', b' are weak interaction eigenstates, expressed as a linear combination of the mass eigenstates d, s, b

$$\begin{pmatrix} \mathrm{d}' \\ \mathrm{s}' \\ \mathrm{b}' \end{pmatrix} = \begin{pmatrix} U_{ud} & U_{us} & U_{ub} \\ U_{cd} & U_{cs} & U_{cb} \\ U_{tb} & U_{ts} & U_{tb} \end{pmatrix} \begin{pmatrix} d \\ s \\ b \end{pmatrix}. \tag{1.21}$$

The above 3×3 matrix is called the Cabibbo-Kobayashi-Maskawa (CKM) quark-mixing matrix. The observation of quark mixing begs the question if similar flavor mixing is observed in neutrino masses. This question traces its origin to the famous "solar neutrino problem", in which early experiments such as Homestake [3], GALLEX [5] and SAGE [6] observed a deficit of the measured solar ν_e flux compared to expectations from the standard solar model for the sun. As mentioned previously, the SM assumed neutrinos to be massless spin-1/2 fermions. However, if the neutrinos had mass, the neutrino flavor eigenstates can also be expressed as a linear combination of the mass eigenstates

$$\begin{pmatrix} \nu_e \\ \nu_\mu \\ \nu_\tau \end{pmatrix} = \begin{pmatrix} U_{e1} & U_{e2} & U_{e3} \\ U_{\mu 1} & U_{\mu 2} & U_{\mu 3} \\ U_{\tau 1} & U_{\tau 2} & U_{\tau 3} \end{pmatrix} \begin{pmatrix} \nu_1 \\ \nu_2 \\ \nu_3 \end{pmatrix}. \tag{1.22}$$

The unitary 3×3 matrix shown above is known as the Pontecorvo-Maki-Nakagawa-Sakata (PMNS) matrix. This leads to the phenomenon of neutrino oscillations, as described below. For the sake of simplicity, we assume only two flavors mixing, ν_e and

ν_μ. Then the 2×2 unitary mixing matrix can be expressed in terms of a single mixing angle,

$$\begin{pmatrix} \nu_e \\ \nu_\mu \end{pmatrix} = \begin{pmatrix} \cos\theta & \sin\theta \\ -\sin\theta & \cos\theta \end{pmatrix} \begin{pmatrix} \nu_1 \\ \nu_2 \end{pmatrix}. \tag{1.23}$$

Therefore,

$$|\nu_e\rangle = \cos\theta|\nu_1\rangle + \sin\theta|\nu_2\rangle, \tag{1.24}$$

and

$$|\nu_\mu\rangle = -\sin\theta|\nu_1\rangle + \cos\theta|\nu_2\rangle. \tag{1.25}$$

A ν_e emitted at $\vec{x} = 0$, $t = 0$ may be represented using the usual time-evolution prescription as

$$|\nu(\vec{x},t)\rangle = \cos(\theta)e^{-iE_1t}|\nu_1\rangle e^{i\vec{p}_1\cdot\vec{x}} + \sin(\theta)e^{-iE_2t}|\nu_2\rangle e^{i\vec{p}_2\cdot\vec{x}}. \tag{1.26}$$

In the ultra-relativistic approximation, as $E \gg m$, $p_i \approx E_i - \frac{m_i^2}{2E}$ and $x = t$. Therefore Eqn. (1.26) can be rewritten as

$$|\nu(\vec{x},t)\rangle = e^{-\frac{m_1^2 x}{2E}}|\nu_1\rangle\cos(\theta) + e^{-\frac{m_2^2 x}{2E}}|\nu_2\rangle\sin(\theta). \tag{1.27}$$

Then the probability of observing a ν_e after the neutrino traveled a distance x is simply

$$P_{\nu_e\to\nu_e} = |\langle\nu_e|\nu(x,t)\rangle|^2 = 1 - \sin^2(2\theta)\sin^2\left(\frac{\Delta m^2 x}{4E}\right), \tag{1.28}$$

where $\Delta m^2 = (m_2^2 - m_1^2)$. The above shows that the probability of observing a ν_μ instead after propagating a distance x is

$$\begin{aligned} P_{\nu_e\to\nu_\mu} &= 1 - P_{\nu_e\to\nu_e} \\ &= \sin^2(2\theta)\sin^2\left(\frac{\pi x}{L}\right), \end{aligned} \tag{1.29}$$

where L is the oscillation length

$$L = \left(\frac{4\pi E}{\Delta m^2}\right). \tag{1.30}$$

Clearly, as neutrinos traverse through space, they undergo oscillation because of flavor mixing. For three generations, the generic oscillation formula is

$$P(\nu_l \to \nu_{l'}) = \sum_{i=1}^{3} |U_{li}|^2 |U_{l'i}|^2 + \sum_{j\neq i} U_{li}U_{lj}U_{l'i}^*U_{l'j}^* exp\left(\frac{-i(m_i^2 - m_j^2)t}{2E}\right), \tag{1.31}$$

where E denotes the energy of the neutrino ν_l. Here, the m_i are the mass values that define the eigenstates $|\nu_i\rangle$. Indeed this phenomenon explains the observed neutrino deficit

in the earlier experiments [3, 5, 6]. Such oscillations were later verified by the Super-Kamiokande [7], KamLAND [8], SNO [9] and the Daya Bay [10] experiments. The term $\Delta m^2_{ij} = m^2_i - m^2_j$ signifies that at least two neutrinos mass eigenstates have non-zero masses. Experimental observations related to solar neutrino oscillations have confirmed that $m_2 > m_1$, with in $\Delta m^2_{21} = 7.57 \times 10^{-5}$ eV^2 [11]. Furthermore, atmospheric neutrino oscillation experiments suggest that the third mass eigenstate may have either the highest or the lowest mass, with $\left|\Delta m^2_{31}\right| = 2.5 \times 10^{-3}$ eV^2 [12]. As exact values for neutrino masses are unknown, there exist two possible neutrino mass hierarchies [13], as depicted in Fig. 1.2. The normal hierarchy corresponds to a mass ordering of $m_1 < m_2 < m_3$. In

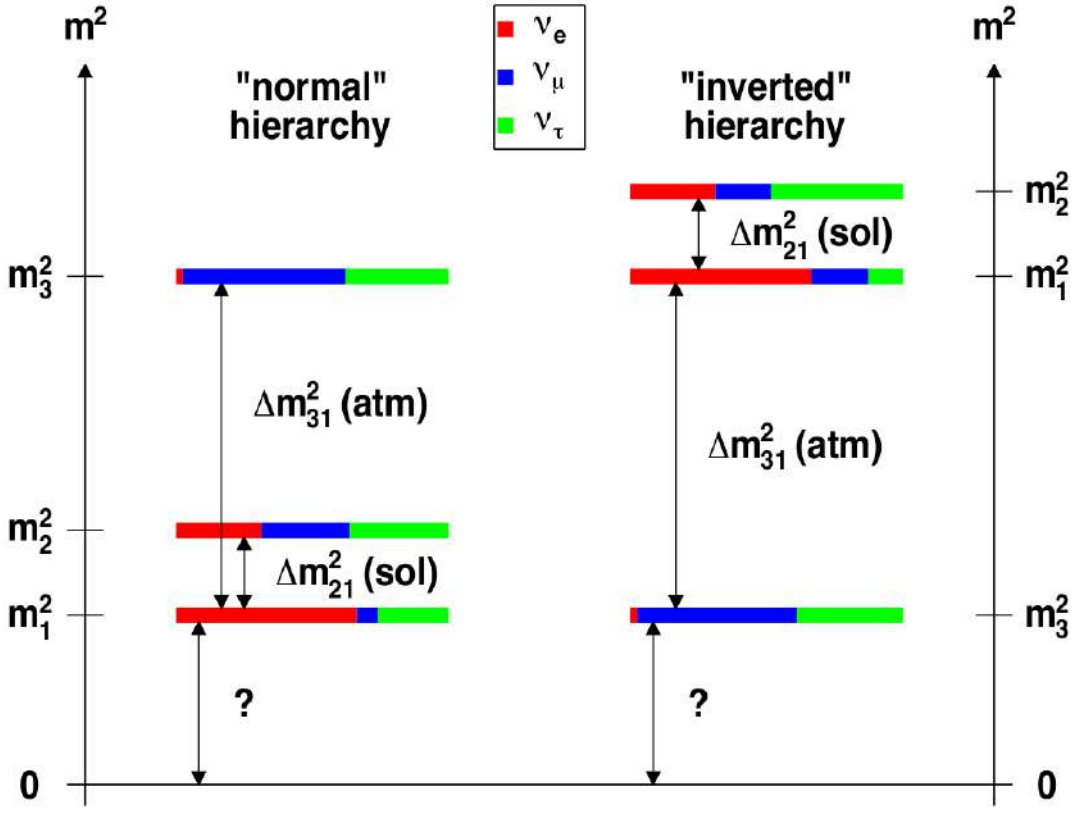

FIGURE 1.2: Two possible arrangements of neutrino masses, the normal and inverted hierarchies. Figure taken from Ref. [14].

contrast, the inverted hierarchy involves a mass ordering where $m_3 < m_1 < m_2$.

1.3 Neutrinoless double β decays

Fig. 1.3 shows the $A = 136$ mass multiplets for atomic nuclei. It is evident from this picture that the mass of ^{136}Xe is smaller than that of ^{136}Cs. This makes the single β decay of $^{136}\text{Xe} \rightarrow {}^{136}\text{Cs}$ energetically forbidden. In such a case one can still observe

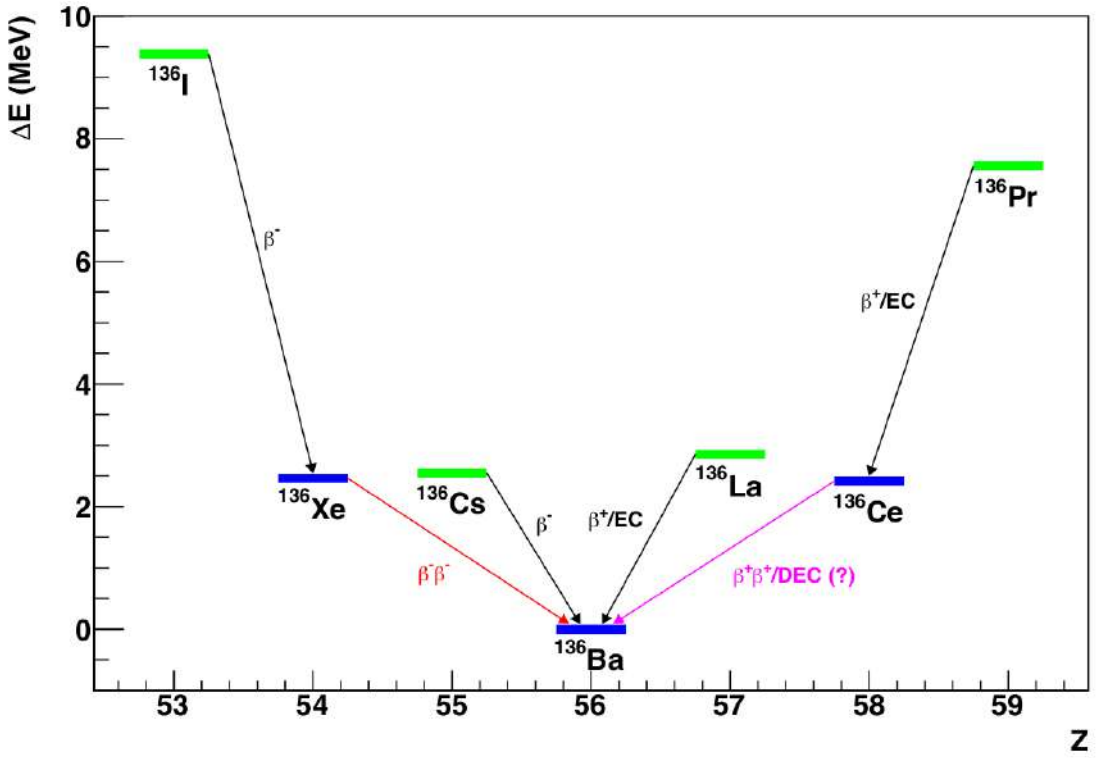

FIGURE 1.3: $A = 136$ mass multiplet. As the level structure shows a single β-decay transition from ^{136}Xe to ^{136}Cs is energetically forbidden. However the second-order $\beta\beta$ decay to ^{136}Ba is still allowed. Figure taken from Ref. [20].

the second-order double β decay to ^{136}Ba,

$$^{136}\text{Xe} \rightarrow {}^{136}\text{Ba} + 2e^- + 2\bar{\nu}_e, \tag{1.32}$$

with the emission of two antineutrinos. Such two-neutrino double β decays ($2\nu\beta\beta$) have been observed in various isotopes [15–18], and typically has half-lives greater than 10^{19} years [19]. Now, let us explore the concept of neutrinoless double beta ($0\nu\beta\beta$) decay. Such a process is described in the right panel of Fig. 1.4, and is possible if neutrinos were massive Majorana fermions. A Majorana particle is indistinguishable from its corresponding antiparticle, which can be represented by the transformation

$$\Psi^c = C\Psi, \tag{1.33}$$

where C is the charge-conjugation operator $C = i\gamma^2\gamma^0$, with γ^μ being the Dirac matrices $\gamma^\mu \equiv (\beta, \beta\vec{\alpha})$. As mentioned in Section 1.1, a special property of this operator is that apart from charge-conjugation, it also flips the handedness (chirality) of the particle. If one assumes that neutrino masses are generated similarly as the quarks and the charged-fermions (i.e via a coupling with the Higgs field), this requires the existence of right-handed neutrinos which have not yet been experimentally observed. Based on the

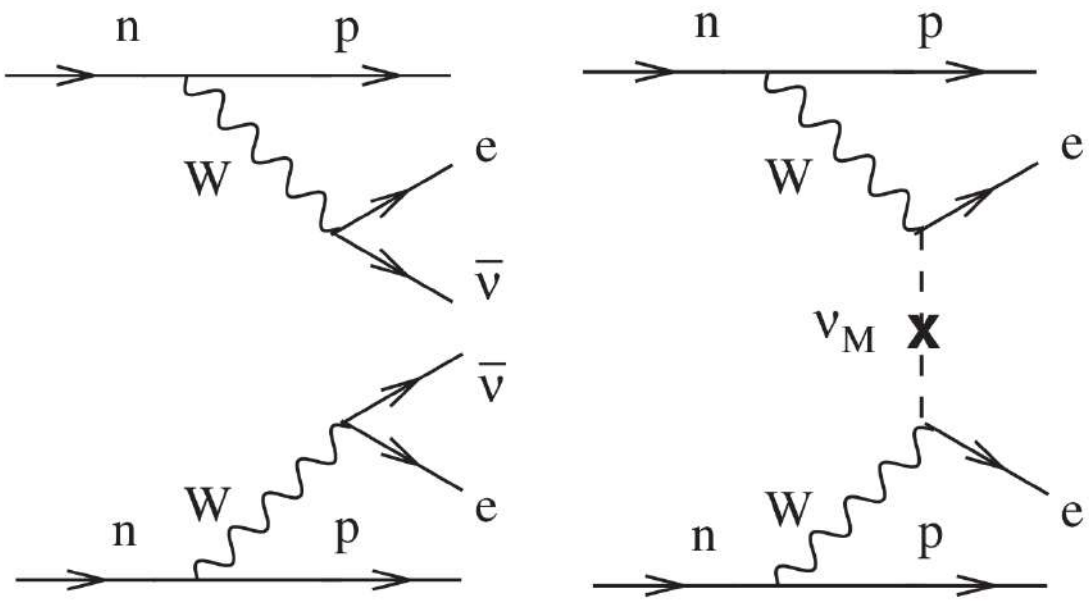

FIGURE 1.4: Feynman diagrams for $2\nu\beta\beta$ decay (left-panel) and $0\nu\beta\beta$ decay (right-panel). Figure taken from Ref. [21].

Dirac equation one can then construct a Lagrangian

$$\mathcal{L}_D = \bar{\nu}(i\gamma^\mu \partial_\mu - m_D)\nu, \tag{1.34}$$

with a Dirac neutrino mass term $\mathcal{L}_{mass} = -m_D\bar{\nu}\nu$, where $\bar{\nu}$ and ν are the neutrino fields with both left-handed and right-handed chiralities. This mass term can be explicitly written as

$$\mathcal{L}_{mass} = -m_D(\bar{\nu}_L\nu_R + \bar{\nu}_R\nu_L). \tag{1.35}$$

However, Dirac neutrinos are deemed unappealing because in addition to right-handed neutrinos, they require unusually small Yukawa couplings to explain the smallness of neutrino masses. A more compelling solution is provided by Majorana neutrinos, which requires only two neutrino fields with the same chirality. This is possible only when neutrinos are their own antiparticles. Under such scenario, if one assumes only left-handed neutrinos, a Majorana mass term is simply

$$\mathcal{L}_M = -\frac{1}{2}m_L(\nu_L^c\nu_L + \nu_L\nu_L^c). \tag{1.36}$$

A similar mass term can also be constructed for the right-handed neutrinos. The above formalism leads to a violation of lepton number by two units.

A very appealing explanation for the smallness of neutrino masses uses both Dirac and Majorana mass terms under special conditions. It is assumed that the Dirac mass m_D is generated by the usual Higgs mechanism and there is no left-handed Majorana term; i.e $m_L = 0$. On the other hand the right-handed Majorana mass term is very large, such

that

$$m_R \gg m_D. \tag{1.37}$$

Consequently, there are two solutions for the masses of Majorana neutrinos given by

$$\begin{aligned} m_1 &\simeq \frac{m_D^2}{m_R} \ll m_D \\ m_2 &\simeq m_R \gg m_D. \end{aligned} \tag{1.38}$$

This explanation, called the see-saw mechanism [21], relates the observed smallness of neutrino masses to a violation of lepton number at an energy scale, determined by $m_R \sim 10^{15}$ GeV.

In summary, if neutrinos were massless, the chiral nature of weak interactions (with purely left-handed neutrinos and right-handed antineutrinos) will not allow such $0\nu\beta\beta$ decay to occur. This is because $\bar{\nu}_e$ and ν_e come with opposite helicities, and helicity is conserved for massless particles. However, for neutrinos with mass one cannot speak of helicity anymore as it violates Lorenz invariance. The correct label to describe massive neutrinos is chirality, which is not a conserved quantity. This allows for new physics mechanisms to make a boost to a reference frame where a right-handed $\bar{\nu}_e$ will be the same as a left-handed ν_e, which leads to an annihilation of the two virtual neutrinos in the $\beta\beta$ decay process, and the two emitted electrons take all the available decay energy as shown in the right panel of Fig. 1.4. Such $0\nu\beta\beta$ decay violates lepton number conservation by two units ($\Delta L = 2$). Therefore, the experimental observation of $0\nu\beta\beta$-decay would not only demonstrate lepton number violation, but also support the idea that neutrinos are Majorana particles.

The effective Majorana mass $\langle m_{\beta\beta} \rangle$ for such a process can be expressed as a superposition of the three neutrino mass eigenstates

$$\langle m_{\beta\beta} \rangle = \left| \sum_i U_{ei}^2 m_i \right|, \tag{1.39}$$

where the U_{ei} are elements of the PMNS matrix in Eqn. (1.22). In such scenario, $\langle m_{\beta\beta} \rangle$ is related to the half-life of the $0\nu\beta\beta$ decay as

$$\frac{1}{T_{1/2}} = \left| \langle m_{\beta\beta} \rangle \right|^2 \left| M^{0\nu} \right|^2 G^{0\nu}(Q, Z), \tag{1.40}$$

where $G^{0\nu}(Q, Z)$ is a phase space factor[1], which depends on the Q-value of the decay and $\left| M^{0\nu} \right|$ is the nuclear matrix element (NME) for the $0\nu\beta\beta$ transition. As the lightest neutrino mass is currently unknown, one can plot possibilities for the neutrino mass

[1] The phase space factor is related to the number of available states per unit energy.

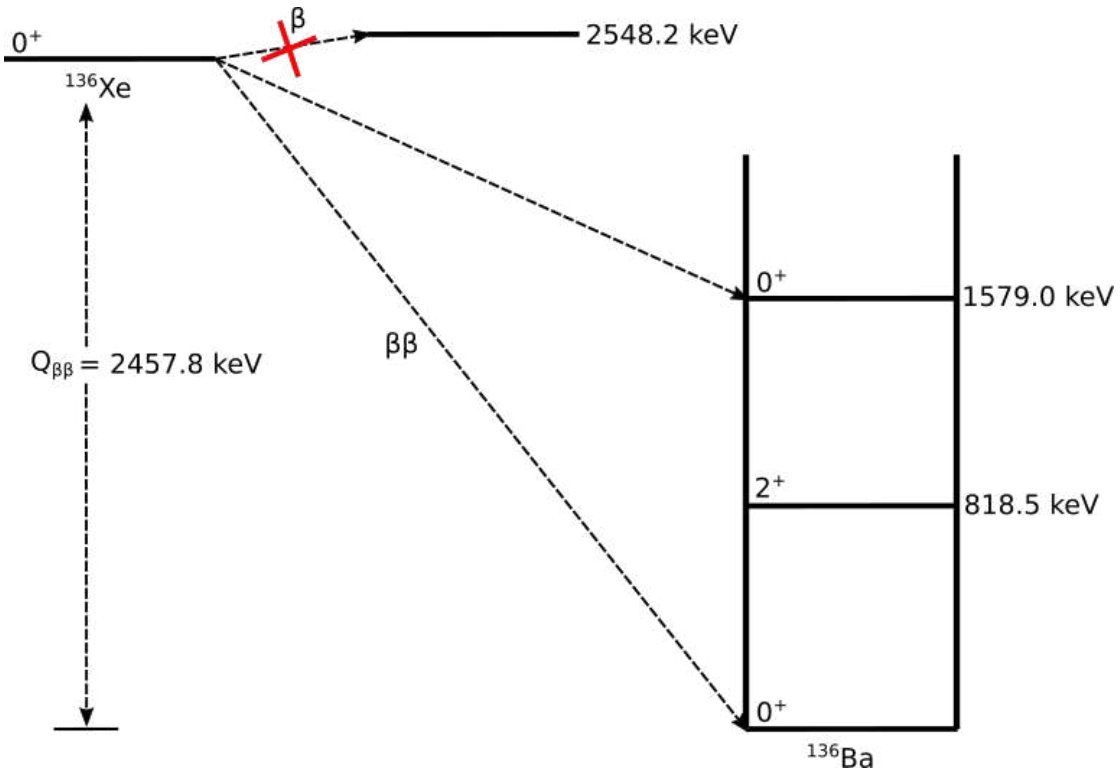

FIGURE 1.5: The $\beta\beta$-decay scheme of ^{136}Xe to ^{136}Ba.

spectrum based on the measured mixing angles from available oscillation data. This is shown in Fig. 1.6, which plots the dependence of $\langle m_{\beta\beta} \rangle$ on m_{lightest}. Future experiments strive to measure $\langle m_{\beta\beta} \rangle$ to better than 10 meV, which is well below the inverted hierarchy scenario. The nEXO experiment [23] aims to observe ^{136}Xe $0\nu\beta\beta$ decay, with a projected half-life sensitivity that is greater than 10^{28} years [24]. The decay scheme of such a process is shown in Fig. 1.5. I briefly describe this experiment in the following chapter.

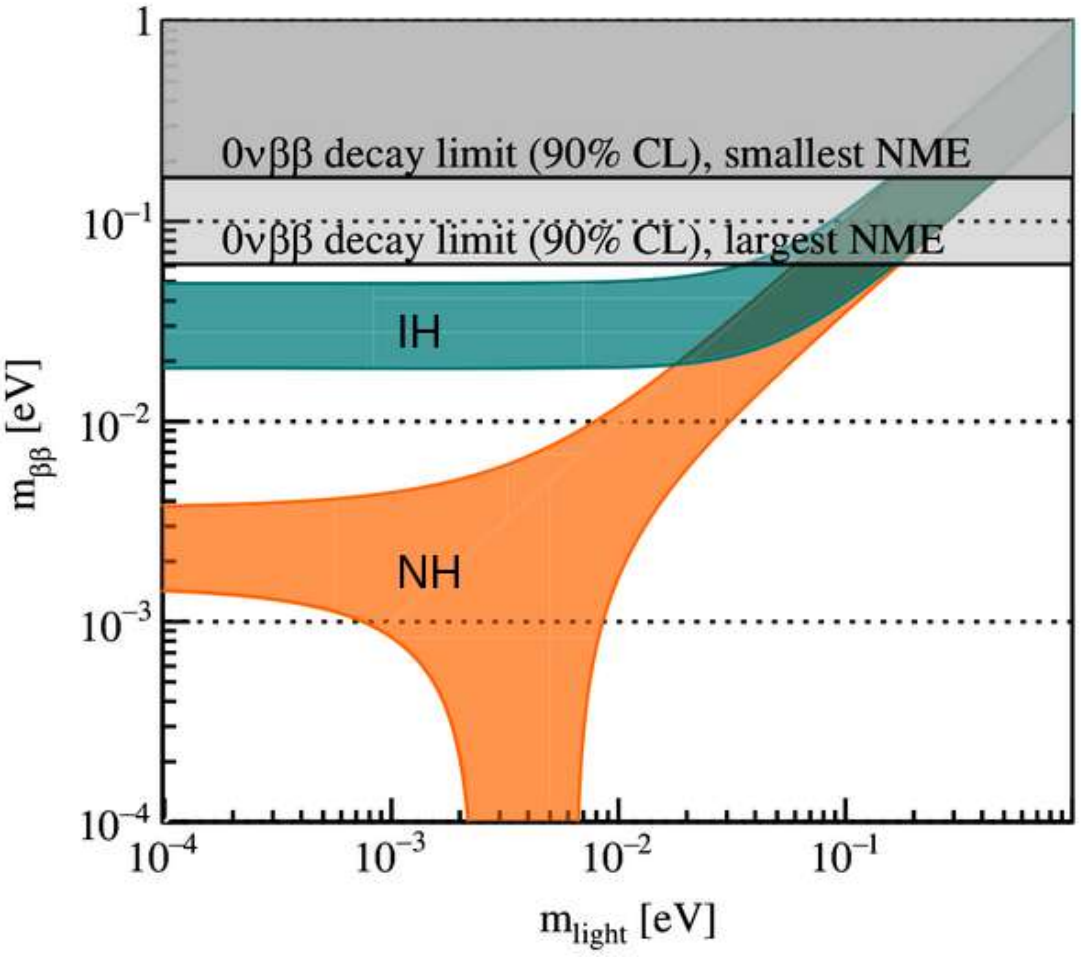

FIGURE 1.6: The effective Majorana neutrino mass $\langle m_{\beta\beta} \rangle$ as a function of the lightest neutrino mass m_{light}, based on available mixing angle data. IH stands for inverted hierarchy, while NH stands for the normal mass hierarchy. Figure taken from Ref. [22].

Chapter 2

The nEXO experiment

2.1 Overview

The next-generation Enriched Xenon Observatory (nEXO) builds on its predecessor, the EXO-200 experiment [25], to search for ^{136}Xe $0\nu\beta\beta$ decay. Fig. 2.1 shows the conceptual design of the experiment, which is planned to be situated at the SNOLAB underground laboratory in Sudbury, Canada. The laboratory is located approximately 2 km below

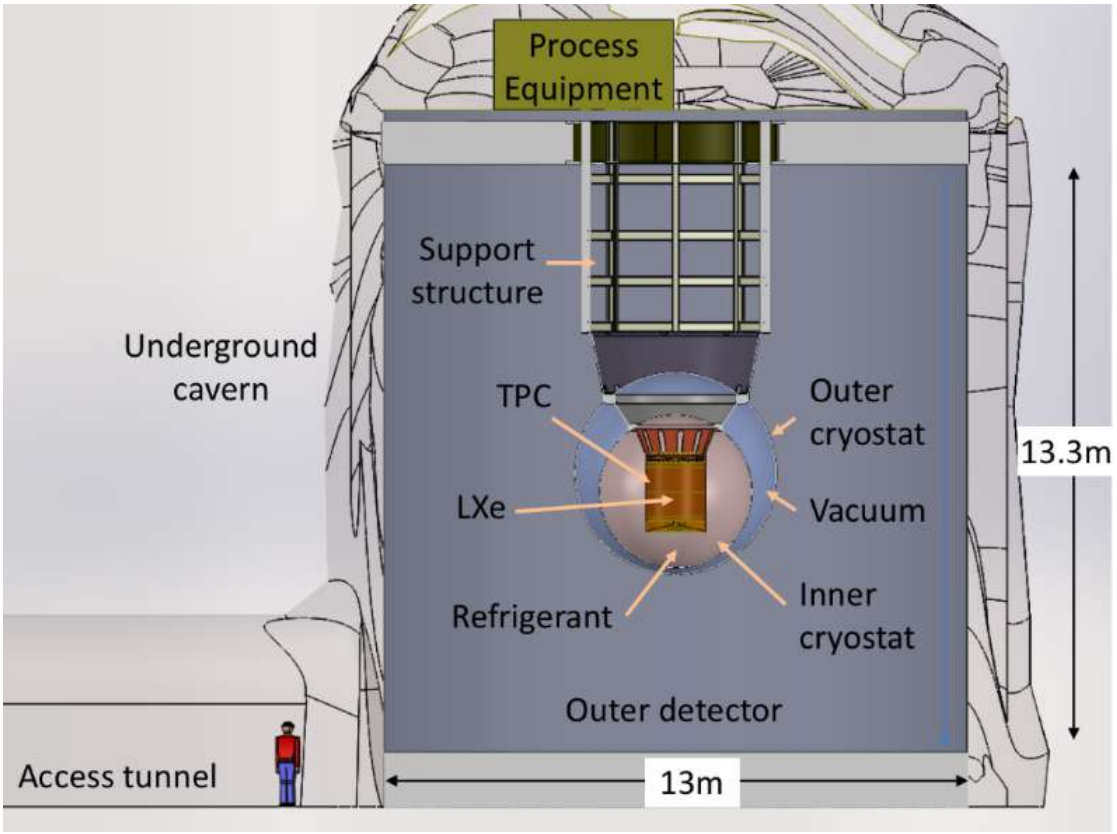

FIGURE 2.1: Conceptual design of the nEXO experiment. Figure taken from Ref. [23].

the earth's surface, in a shaft of the Creighton nickel mine [26]. The ∼2000 m rock overburden on top of the laboratory provides significant shielding from cosmic rays, which is a critical aspect for such rare event searches. The signal for $0\nu\beta\beta$ decay is a monoenergetic peak at the decay Q value, which corresponds to the summed energy of the two electrons from the decay. Fig. 2.2 illustrates such events, in the vicinity of the unavoidable $2\nu\beta\beta$ decay background. In an idealized background-free scenario, the number of observed $0\nu\beta\beta$ decays ($N_{0\nu\beta\beta}$) in the region of interest (ROI) is given by

$$N_{0\nu\beta\beta} = \ln(2) \cdot \frac{a \cdot m}{M} N_A \cdot \epsilon_{det} \cdot \frac{t}{T_{1/2}}, \tag{2.1}$$

where m is the mass of the material used for the $0\nu\beta\beta$ decay search, a is its isotopic enrichment, M is the molar mass of the isotope, N_A is Avogadro's number, ϵ_{det} is the detector efficiency, and t is the observation time. Eqn. (2.1) shows that in the absence of backgrounds, a $0\nu\beta\beta$ detector's sensitivity scales linearly with its size and the measurement time. This sensitivity is affected by background events in the region,

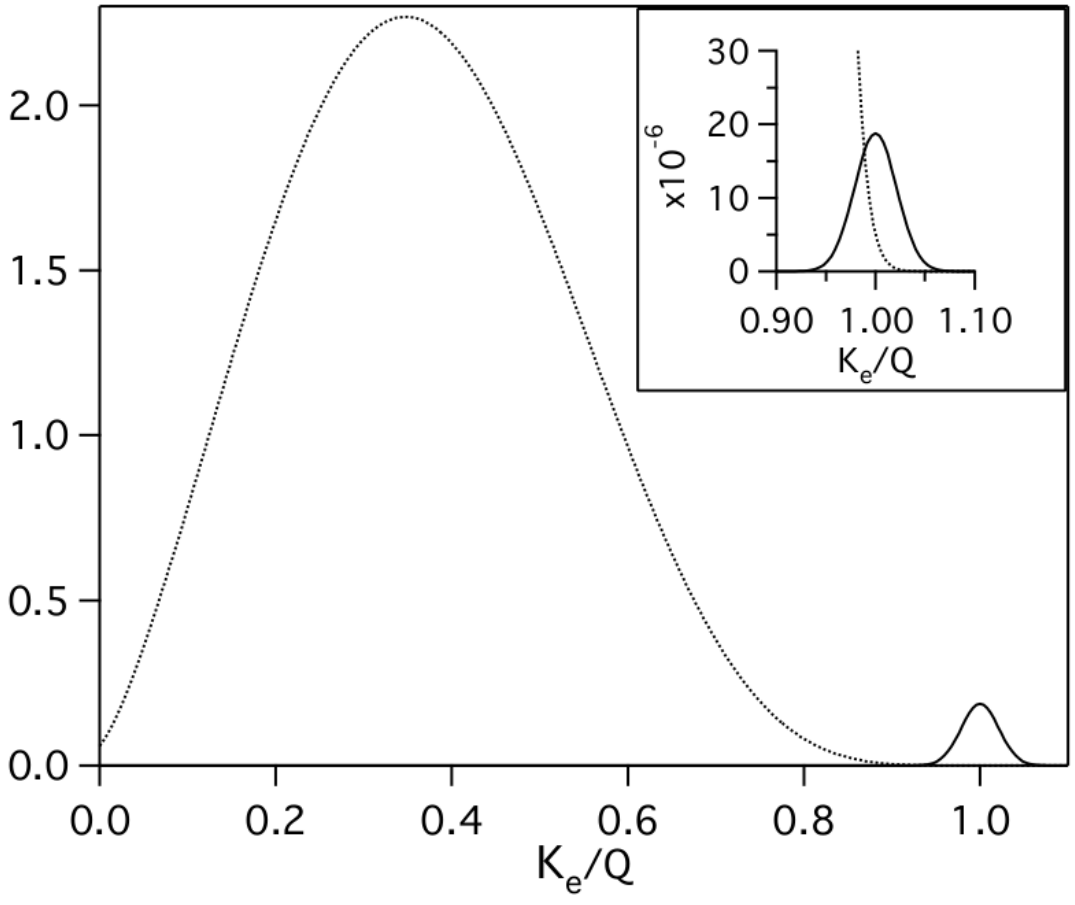

FIGURE 2.2: A $0\nu\beta\beta$ decay peak relative to the continuous $2\nu\beta\beta$ decay spectrum. Figure taken from Ref. [27].

so that [19]

$$T_{1/2}^{0\nu\beta\beta} \propto a \cdot \epsilon_{det} \sqrt{\frac{m \cdot t}{B \cdot \Delta E}}. \tag{2.2}$$

Here B represents the background events in the ROI and ΔE is the energy resolution of the $0\nu\beta\beta$ decay peak. Although achieving a complete background-free scenario is impossible in realistic conditions, the background is one of the several controllable parameters that can be optimized to maximize the sensitivity of a $0\nu\beta\beta$ decay search. The other parameters that are critical for such measurements are a, m, t and ΔE. It is therefore important to have large-scale detectors, with minimal background and maximal energy resolution. The design of the nEXO detector, shown in Fig. 2.1, is based on these considerations. It comprises of a single-phase time projection chamber (TPC), filled with 5 tons of liquid xenon (LXe) that is isotopically enriched to 90% ^{136}Xe. The LXe serves a dual purpose, both as a detection medium as well as the source of the sought-after $0\nu\beta\beta$ decay. These unique features of the nEXO experiment have been derived from the success of EXO-200 as a TPC detector. The general working principle of the TPC is described below.

2.2 TPC working principle

The use of xenon as a detector offers several advantages for rare-event searches [28]. One is its high Z and density ($Z = 54$, $\rho \approx 3\text{g/cm}^2$), which provide considerable self-shielding from γ-ray and neutron-induced environmental backgrounds. Furthermore, enriching xenon is relatively straightforward and the detector is scaleable in size. There are two types of xenon TPCs used in such experiments: the single-phase TPC, which comprises of a volume filled with either xenon in its liquid or gas phase, and the dual-phase TPC, which use xenon in both liquid and gas phases. The primary advantage of a TPC is that it allows a three-dimensional topological reconstruction of the deposited radiation within the TPC volume, through its ionization and scintillation channels. When energy is deposited in the LXe, it produces electron-ion pairs and xenon excitons [28]. An external electric field is applied to collect the electrons at an anode plane, which provides a 2-dimensional (XY coordinate) event reconstruction. When the ionization electrons drift towards the anode, a positive charge is induced on different tile strips in accordance to the Shockley-Ramo theorem [29]. This behaviour is characterized as electronics noise, as the induced charge degrade the reconstruction of the total charge collected at the anode. A fraction of the ionization electrons recombine with xenon ions, generating excited states that later de-excite. This results in the emission of scintillation photons in the vacuum ultra-violet (VUV) region of 175 nm. Since the ionization electrons drift at roughly constant velocity, information along the third dimension (the Z coordinate)

is obtained by measuring the electron drift time (using the relation $v = \frac{z}{t}$). A large homogeneous TPC detector can effectively measure both the desired signal and the background simultaneously. The primary source of backgrounds at the $0\nu\beta\beta$ decay Q value are expected to be from γ-rays that originate from long-lived radionuclides. These γ-rays will deposit energy at multiple locations within the TPC because of their tendency to undergo Compton scattering. Events of this nature are classified as "multi-site" (MS) events. In contrast, a $0\nu\beta\beta$ event would deposit its energy at a single location, making it a "single-site" (SS) event. The identification and separation of MS-events minimizes background contributions, which enhances the sensitivity and accuracy of the detector. In the nEXO design, an outer detector (OD) surrounding the TPC will be filled with water, which shields against room-background and can also be used to veto cosmic-ray induced events. An outer cryostat, kept under a vacuum separates the OD from an inner cryostat that surrounds the TPC volume. Similar to the EXO-200 detector, the inner cryostat will be filled with HFE-7000 fluid[1]. This enhances the shielding of the innermost section from γ-rays and ensures a substantial thermal mass, with minimal temperature gradients across the chamber, which are important for maintaining the xenon in its liquid phase.

2.3 Detector design

The readout systems for light and charge in the nEXO TPC are designed to achieve an energy resolution which is $\leq$1% at the $0\nu\beta\beta$ decay Q value [23, 30], while also ensuring low-background contributions from all possible sources and a homogeneous volume to maximize self-shielding. To meet this requirement, the nEXO TPC ought to maintain an electron lifetime (τ_e, defined as the drift time after which the number of initial ionization electrons reduce by a factor s^{-1}) that is greater than 10 ms, to ensure sufficient charge collection at the anode. This task is accomplished by continuously purifying the xenon of electronegative contaminants with highly efficient getters. Fig. 2.3 illustrates a cross-section view of the nEXO TPC. The TPC will be constructed with low-background copper [31], measuring to around 1.3 m in both height and diameter. These dimensions are critical for minimizing backgrounds arising from radioactive contamination on the vessel walls and inner surfaces, by optimizing the surface-to-volume ratio of the TPC. As illustrated in Fig. 2.3, silicon photomultipliers (SiPMs) situated at the TPC's barrel, behind the field shaping rings (FSR)[2], will be used to detect the VUV scintillation light.

[1] The 3 M^{TM} Novec^{TM} 7000 Engineered Fluid represents a thermally stable dielectric fluid that maintains a liquid state even in extremely low temperatures. For more information, refer to https://multimedia.3m.com/mws/media/1213720/3m-novec-7000-engineered-fluid-tds.pdf.

[2] The field shaping rings are evenly spaced and securely connected to both the cathode and the anode via a chain of resistors, enabling a uniform electric field inside the TPC.

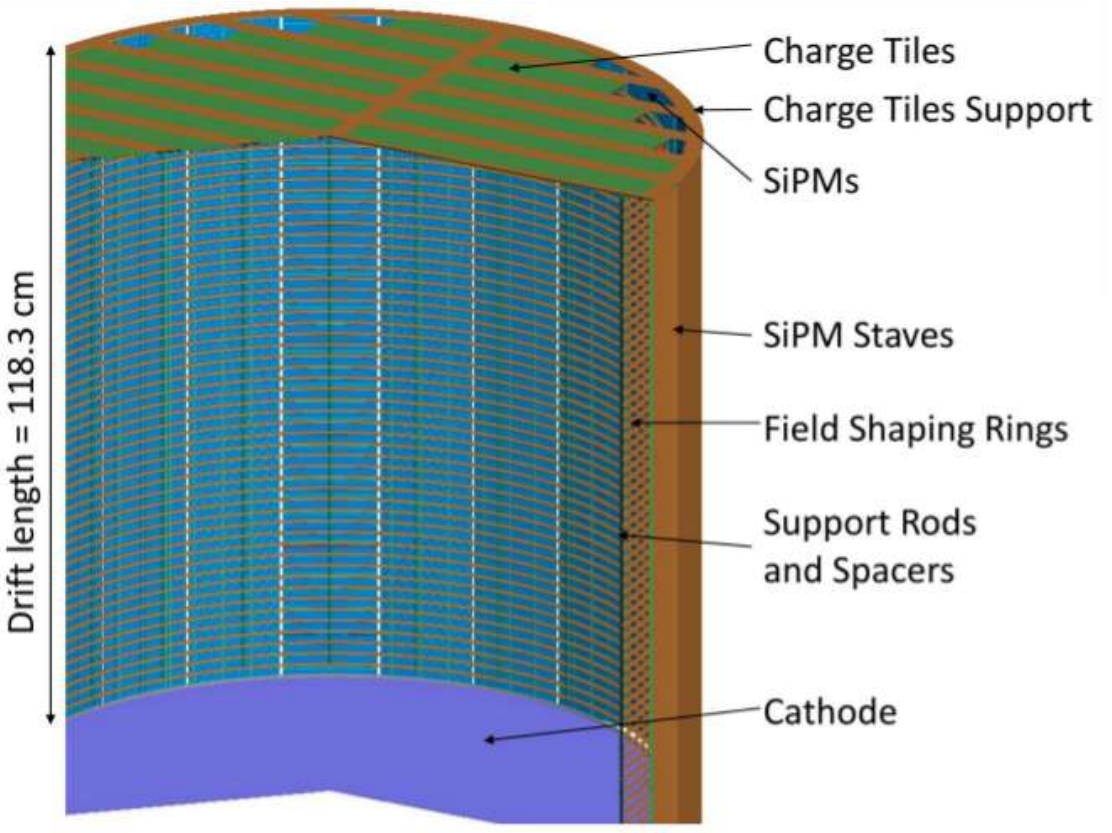

FIGURE 2.3: A schematic representation of the nEXO TPC, illustrating the photon and charge collection system. The charge collecting tiles gather the ionization electrons at the anode, while the photons are detected by SiPMs positioned at the detector barrel behind the high voltage field rings. Figure taken from Ref [24].

The ionization electrons will be detected by a charge collecting plane located at the top of the TPC. The scintillation and ionization signals are strongly anti-correlated because of fluctuations in the recombination of electrons and xenon ions [32, 33]. Consequently, the deposited energy can be determined by a linear combination of these two signals, expressed as

$$E = W \cdot (S_0 + Q_0), \tag{2.3}$$

where S_0 represents the number of scintillation photons, Q_0 the number of ionization electrons, and W the average energy required to generate an electron-ion pair. To observe $0\nu\beta\beta$ decay, the energy E must equal the monoenergetic peak at the Q value, corresponding to the decay. Extensive simulations have shown that the use of this linear combination (of scintillation light and charge signals) yields an energy resolution of $\sigma_E/E \leq 1\%$ for the nEXO TPC. This is shown in Fig. 2.4. This method was experimentally verified by the XENON collaboration [34], who achieved a resolution of $(0.80 \pm 0.02)\%$.

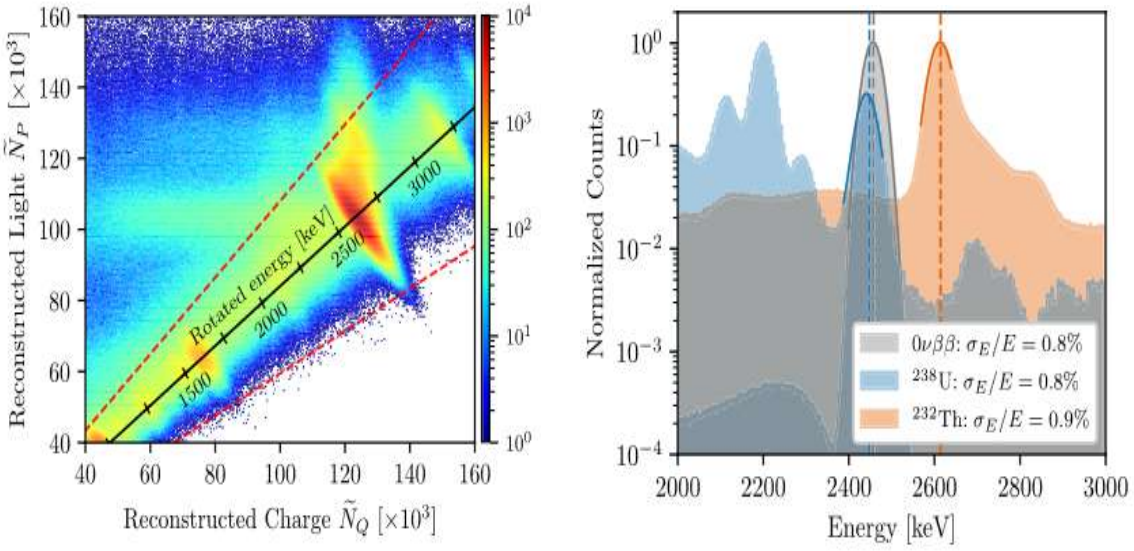

FIGURE 2.4: Left-panel: The relationship between reconstructed charge and light. Events with a high light-to-charge ratio are events that are between the FSR and the TPC vessel, where only scintillation light is detected. These events are removed by the diagonal cut highlighted by the dashed lines. The clear anti-correlation between reconstructed light and charge is evident. Right-panel: The rotated energy, obtained as a linear combination of the charge and light signals, yields an energy resolution $\sigma_E/E \approx 0.8\%$. Figures taken from Ref. [24]

2.4 nEXO sensitivity

The EXO-200 experiment placed a lower bound on the ^{136}Xe $0\nu\beta\beta$ decay half-life to be 3.5×10^{25} yr at the 90% confidence level (CL) [25]. However, the current best limit is 2.3×10^{26} yr from KamLAND-Zen [35]. In comparison, the projected sensitivity of the nEXO experiment is 1.38×10^{28} yr at the 90% CL [24]. This sensitivity is evaluated using a frequentist approach, by employing a profile likelihood test. Toy Monte Carlo simulations were generated to determine the median upper limit for the $0\nu\beta\beta$ decay half-life, at the 90% CL. The increase in the sensitivity compared to EXO-200 (shown in Fig. 2.5) is because of significant research efforts made to improve the light and charge collection efficiencies and extensive radio assay measurements performed to better characterize and minimize backgrounds. Based on its current sensitivity projection, nEXO will be able to probe beyond the inverted neutrino mass hierarchy region of Fig. 2.6, after 10 years of data acquisition.

Two possible outcomes emerge from the nEXO experiment. In the more optimistic scenario nEXO may achieve a direct observation of $0\nu\beta\beta$ decay. Alternatively, the course of action would be to set an improved limit on the half-life of $0\nu\beta\beta$ decay. If this were the case, a future kilo-tonne scale detector [36] may be designed to further enhance the sensitivity and the discovery potential for observing the decay.

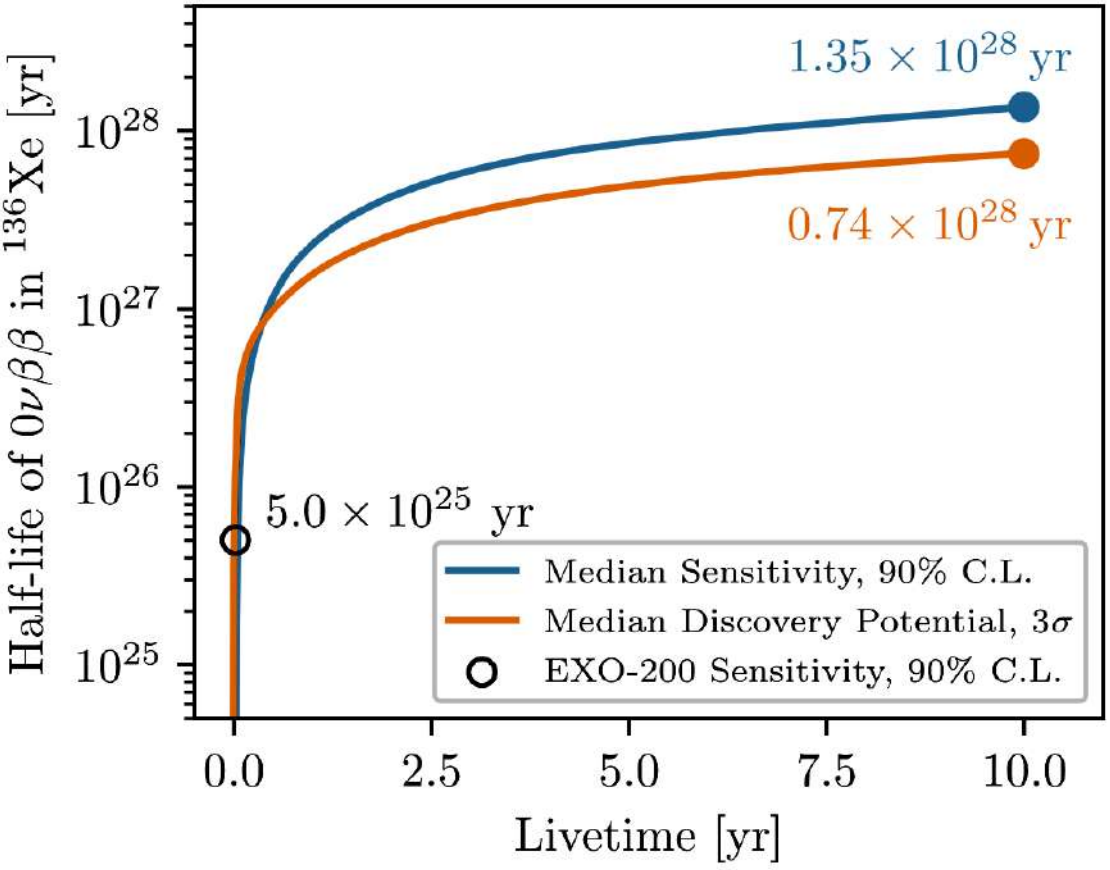

FIGURE 2.5: nEXO's projected sensitivity and discovery potential after 10 years of data collection. Figure taken in Ref. [24].

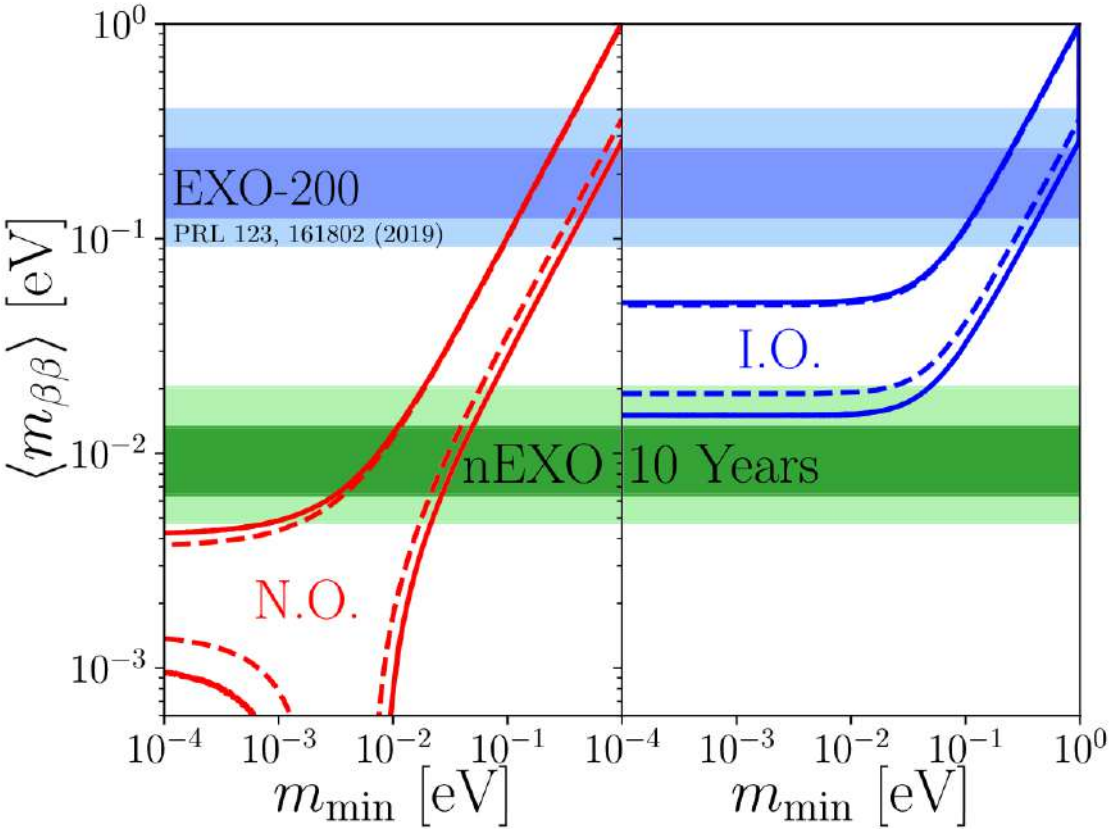

FIGURE 2.6: The sensitivity reach of the nEXO experiment. The horizontal band in the lower-limit arises from a spread in calculated values of the nuclear matrix element (NME) for ^{136}Xe $0\nu\beta\beta$ decay. Figure taken from Ref. [24].

Chapter 3

Experimental details

As mentioned in Chapter 2, nEXO is designed to be constructed with low-background components. While such α-particles may be efficiently rejected through a charge/light ration analysis [23], a precise understanding of the α ionization response in LXe remains crucial. This knowledge is important to accurately model such interactions within the TPC, and refine background rejection techniques to improve the overall signal to noise ration for the experiment. In order to obtain useful information in this regard, this work investigates the charge energy resolution of α-induced energy depositions at 400 V/cm, with a single-phase prototype LXe TPC, located at Stanford University. To achieve this goal, we used 6 MeV α-particles from a ^{228}Th source to generate uniformly distributed events inside the TPC. The charge collecting plane at the anode collects the charge from the α interactions within the LXe as SS events, similar to $0\nu\beta\beta$ decay. Through a detailed and precise analysis presented in Chapter 4, this study seeks to improve our understanding of α ionization in LXe. This chapter provides an overview of the Stanford prototype TPC and its components, followed by a discussion on the experimental data acquisition.

3.1 The Stanford prototype TPC

The Stanford TPC is a single-phase LXe prototype TPC, developed at Stanford University for testing the instrumentation relevant for the yet-to-be built nEXO detector. It is housed in a cylindrical stainless steel chamber, measuring around 20 cm in length and 25 cm in width, with a total LXe mass of about 27 kg (Figs. 3.1 and 3.2), which is enough to fully submerge the anode charge tile and achieve a drift distance of $\sim$14 cm. The chamber is placed in a dewar filled with HFE-7000 fluid to maintain temperature uniformity inside the TPC. As mentioned previously, the HFE-7000 helps maintain the

FIGURE 3.1: The cylindrical stainless steel chamber that contains the TPC and the semi-cylindrical copper plate that surrounds the TPC.

xenon in its liquid state. This is achieved by making use of a copper plate[1] which is connected to a cryogenic system maintained at 165 K, while the pressure is kept at ∼120 kPa. The temperature of the HFE-7000 fluid is measured using three thermocouples connected to the body of the copper plate. One of these also manages the flow of hydrofluorocarbon (HFC) via a LabVIEW application[2]. Additionally, to measure the temperature inside the TPC, three other thermocouples are used at different locations

[1]The copper plate, connected to a Telemark TVP2000 cryogenic system with approximately 1 kW power at 165 K, is actively cooled by the re-circulation of HFC along with an inert gas through its cubing. These gases operate in a closed-cycle refrigeration system and are crucial for achieving the cryogenic temperatures required in this TPC. For further details on the cryogenic system, refer to https://archive.org/details/manualzilla-id-6019686/mode/1up.

[2]National Instrumentation LabVIEW is a graphical programming environment used for monitoring and controlling the temperature of the TPC and the copper plate, refer to http://www.ni.com/en-us/shop/labview.html.

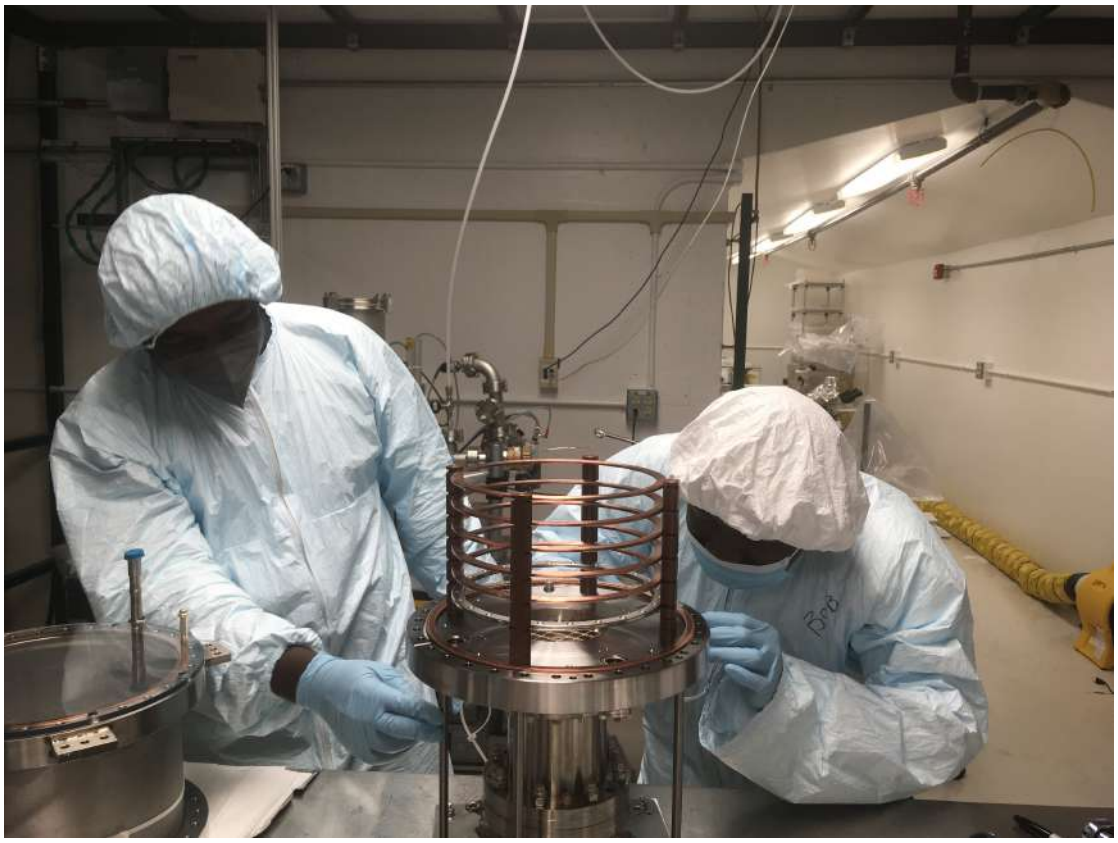

FIGURE 3.2: The Stanford TPC inside its cylindrical chamber.

outside the TPC vessel. The pressure inside the TPC is measured using two Model 121A MKS Baratrons[3] at two different locations. A picture of the dewar is shown in Fig. 3.3. As Fig. 3.4 shows, the active detector volume (which measures 13.5 cm), is defined by the anode charge-collecting plane at the top and a stainless steel cathode grid at the bottom. A negative high voltage of about 6 kV is supplied to the cathode grid, which provides a nominal ∼400 V/cm electric field that is kept uniform with five FSRs shown in Fig. 3.2. The FSRs are held by four low-outgassing polyimid-based plastic Vespel^{TM} spacers, attached at the bottom of the TPC vessel, shown in Fig. 3.2. The Vespel^{TM} spacers also allow the FSRs to be equally spaced with respect to each other. The energy deposited by incoming radiation leads to the generation of both ionization and scintillation signals, as described in Chapter 2. Unlike the nEXO design, here scintillation photons are detected with SiPMs that are positioned approximately 4 cm below the cathode (see Fig. 3.4). As a result, the light efficiency for this particular case is not optimized for a combined improved energy resolution. Ionization electrons are drifted towards the charge sensitive anode plane at the top of the detector because of the uniform electric field.

[3]MKS121A Baratron, refer to https://www.mksinst.com/product/product.aspx?ProductID=1191.

FIGURE 3.3: The TPC dewar filled with HFE-7000.

3.1.1 Scintillation channel

The photon readout of the Stanford TPC is an array of 24 1×1 cm^2 SiPMs, which are primarily used to provide a trigger signal to tag specific interactions. The SiPMs are organized into 12 parallel readout channels and are positioned 4 cm below the cathode grid, as illustrated in Fig. 3.5, with their preamplifiers located outside the cryostat. These detectors have high gain, of the order 10^6 [23], which is obtainable at a relatively low bias when compared with vacuum photo-multiplier tubes [38]. They also have high radiopurity, thermal stability and a low outgassing rate. A visual representation is shown in Fig. 3.5, which describes the placement of the SiPM array. Since, as mentioned previously, in this work we focus on studies of the charge energy resolution at the anode, we omit an in-depth discussion regarding the SiPMs for the Stanford TPC.

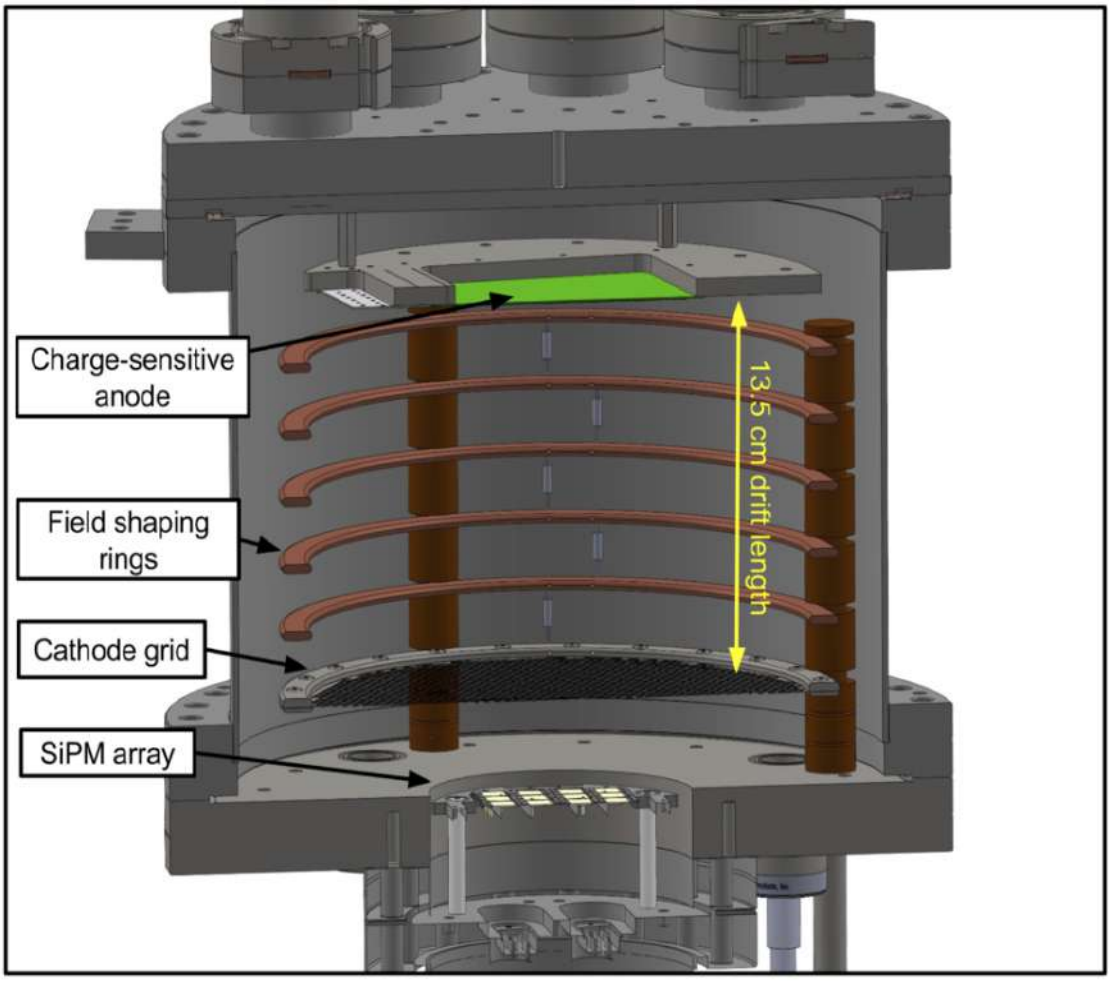

FIGURE 3.4: Schematic representation of The LXe. Figure taken from Ref. [37].

3.1.2 Ionization channel

The ionization channel consists of a 10×10 cm^2 prototype charge-sensitive tile, mounted at the center of a metallic plate holder, as shown in Fig. 3.6. The charge tile, whose substrate is a silica wafer, is described in detail in Ref. [39]. It is made of 60 strips, which are arranged orthogonally (30 in the X direction and 30 in the Y direction), to provide information in the X and Y coordinates. This arrangement of the strips reduces the capacitance between them. The total resistance of each strip is about 5 Ω at 165 K. The strips have layers of Au and Ti on top of the substrate. Layers of 1.5 μm thick SiO_2 are used at the overlap of the X and Y strips to make the strips electrically isolated, with a capacitance of 80 fF at each overlap. This results in a capacitance of 0.9 pF between the strips in parallel and 0.6 pF between pairs of the strips at the overlap [40]. The left picture in Fig. 3.7 shows the charge-sensitive tile mounted on a metallic holder, with the readout electronics connected at the end of each tile strip. In the same figure, the picture on the right shows the X and Y strips, with their specifications. The strips are

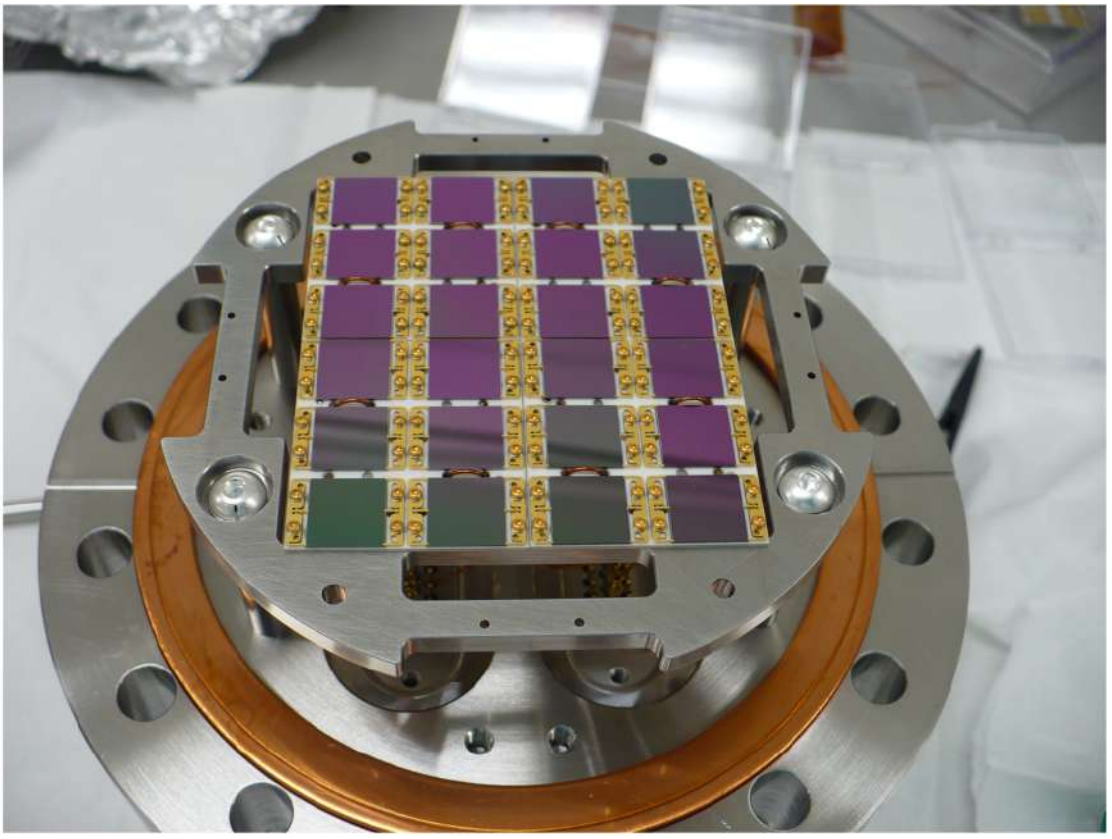

FIGURE 3.5: SiPMs on the Stanford prototype TPC.

connected to preampifiers that are based on the design described in Ref. [41]. Because of limitations in the number of feedthroughs that can connect to the preamplifiers, some channels are ganged together, as shown in the Fig. 3.8. This results in a total of 31 charge-collection channels.

3.2 Radioactive source injection

A recirculation loop, shown in Fig. 3.9, was used to introduce radon from an electroplated ^{228}Th source (with an activity of ∼1400 Bq) into the TPC, which is described in detail in Ref. [42]. The procedure for introducing radon into the TPC is described below.

Before filling the TPC with xenon, a pump-down process was initiated for both the TPC vessel and the recirculation loop, which reduces the pressure of the system to $\sim 10^{-7}$ kPa. This is done by sequentially opening valves $V_{20} - V_{16}$, $V_{13} - V_{10}$, and valves V_8, V_6, V_5, V_3, and V_2, while the other valves remain closed (see Fig. 3.9). These valves also define the path of xenon flow, shown by the arrows in Fig. 3.9. The turbo pump was then used to create a vacuum inside the TPC vessel and the recirculation loop, where the source is installed. This minimizes electronegative impurities (such as O_2) inside the system.

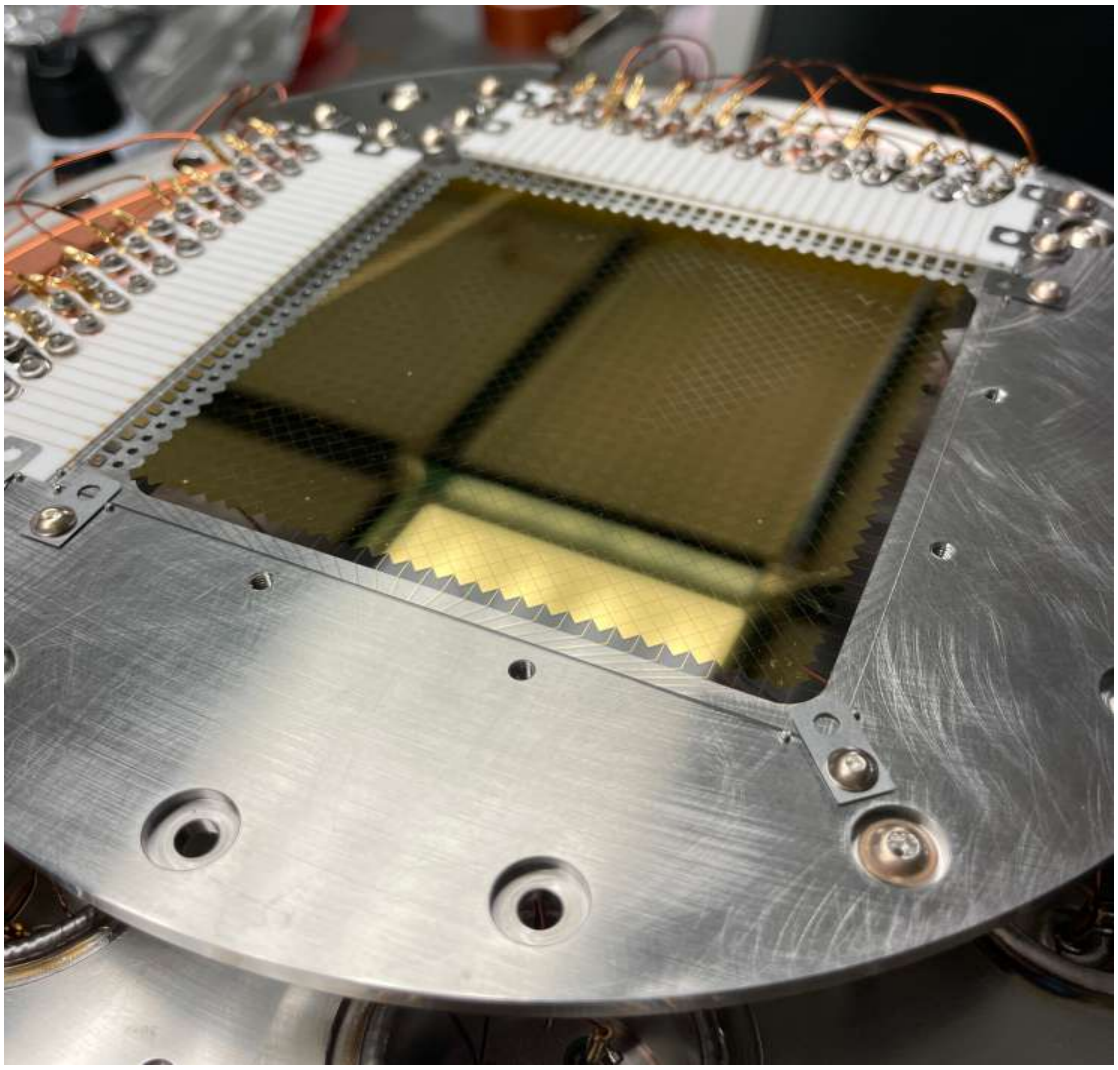

FIGURE 3.6: Charge tile section of the Stanford TPC.

The impurities inside the system were monitored using a residual gas analyser (RGA). When the desired pressure was achieved in the system, all the valves were closed and the system was leak-checked using helium gas. To prepare for the filling of the TPC vessel with xenon, the empty TPC vessel was maintained at 165 K by cooling the HFE-7000 fluid. The xenon is introduced to the TPC through valve V_1. Before opening V_2, the pressure at the xenon bottle is about 5500 kPa. This high pressure region (before valve V_6) is labeled by a red arrow shown in Fig. 3.9. The xenon gas flows through V_3 and V_5 to the regulator at V_6, which regulates the pressure of the gas (to a maximum of 180 kPa) into the low pressure region marked with yellow arrows in Fig. 3.9. At this stage the xenon is in the low pressure region of the recirculation loop. It flows through a magnetically driven xenon pump, through the ^{228}Th source, upon opening valves V_8, V_{10}, V_{11} and V_{13}. Fig. 3.10 shows the decay chain of ^{228}Th. Here, the only gaseous nucleus is ^{220}Rn. The ^{220}Rn mixes with the gaseous xenon, following which the mixture

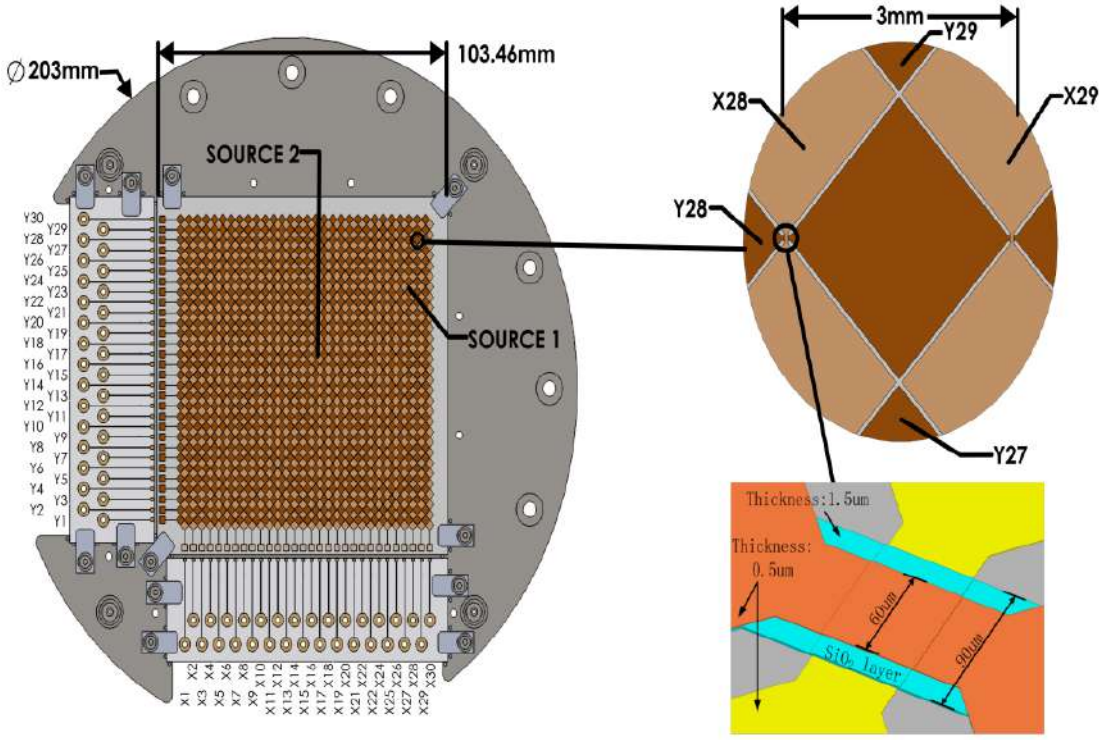

FIGURE 3.7: Schematic of a prototype charge tile. Figure taken from Ref. [39]

of ^{220}Rn and xenon flow through a hot SAES MonoTorr PF3C3R1 getter[4]. Since ^{220}Rn is a noble gas, it cannot be removed by the SAES getter. It passes through the getter and into the cold TPC vessel, where it condenses along with the xenon, when V_{18} is opened. Valve V_6 is then closed with the xenon and ^{220}Rn mixture inside the TPC. ^{220}Rn α decays to ^{212}Pb via the intermediate nucleus ^{216}Po. The ^{212}Pb is uniformly distributed throughout the TPC. Valve V_{21} is then opened to allow the xenon to recirculate for about ten hours. ^{212}Pb β decays to ^{212}Bi which in turn decays via two alternative branches to form stable ^{208}Pb:

1. Around 36% of ^{212}Bi α decays to the ground state in ^{208}Tl, emitting α's at 6 MeV. The ^{208}Tl β decays to stable ^{208}Pb. We call this the alpha branch.

2. The remaining $\sim$ 64% of ^{212}Bi β decay to ^{212}Po. ^{212}Po then α decays to stable ^{208}Pb. This branch is known as the BiPo branch (see Fig. 3.10).

Because of the $\sim$ 300 ns half-life of ^{212}Po, the charge energy resulting from the interaction of the 9 MeV BiPo α's with LXe have continuous energies rather than discrete. Essentially, distinguishing charge energy resulting from interactions of 9 MeV α's and β's with LXe, from the BiPo branch is not possible. Instead, the charge energy from the interactions of α's with LXe causes a shift in the charge energy distribution of the

[4]The getter is used to remove electronegative impurities. Refer to http://www.saespuregas.com/.

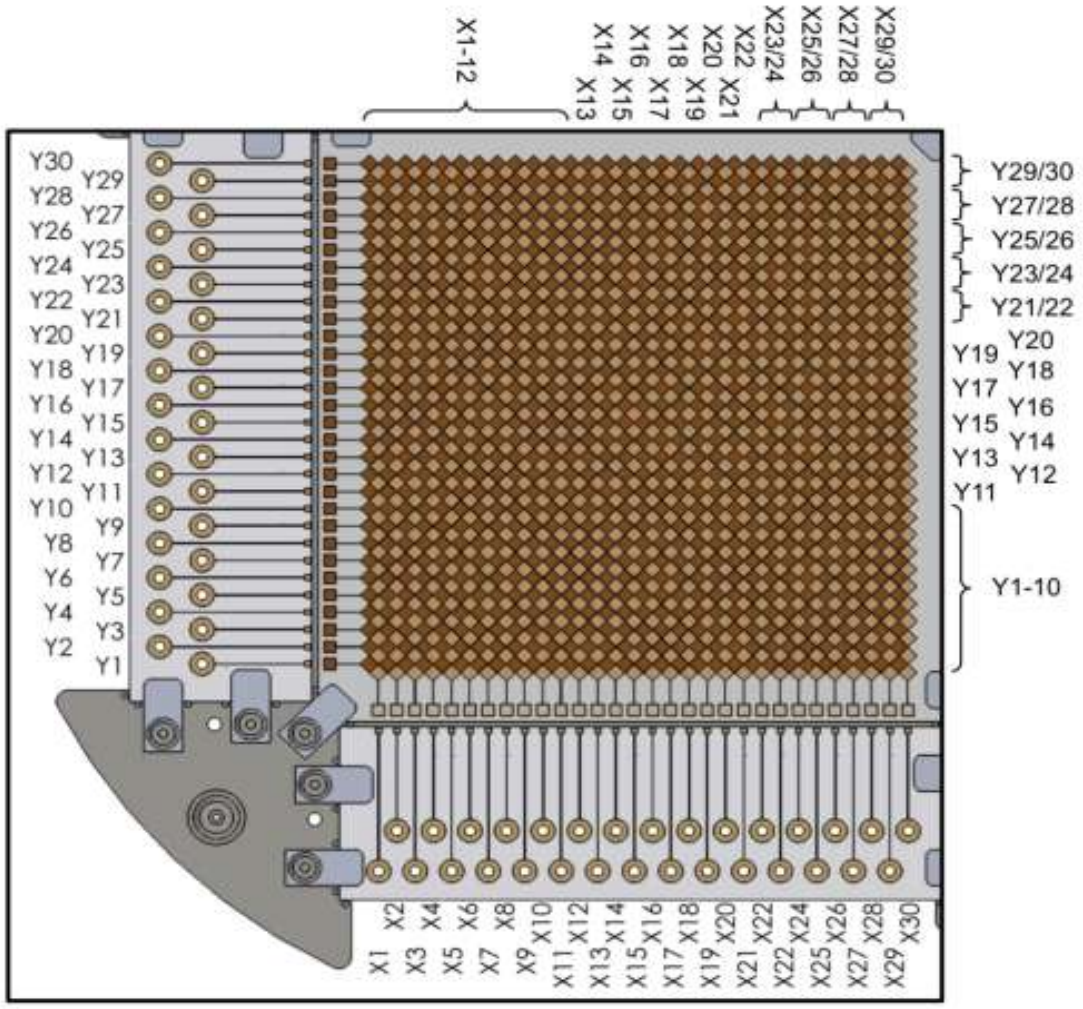

FIGURE 3.8: Schematic representation of the charge tile, showing how the strips are grouped together.

β's by the energy of the α's. In the alpha branch, the 3 minute half-life of ^{208}Tl results in uncorrelated β events with respect to the α events, from the decay of ^{212}Bi to ^{208}Tl[5]. The data for this experiment were collected after $\sim$ 10 hours, to allow the ^{212}Po to decay to ^{212}Bi within the TPC.

This work primarily focuses on the charge energy resolution from the 6 MeV α particles in the alpha branch.

3.2.1 Data collection

Signals from the SiPMs trigger data acquisition, initiating the collection of charge signals. The charge sensitive tile at the anode detects drifted charges within the TPC and

[5]This will be explicitly shown in following chapter.

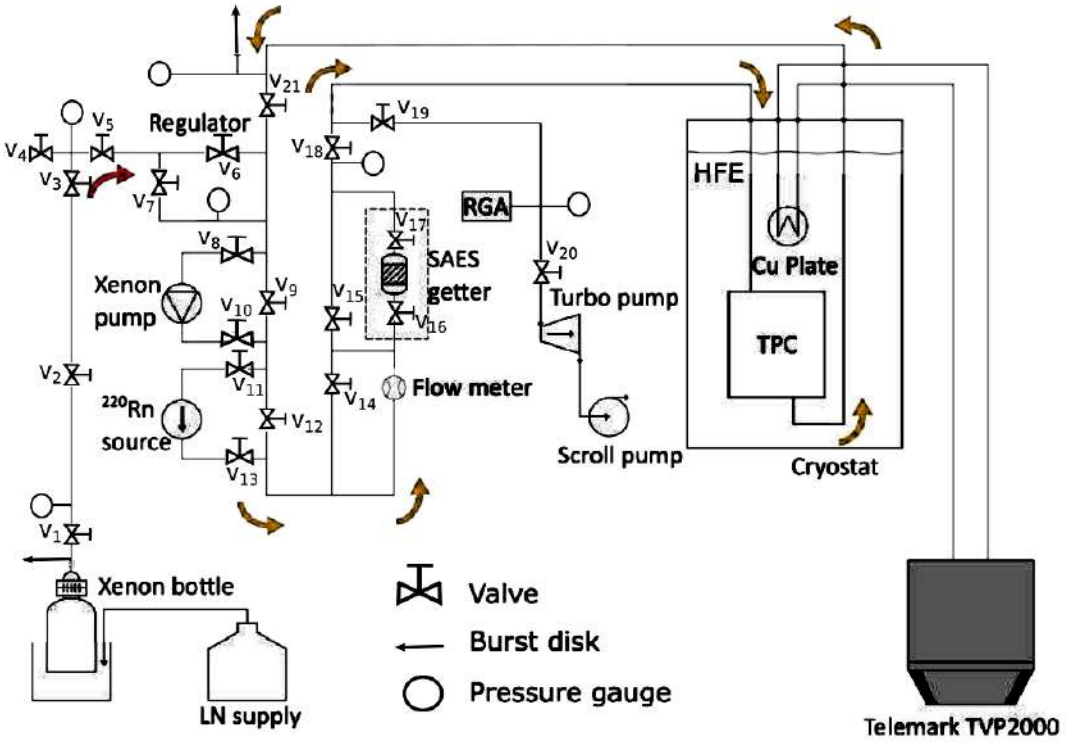

FIGURE 3.9: Schematic diagram of the ^{220}Rn source installed on the Stanford TPC recirculation system in an isolated loop [40].

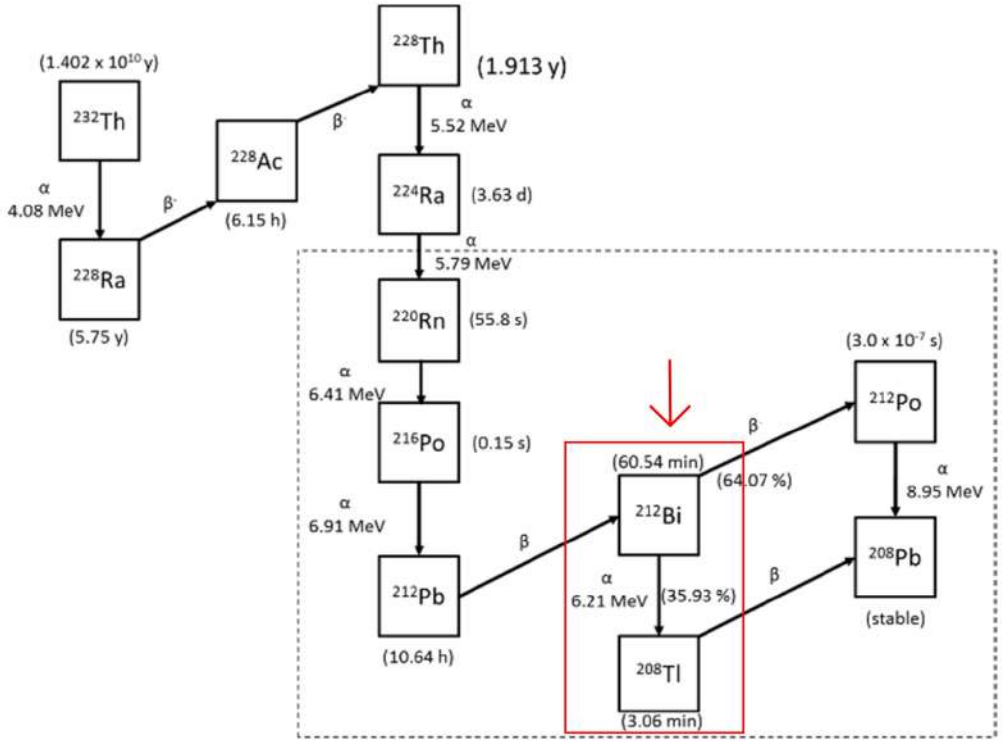

FIGURE 3.10: The ^{220}Rn decay chain, highlighting ^{212}Bi to ^{208}Tl decay. Figure taken from Ref. [43].

each interaction is registered as a pulse. Subsequently, preamplifiers on boards, positioned approximately 10 cm above the TPC feedthroughs on top of the anode, process these pulses. Detailed information about these preamplifiers is available in Ref. [41]. A Phillips Scientific 776 amplifier, located roughly 2 m away from the TPC cryogenic system, further amplifies the signal by a factor of 10. Following this amplification, 16-bit Struck SIS3316 digitizers[6], functioning as analog-to-digital converters (ADCs) are used to digitize the signal. These digitizers obtain charge waveforms which are processed by a python code that extracts several parameters such as charge energy. These charge waveforms are stored in a data acquisition (DAQ) computer.

The waveforms are collected at sampling rates ranging from 10 to 100 MS/s. To address the challenge posed by a large number of charge channels, some channels are grouped together because of a limited availability of digitizer channels. This grouping results in a total of 32 channels, with 31 dedicated to charge and 1 for the SiPMs.

[6]Struck Innovative System, http://www.struck.de/sis3316.html.

Chapter 4

Data analysis and Results

As explained in Chapter 3, the main objective of this work is to measure the Stanford University TPC's energy resolution. The energy resolution is a crucial gauge of a detector's ability to accurately determine the energy distribution of incoming radiation. It may be defined as a dimensionless quantity

$$R = \frac{\text{FWHM}}{\mu}, \tag{4.1}$$

where μ is the centroid of the energy peak and FWHM is its full width at half maximum. For a Gaussian distribution, the FWHM is given by

$$\text{FWHM} \simeq 2.35\sigma, \tag{4.2}$$

where σ is its standard deviation. Therefore, to calculate the energy resolution of the charge-sensitive tile for the TPC, it is necessary to measure both the width and centroid of the energy distribution peak. As a result of electronic noise introduced during the experiment and the ion-screening effect [39] caused by the ionization electrons drifting towards the anode, the effective resolution after noise subtraction, denoted as R_{NS}, is given by

$$R_{NS} \simeq \frac{2.35\sqrt{\sigma^2 - \sigma^2_{\text{noise}}}}{\mu}, \tag{4.3}$$

where σ^2_{noise} are the noise fluctuations subtracted in quadrature. The subsequent sections will use this framework to analyze and evaluate the energy resolution of α signals from the TPC.

4.1 Analysis cuts

Previous studies [44] have shown that when α particles interact with LXe, they produce more scintillation signals compared to ionization. As a result, initial data quality cuts need to be made on the scintillation photon data, shown in Fig. 4.1. The upper panel

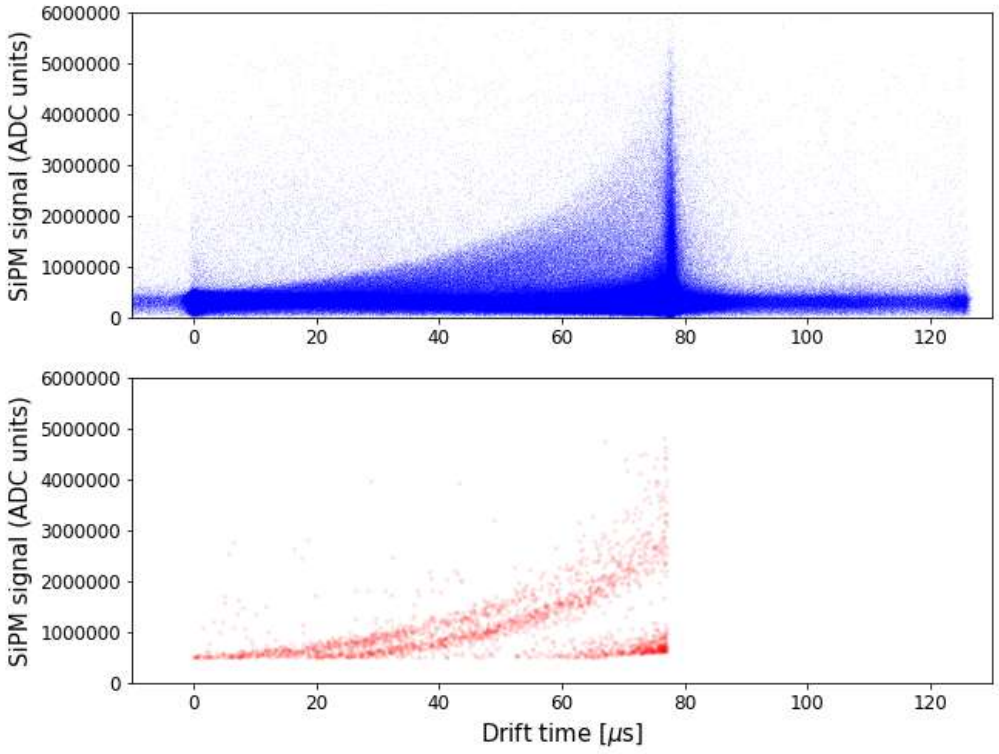

FIGURE 4.1: The top panel (blue) shows the scintillation output (in ADC units) vs drift time, prior to the application of analysis cuts. The bottom panel (red) show the data after implementation of the cuts.

in Fig. 4.1 shows the SiPM signals before applying any analysis cuts. Notably, this plot reveals an exponential rise in scintillation events from 0 μs to approximately 80 μs in drift times[1]. The large concentration of events between ~40 μs and ~80 μs are caused by ^{220}Rn daughters plating out on the cathode surface. This observation aligns with the expectation of more scintillation light near the cathode at the bottom of the TPC, where the SiPMs are located.

The first data-quality cut was performed to eliminate events occurring below 0 μs and above ~78 μs on the x-axis. The 'negative' drift times are registered when the electrons are detected before the trigger signal. In such cases, although the electrons reach the

[1]The drift time represents the time taken for electrons to be collected at the anode.

anode, the events cannot be fully reconstructed because of the delayed response of the SiPMs in recording the events. These events occur within the TPC, but are above the charge-sensitive plane at the anode and below the cathode grid[2]. A second cut was used to remove the noise below 500000 ADC units for the SiPM signals, present as a horizontal band in the upper panel of Fig. 4.1. This was used together with an additional linear cut that only accepted signals with

$$S > 9375t - 100000, \tag{4.4}$$

where t is the drift time. This linear cut further cleaned up the background events near the cathode. The bottom panel in Fig. 4.1 shows the SiPM data after these cuts were applied. In addition, for the charge energy signals, two analysis cuts were applied to ensure that each event only hits two channels (one X tile strip and one Y tile strip) simultaneously per α interaction with LXe, to ensure event localization within the TPC. Another analysis cut was required to ensure that the X and Y channels are single-strip readout channels, by selecting events for which the charge-weighted average position is within ± 20 mm of the center of the tile[3]. These cuts help to improve the energy resolution. Finally, as discussed in Section 4.2.2, one tile strip had excessive noise during the experiment. This required the application of an additional cut to exclude the noisy strip. The charge energy spectrum obtained after applying these analysis cuts is shown in Fig. 4.2. To study the charge energy resolution from α particle interactions, an additional cut was applied to only accept events that had drift times ranging from 20 μs to 60 μs. The lower limit was set at 20 μs to minimize the effects of ion screening [39], while the upper limit of 60 μs further minimized noise contributions from close to the cathode. As mentioned previously, the main contribution to this noise is from ^{212}Pb ions, a byproduct of ^{220}Rn decay, as shown in Fig. 3.10. The charge energy data obtained after the application of all analysis cuts are shown in Fig. 4.3. The dense band corresponds to data from the α branch, resulting from ^{212}Bi decays. Because of the relatively short half-life ($T_{1/2} \simeq 0.3\ \mu s$) of ^{212}Po from the BiPo branch, the BiPo α's are not distinguishable from the electrons following ^{212}Bi β decay.

[2]These regions are outside the active detector volume, which is defined by the drift length, as shown in Fig. 3.4.

[3]This cut made an exception for events from tilestrips X23/24 and Y21/22 because they are close to the single tile strips and also collect charge.

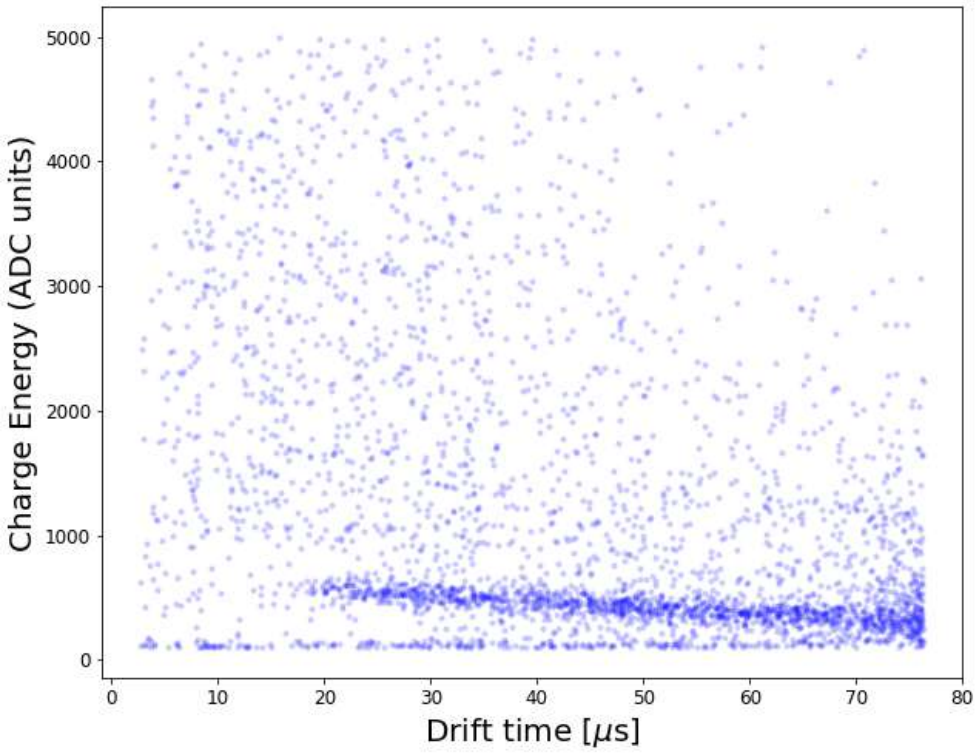

FIGURE 4.2: A 2D histogram of charge energy in ADC units vs drift time. These events arise from BiPo and alpha branch interactions. The dense band below 1000 ADC units are from the alpha branch interactions, as the ionization is localized for such events. The other events are mainly from the BiPo branch.

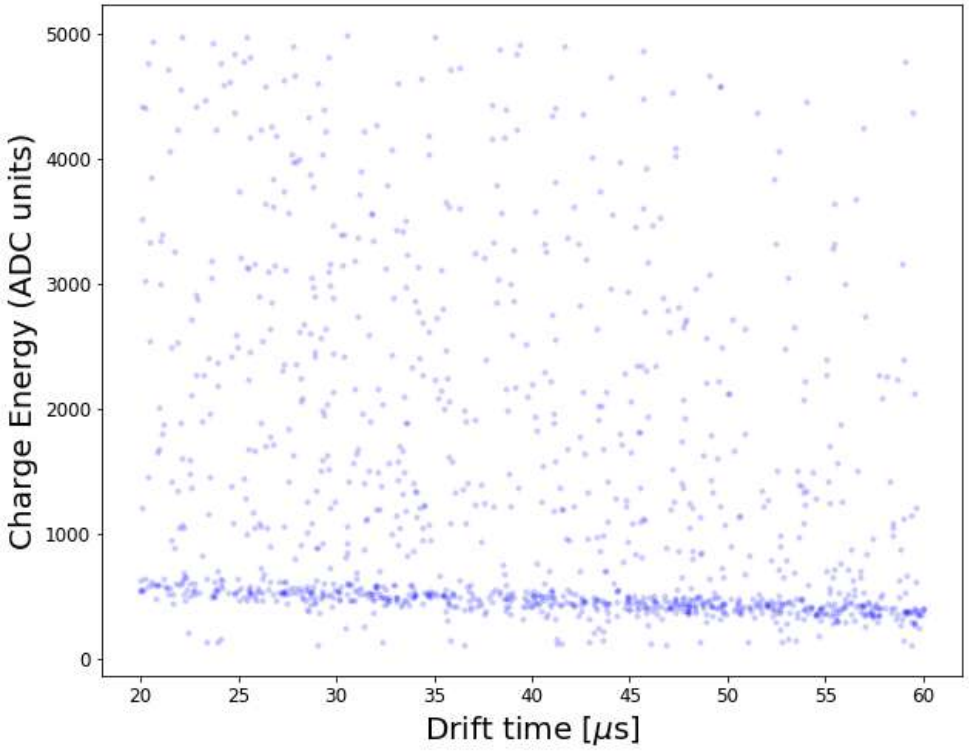

FIGURE 4.3: Final 2D charge-energy histogram after all the analysis cuts have been applied. The dense band below 1000 ADC units will be studied. This band mainly arises from the charge energy detected by the anode.

4.2 Electron lifetime measurement

Electronegative impurities within the LXe TPC worsen the energy resolution by affecting charge collection efficiency at the anode plane. Consequently, it is imperative to model the time that free electrons take on average, before they attach to impurities within the LXe. This electron "lifetime" depends on both the concentration of electronegative impurities and the drift field [45]. Consequently, the measured charge energy $Q_{meas}(t)$ is expressed as

$$Q_{meas}(t) = Q_0 e^{-\frac{t}{\tau_e}}, \tag{4.5}$$

where t is the drift time, Q_0 is the initial number of ionization electrons, and τ_e is the electron lifetime. As a result, the next step in our data analysis required a correction to our data for the electron lifetime. This requires a measurement of τ_e. We achieved this by binning the data shown in Fig. 4.3, into five 7 μs intervals in drift time. The 1D projections of the charge-energy data, for two such time intervals are shown in Fig. 4.4. Additional plots are listed in Appendix A. The scattered events in these

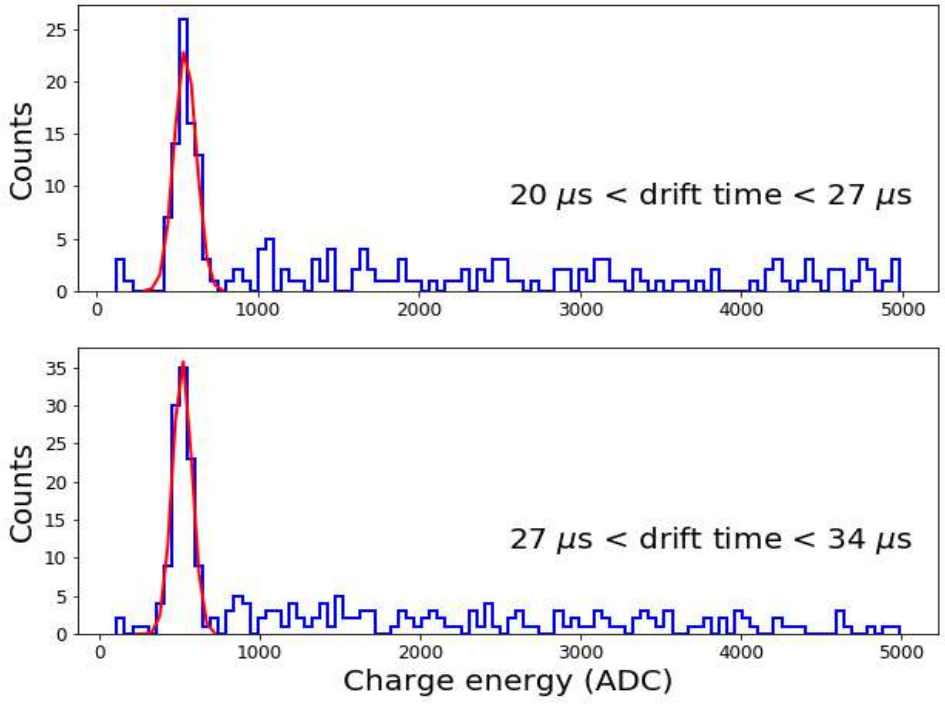

FIGURE 4.4: 1D projections for the data corresponding to Fig. 4.3, for different time intervals.

plots are background from both β and α events from the BiPo branch. Neglecting this

background, we fitted each charge energy peak with a Gaussian distribution

$$f(x) = ae^{-\frac{(x-\mu)^2}{2\sigma^2}}, \tag{4.6}$$

where a is the normalization constant, μ is the centroid, and σ is the standard deviation. The extracted centroids were plotted against mean drift time of each bin. These data are shown in Fig. 4.5. They were fit to a model described by Eqn. (4.5). The electron lifetime extracted from this fit was $\tau_e = 91.9 \pm 5.8$ μs.

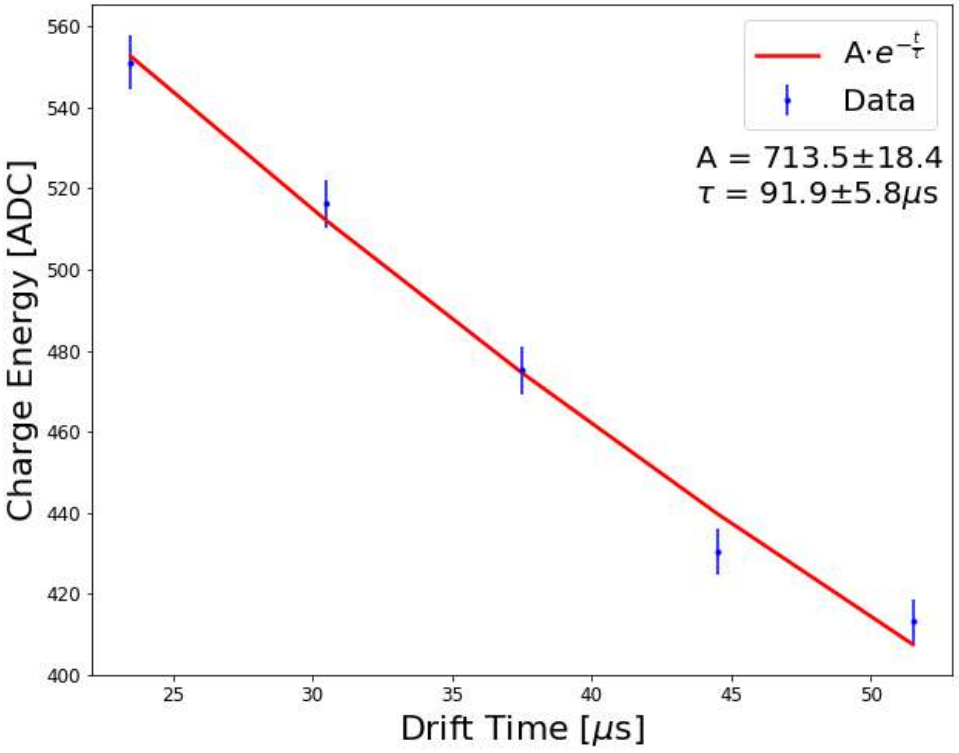

FIGURE 4.5: The electron lifetime, τ_e in the Stanford TPC, extracted from the charge tile data shown in Fig. 4.3.

4.2.1 Charge Reconstruction

The measured τ_e from the preceding section was used to reconstruct Q_0 via Eqn. (4.5). This reconstructed 2D histogram of charge energy is shown in Fig. 4.6, whose 1D histogram of charge energy projection is shown in Fig. 4.7. Similarly as before, a Gaussian distribution was used to fit the charge-energy peak in Fig. 4.7. The following parameters

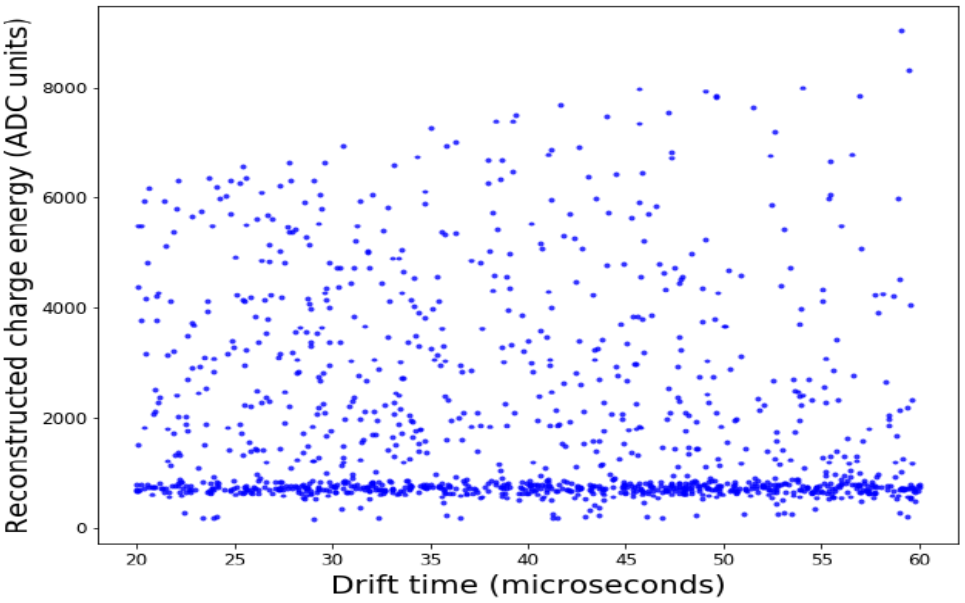

FIGURE 4.6: 2D Histogram for charge energy vs drift time after correcting for the electron lifetime. As mentioned previously, the band below 2000 ACD units will be studied as these data correspond to 6 MeV α's from the source interacting with LXe.

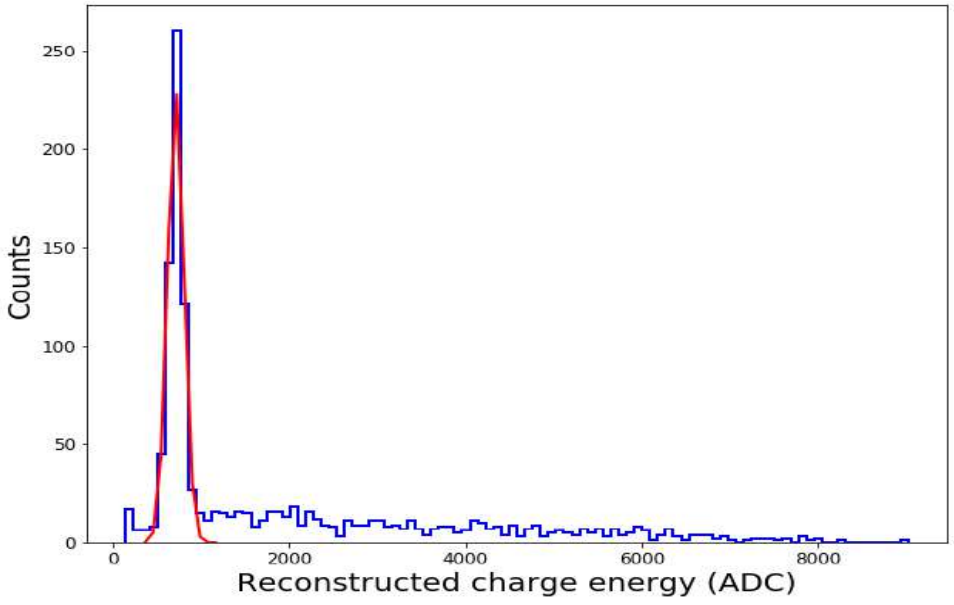

FIGURE 4.7: Projected charge energy spectrum from Fig. 4.6.

were extracted

$$\mu = (717.2 \pm 8.0) \text{ ADC units} \; ; \quad \sigma = (92.3 \pm 6.4) \text{ ADC units}, \tag{4.7}$$

The other remaining task in this analysis is removing the contribution of electronic noise as per Eqn. (4.3).

4.2.2 Noise measurements

The electronic noise in each charge tile was measured using the same procedure described in Section 4.1. The plots in Fig. 4.8 show example charge-energy noise spectra for two tile strips, X13 and X14. Additional plots are listed in Appendix B. The peaks at

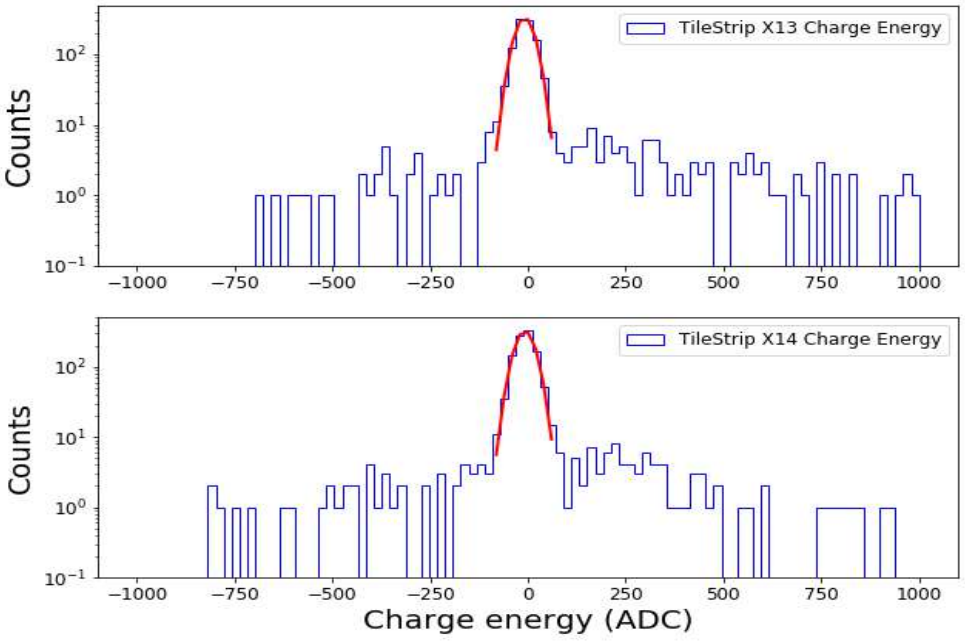

FIGURE 4.8: Charge energy spectrum for a single channel, with a Gaussian fit to the noise peak at 0 ADC units.

0 ADC units correspond to the noise in these strips. These peaks were also fitted with Gaussians to extract the σ_{noise} for each channel. The σ_{noise} obtained from each tile strip are shown in Fig. 4.9. As mentioned previously in Section 4.1, strip X19 was excluded from our analysis because of excessive noise. The final electronic noise contribution was calculated using a weighted average

$$\sigma_{\text{noise}} = \frac{\sum_{i=1}^{n} (1/\delta_i^2) \cdot \sigma_i}{\sum_{i=1}^{n} 1/\delta_i^2}, \tag{4.8}$$

where δ_i^2 are the variances of each σ_i, obtained from their individual Gaussian fits. This procedure yields

$$\sigma_{\text{noise}} = (38.9 \pm 0.2) \text{ ADC units.} \tag{4.9}$$

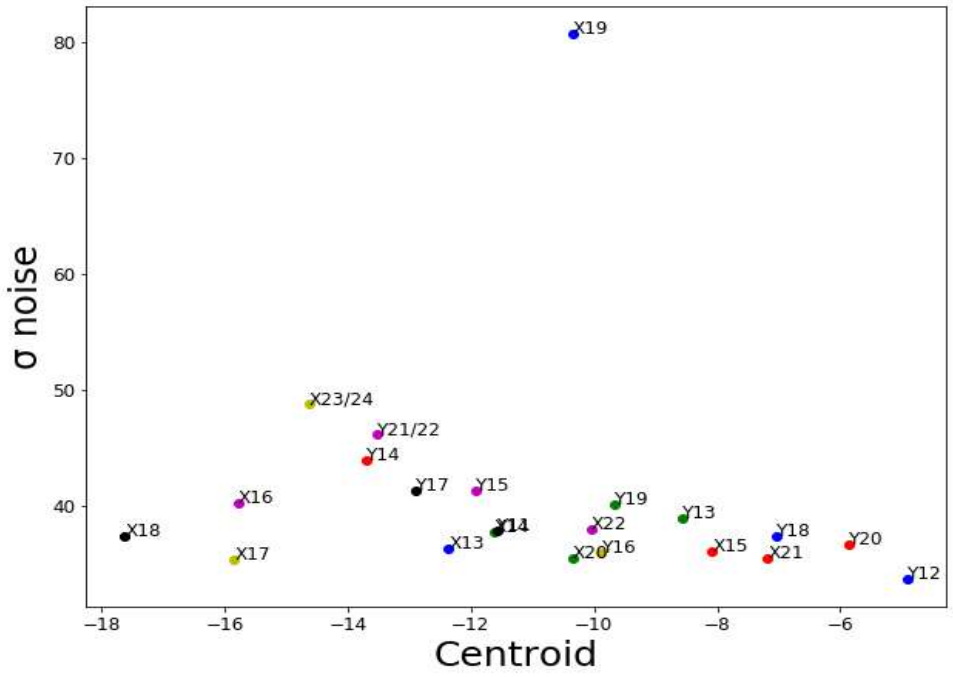

FIGURE 4.9: σ_{noise} obtained for each tile strip, also showing the noisy strip X19.

4.2.3 Energy Resolution

The noise-corrected energy resolution was finally determined using Eqn. (4.3), from the extracted parameters listed in Table 4.1. This yields the noise subtracted energy resolution (R_{NS}) to be

$$R_{NS} = (27.0 \pm 2.3)\%. \tag{4.10}$$

Measured parameters			
σ (ADC units)	σ_{noise} (ADC units)	μ (ADC units)	R_{NS} (%)
92.3 ± 6.4	38.9 ± 0.2	717.2 ± 8.0	27.0 ± 2.3

TABLE 4.1: Measured parameters to determine the energy resolution for 6 MeV α's in the Stanford LXe TPC.

4.3 Comparison with simulations

Our extracted resolution is found to be inconsistent with previous measurement in Ref. [46], as shown in Fig. 4.10. To investigate possible reasons for this discrepancy, we further performed a set of simulations, which are described below. Two simulation programs were used.

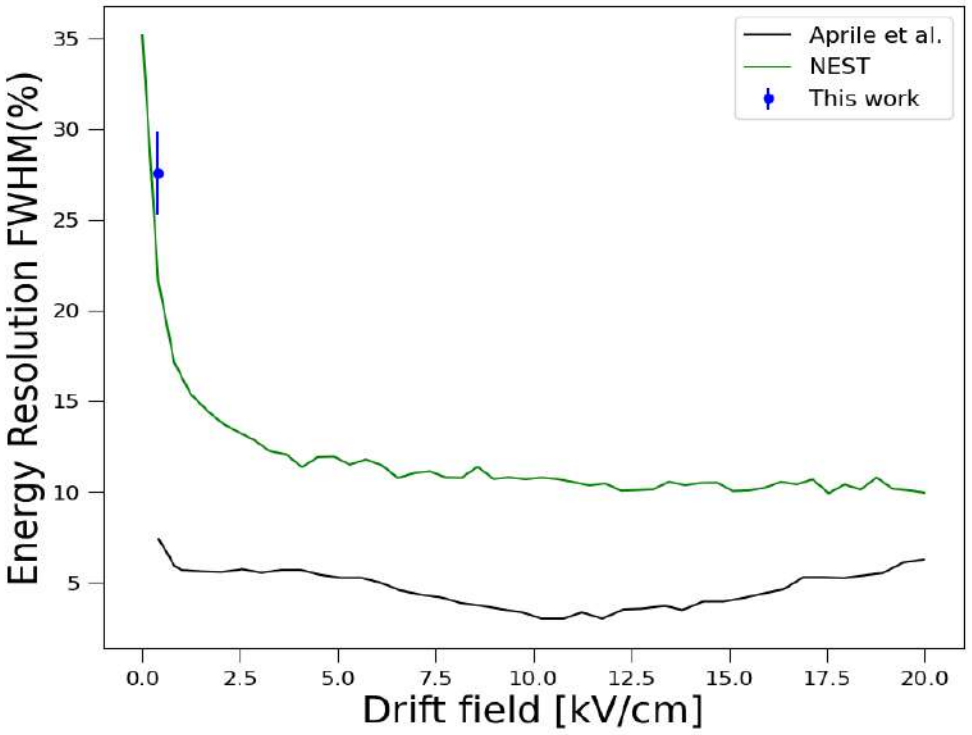

FIGURE 4.10: This figure shows the inconsistency between NEST predictions and the experimental data from Aprile *et al.* [46]. On the other hand, our measured value is in reasonable agreement with the NEST results. Our study is limited to a drift field of 400 V/cm, considering its relevance to nEXO's future implementation.

4.3.1 NEST simulations

The noble element simulation technique (NEST) software package, initially developed as NEST v0.98 [47, 48] employs a semi-empirical model to simulate scintillation photons and ionization electrons within liquid LXe and other noble elements [47–49]. The photons and ionization electrons are then propagated to collection channels. The signals from ionization and scintillation channels are modeled based on the applied electric field within the TPC and the energy of the radiation deposited. NEST has found widespread application in various experiments, and serves as a useful tool to interpret experimental data [50–52]. For our experiment, we used NEST v2.3.12 to predict the energy resolution for charge-only events when 6 MeV α particles interact with LXe under an electric field of 400 V/cm, within a virtual TPC. This prediction serves as a foundation for comparison with other data and an analysis of our results. To ensure effective comparison, we used WebPlotDigitizer[4] to extract experimental energy resolution data, obtained with 5.3 MeV α's from a ^{210}Po source within LXe, as measured in Ref. [46]. Fig. 4.10 shows

[4]WebPlotDigitizer is an online tool used to extract data from 2D-plots, for more information refer to https://automeris.io/WebPlotDigitizer.

these data plotted against the drift field. These results are compared with ours, and the prediction from a NEST simulation. It is clear from the figure that NEST fails to reproduce the results observed in Ref. [46], while being in agreement with our experimental findings. To further investigate the reasons behind this discrepancy, we conducted an additional simulation, detailed in the subsequent section.

4.3.2 The *nexo-offline* simulations

The second simulation uses a GEANT4-based package known as the *nexo-offline*. In this simulation, we used a uniformly distributed ^{212}Bi source inside the Stanford LXe TPC. The *nexo-offline* simulation package simulates the charge tile response of the prototype TPC during operation. It inputs the TPC geometry, the detector medium, the electron lifetime, the interacting particles (α's), and their energy. This simulation has the capability to integrate NEST[5] [53, 54] into the package, for generating ionization electrons and scintillation photons within the detector. It produces charge waveforms as the ionization electrons get detected at the anode plane. These simulated waveforms are generated using a high-performance computing cluster at LLNL and stored as ROOT [55] files. The waveforms do not incorporate electronic noise. To include such noise actual data needed to be acquired with the TPC. This was done independently, in the absence of LXe in the TPC. In this procedure, a pulser signal was used as an input to the cathode. After detecting the induced charge pulses on the charge tiles, a database of 10^5 "real noise" waveforms were collected using a digitizer. These waveforms were grouped together to match the tile strips at the charge-collecting plane. Then they were randomly selected from the database and added to the simulated charge waveforms. Fig. 4.11 shows the simulated waveform outputs with and without this experimental noise.

Next, we used a Python code to process these files and extract the charge energy, in a similar manner to the experimental data analysis. By applying the same data quality cuts as in our experimental data (see Section 4.1), we produced the simulated data in Fig. 4.12, which shows events from both the α and BiPo branches. An electron lifetime value of $\tau_e = 100$ μs was input into the simulation, based on our experimental measurement. Similar to the experimental data, we binned these data in different intervals for the drift time, as shown in Fig. 4.13. A exponential fit to these data yielded

$$\tau_e = (100.5 \pm 3.0)\ \mu\text{s}, \tag{4.11}$$

[5]The *nexo-offline* simulation package uses a modified version of NEST that minimizes the intrinsic fluctuations of charge produced by α-particles, by eliminating fluctuations due to recombination.

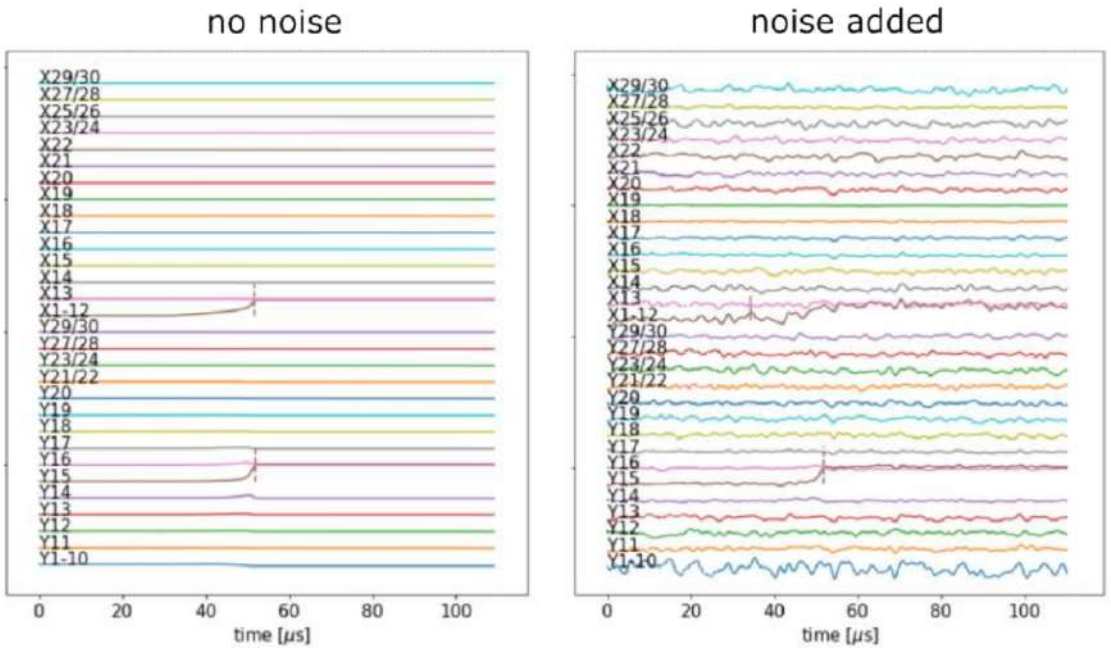

FIGURE 4.11: Simulated waveforms from an α energy deposition. Left panel: Without electronic noise. Right panel: With electronic noise added [40].

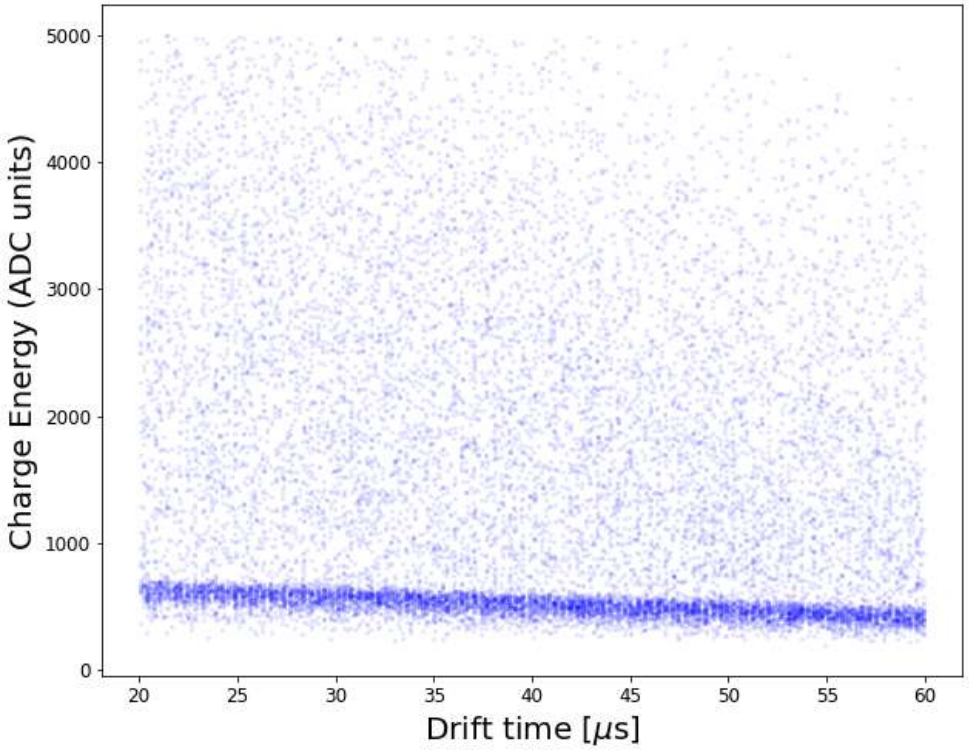

FIGURE 4.12: Simulated 2D histogram for charge energy vs drift time, after all the analysis cuts are applied.

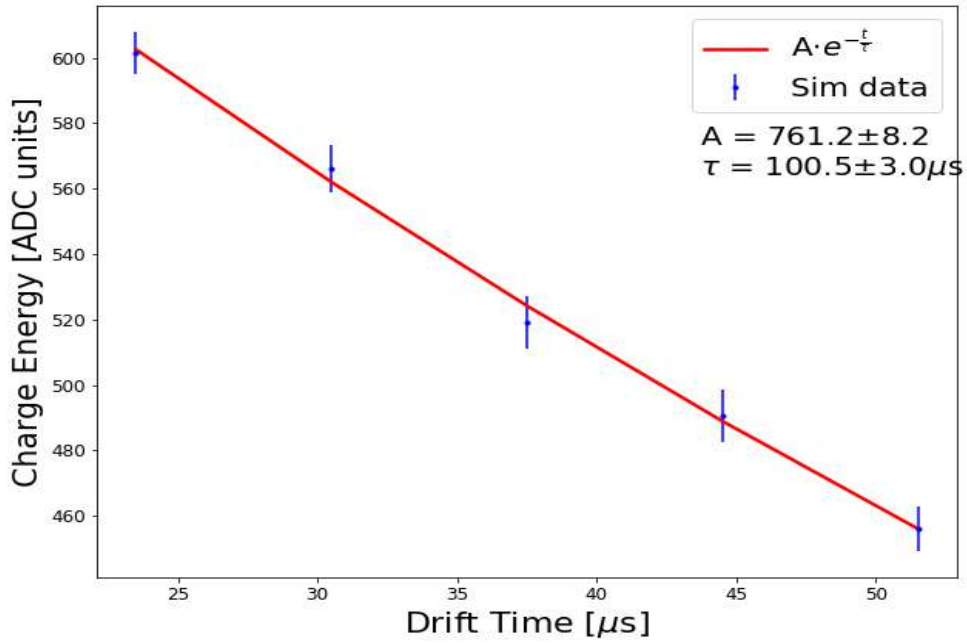

FIGURE 4.13: τ_e determination from the simulated data.

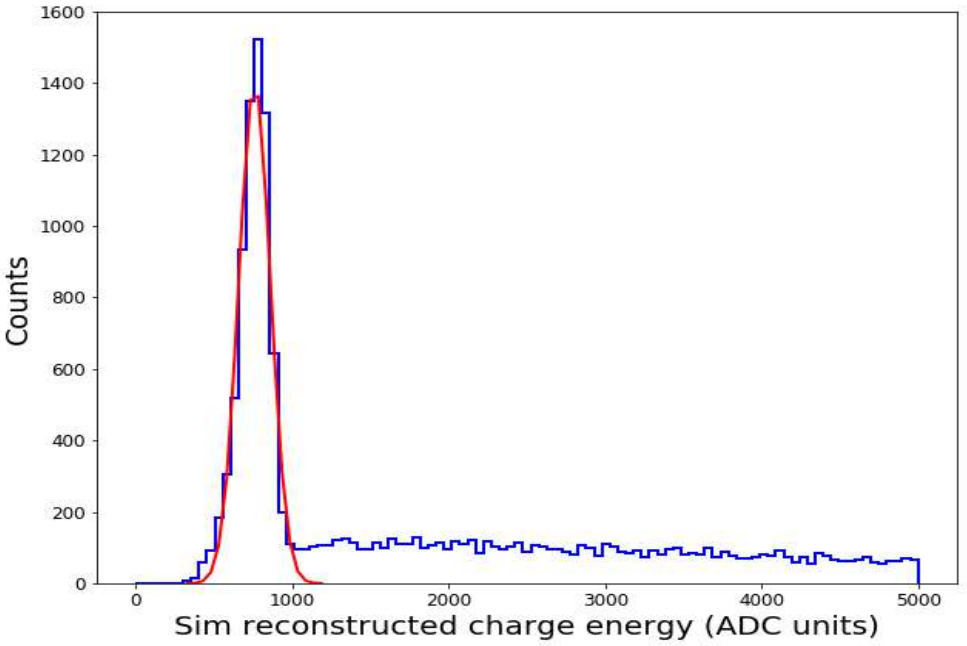

FIGURE 4.14: The simulated charge energy spectrum reconstructed using the value for the electron lifetime. These data correspond to 5×10^5 ^{212}Bi decays.

which agreed with the input value and validated our analysis. This value of the electron lifetime ($\tau_e = 100$ μs) was used for charge reconstruction. Fig. 4.14 shows the

reconstructed charge energy. A Gaussian fit to peak yielded parameters

$$\mu_{\text{Sim}} = (759.22 \pm 7.88) \text{ ADC units} ; \quad \sigma_{\text{Sim}} = (101.09 \pm 6.45) \text{ ADC units.} \tag{4.12}$$

Before calculating the energy resolution, it was important to remove the electronic noise that were added to the simulated charge waveforms. We achieved this similarly as with the experimental data (see Section 4.2.2). A weighted average for all charge tiles determined the simulated σ_{noise} to be

$$\sigma_{noise} = (40.05 \pm 0.12) \text{ ADC units.} \tag{4.13}$$

This yields an energy resolution $R_{NS} = (28.73 \pm 2.19)\%$. As illustrated in Fig. 4.15, this aligns with our experimental result but differs from the results by Aprile *et al.* [46].

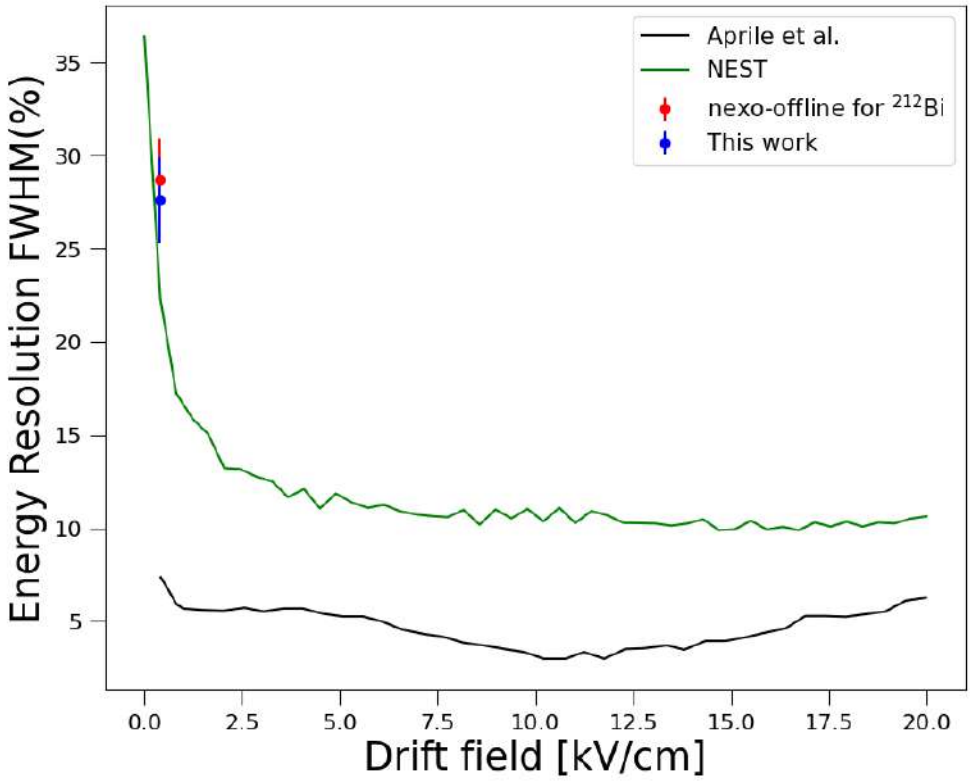

FIGURE 4.15: The energy resolution obtained from *nexo-offline* compared with experimental measurements and NEST predictions.

This discrepancy necessitated further investigation, which was done via a waveform analysis. As discussed previously, the waveforms were stored as ROOT files, and one

Simulation results for a ^{212}Bi source			
σ_{Sim} (ADC units)	σ_{noise} (ADC units)	μ_{Sim} (ADC units)	R_{NS} (%)
101.09 ± 6.45	40.05 ± 0.12	759.22 ± 7.88	28.73 ± 2.19

TABLE 4.2: Measured parameters from the *nexo-offline* simulation data.

can extract the simulated thermal electrons[6] from the ROOT file trees. Fig. 4.16 shows this information, plotted as the simulated charge (n_e) released via ionization. In the top panel, the spectrum shows two peaks instead of a single peak that one would expect from the α branch. To investigate this further, we re-ran the simulation using monoenergetic

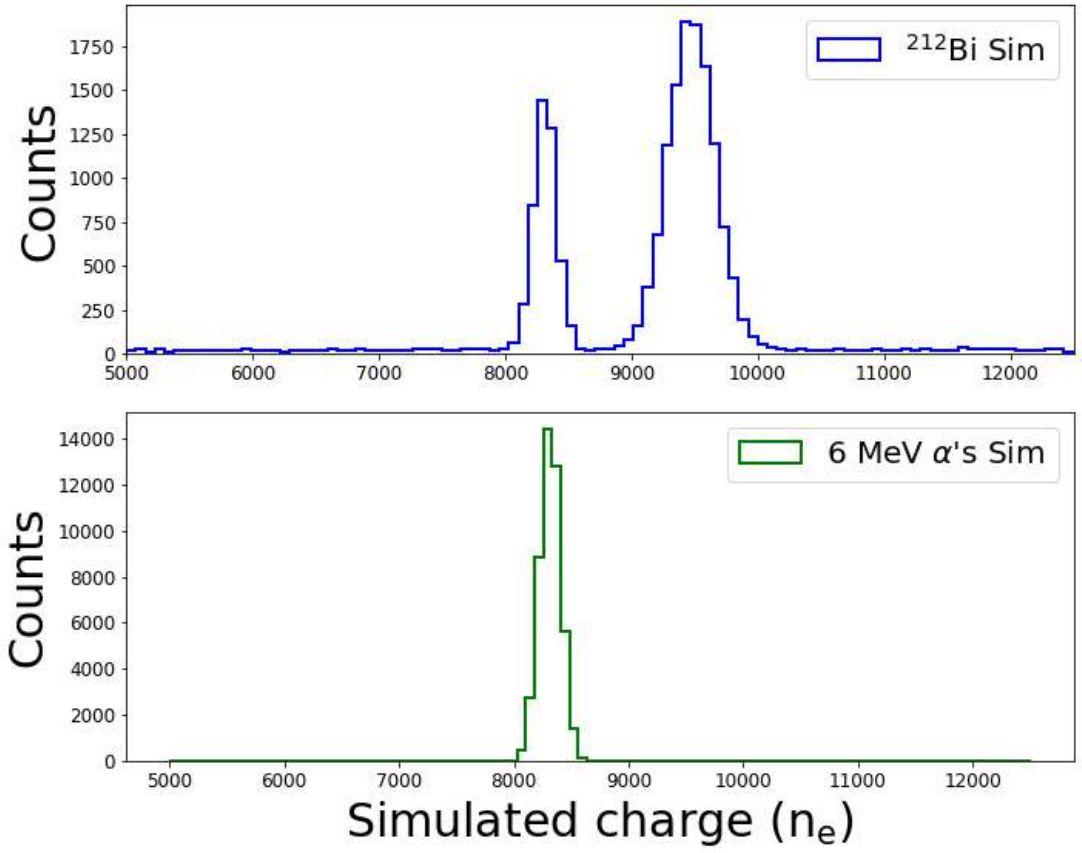

FIGURE 4.16: The top panel shows the spectrum of the simulated charge energy when a ^{212}Bi source is simulated in the *nexo-offline* simulation. The bottom panel shows the peak for 6 MeV α's, instead of the ^{212}Bi source. It is clear that the first peak is from the alpha branch.

6 MeV α particles, instead of ^{212}Bi as a source. As shown in bottom panel of Fig. 4.16, the latter simulation produced one peak that matches the peak on the left from the source simulation. This led us to identify the first peak, which corresponds to ionization from the α branch. To identify the second peak, we examined the α decay scheme for the nucleus, shown in Fig. 4.17. This suggests that the second peak may arise due to the γ-

[6]Thermal electrons are the ionization electrons released when the particles interact with LXe.

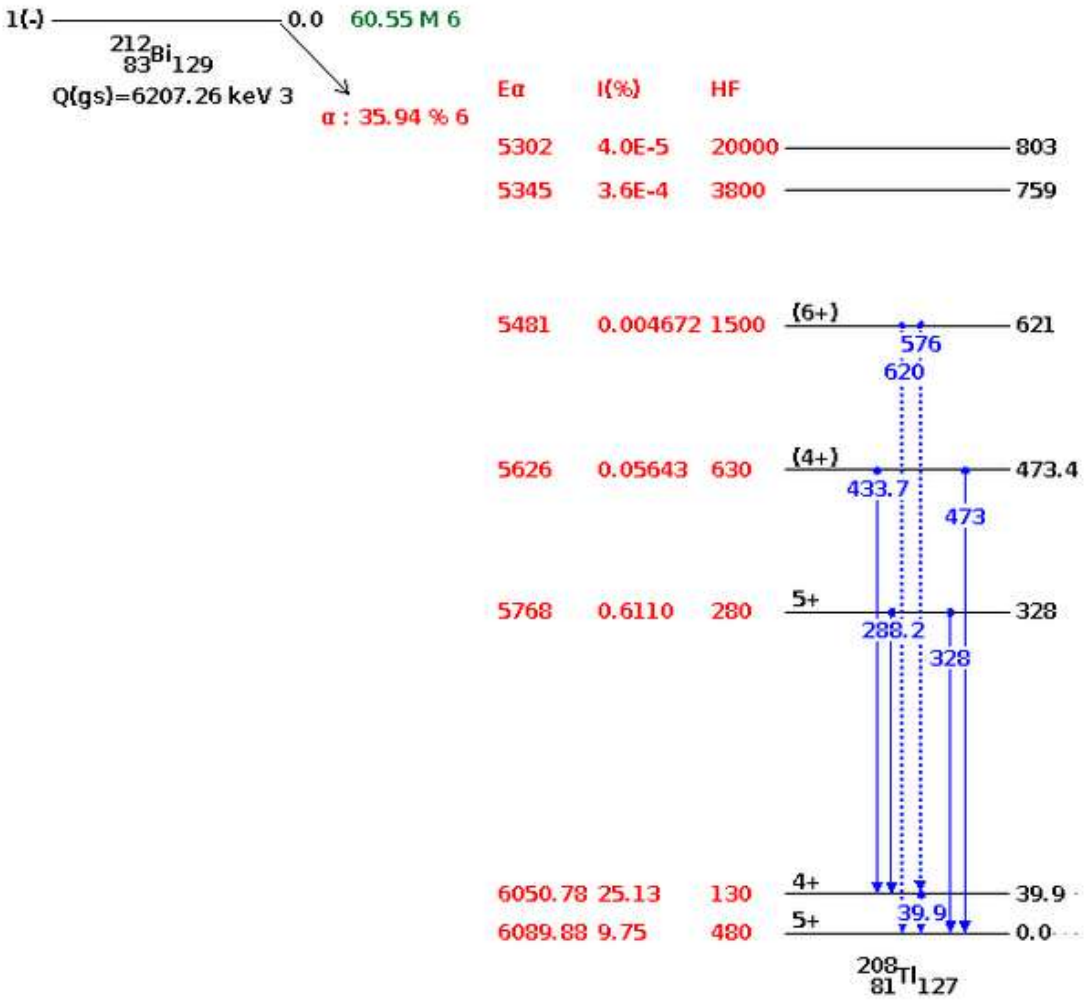

FIGURE 4.17: ^{212}Bi α decay scheme from NuDat3 [56]

ray feeding from excited states of ^{208}Tl. To verify this possibility, we ran a Monte Carlo simulation in NEST, which performed 10^5 decays of ^{212}Bi to ^{208}Tl, considering the decay branches to various excited states of ^{208}Tl, as shown in Fig. 4.17. In each simulation, the code was used to randomly select a decay path, based on known α branching ratios. After determining the decay path, the code computed the electron yields separately for the α's and the γ's emitted during the decay. The sum of both gives the total yield, as shown in the right panel of Fig. 4.18. For a more effective comparison with a histogram similar to the *nexo-offline* data, we used the Box-Müller method [57], to obtain Gaussianly smeared data for the electron yield, with a standard deviation that is $\sqrt{N}$, where N is the electron yield. These results are shown in Figs. 4.19 and 4.20. The offset between the top and the bottom panels of Fig. 4.20 is most likely because of the differences between the NEST and *nexo-offline* simulations. These results led us to conclude that the second peak on the right is caused by the summed effect of 6 MeV α's and 40 keV γ's (from the first excited state in ^{208}Tl), interacting with the LXe.

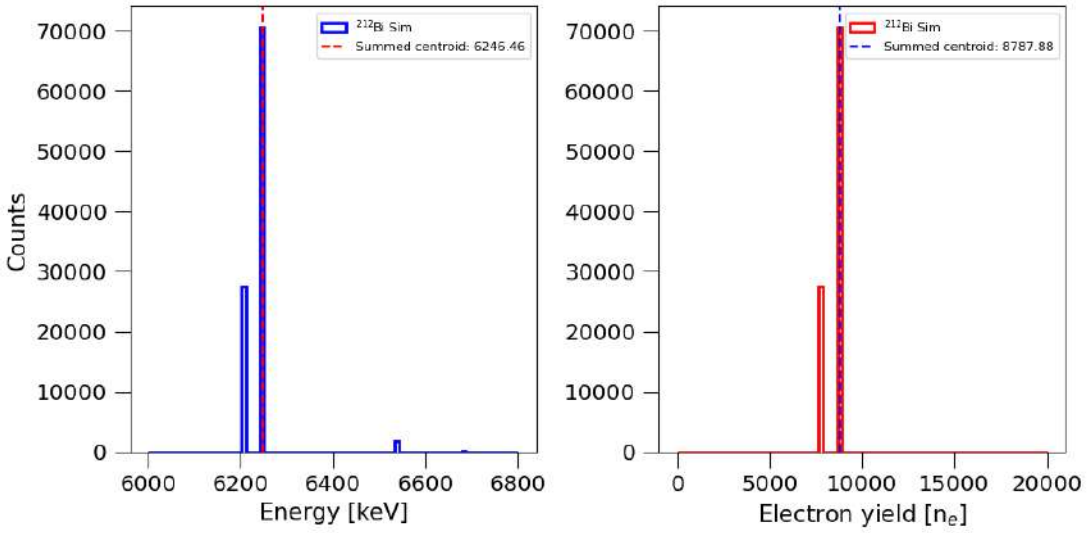

FIGURE 4.18: Left panel: Individual α and summed α and γ energies used in the NEST simulation. The right peak is from summing with 40 keV γ-rays. Right panel: From the same simulation, ionization electron yields for the α energies, compared with the yields when both α and γ energies are summed together.

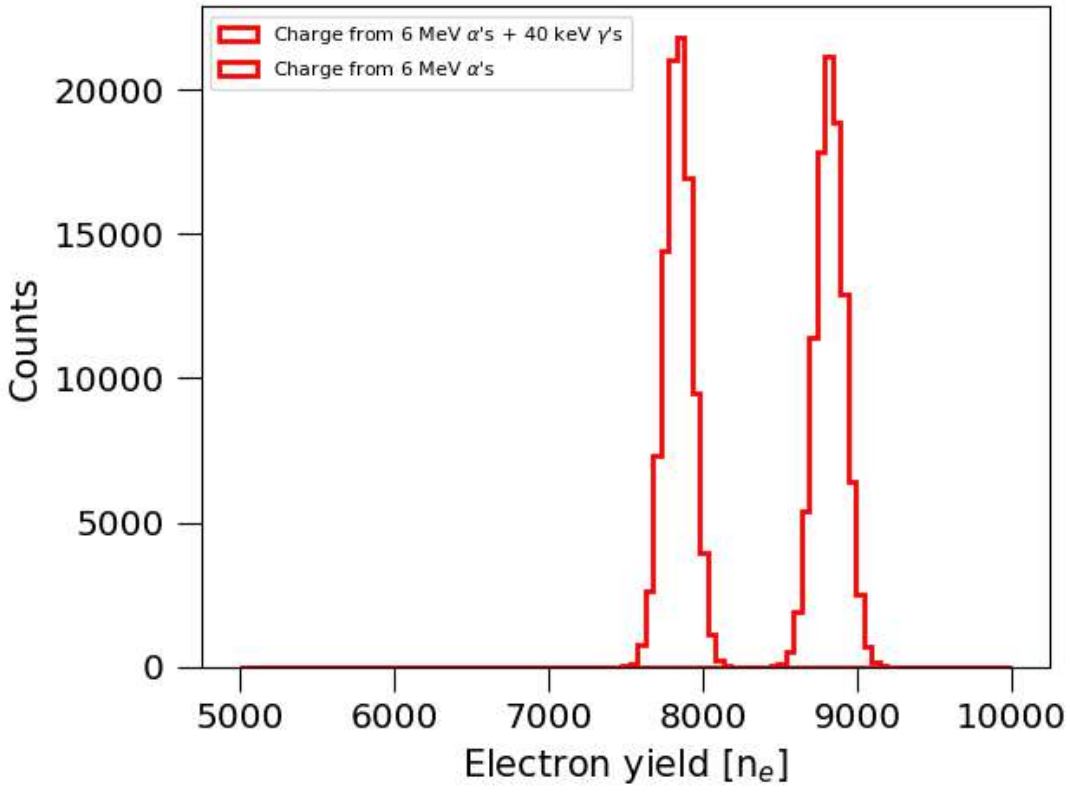

FIGURE 4.19: The results in Fig. 4.18, with smeared Gaussian widths.

Having confirmed that the *nexo-offline* simulated charge energy for the decay of ^{212}Bi is affected by summing with γ-rays, it was important to establish if this was the reason for the discrepancy observed in Fig. 4.15. For this we revert back to the monoenergetic

Simulation results for 6 MeV α's as a source			
σ_{Sim} (ADC units)	σ_{noise} (ADC units)	μ_{Sim} (ADC units)	R_{NS} (%)
65.95 ± 2.39	37.88 ± 0.12	698.0 ± 2.4	18.18 ± 0.98

TABLE 4.3: Measured parameters from the *nexo-offline* simulations when 6 MeV α's were used.

α's simulated in *nexo-offline*, as shown in the bottom panel of Fig. 4.16. These data were analyzed by applying the same data quality cuts as in our experimental data and a charge reconstruction using an electron lifetime of 100 μs. This produced the simulated charge energy data for 6 MeV α's, as shown in Figs. 4.21 and 4.22. The 1D projection of the reconstructed charge energy (shown in Fig. 4.22), was fitted with a Gaussian distribution. The peak width and the centroid were determined as

$$\mu_{\text{Sim}} = (698.0 \pm 2.4) \text{ ADC units} \; ; \quad \sigma_{\text{Sim}} = (65.95 \pm 2.39) \text{ ADC units}. \tag{4.14}$$

Upon removing electronic noise similarly as before, it is found that for this case

$$R_{NS} = (18.18 \pm 0.98)\%. \tag{4.15}$$

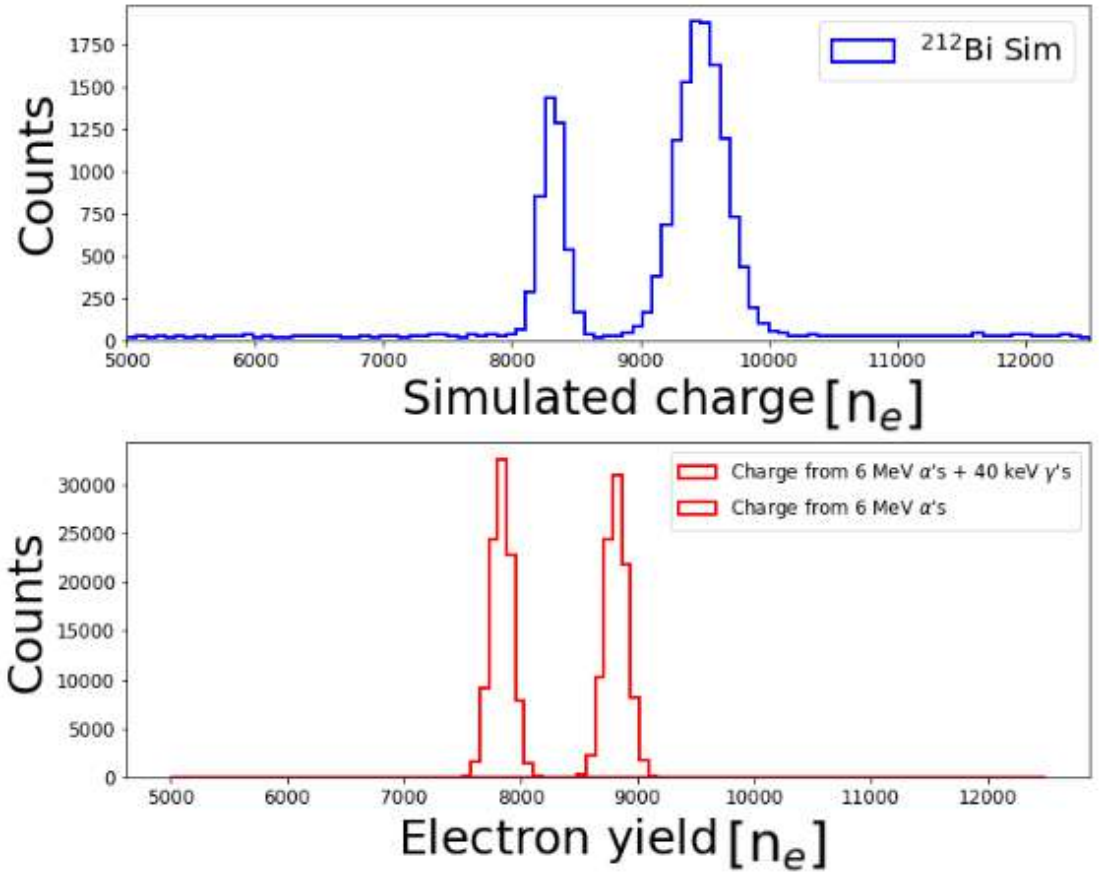

FIGURE 4.20: Comparison of NEST generated electron yields shown in Fig. 4.19 and the *nexo-offline* simulated charge for ^{212}Bi decays in LXe.

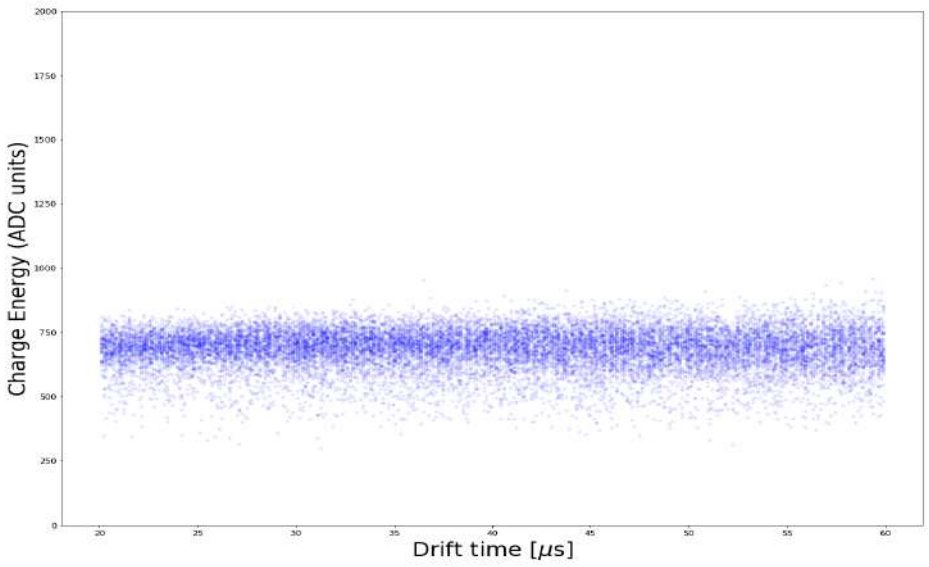

FIGURE 4.21: 2D histogram for charge energy vs drift time when the ^{212}Bi source in the *nexo-offline simulation* is replaced with the 6 MeV α particles uniformly distributed inside the TPC. These data are produced after all the analysis cuts have been made, similar to our experimental data.

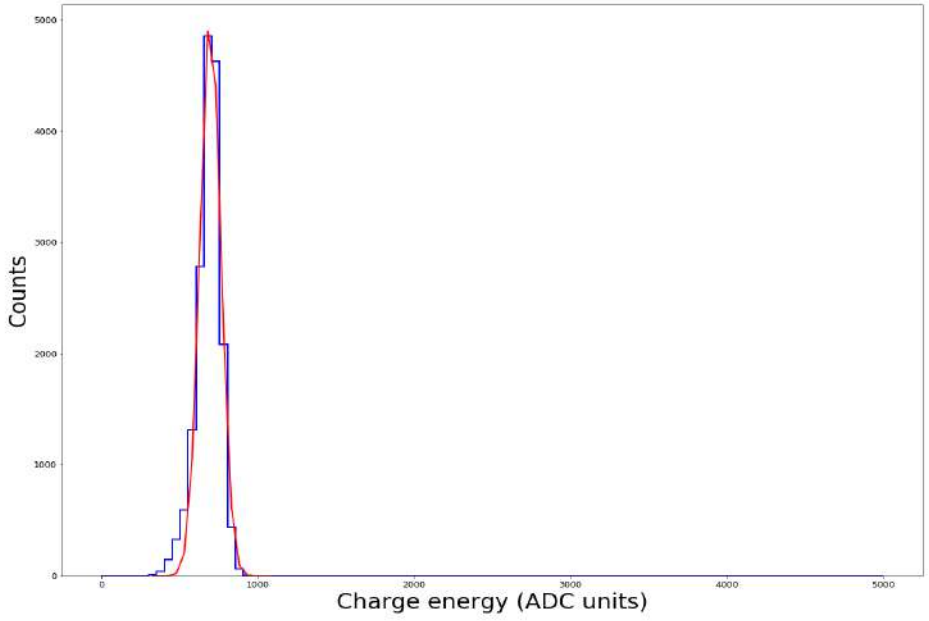

FIGURE 4.22: The reconstructed charge energy spectrum for 6 MeV α's as a source in *nexo-offline* simulations.

The extracted parameters from these simulations are shown in Table. 4.3, which show that the noise-subtracted resolution is still significantly worse than the one reported in Ref. [46]. This is illustrated in Fig. 4.23. This result may be compared to the one obtained when no electronic noise waveforms were added to the *nexo-offline* simulations, which yielded

$$R = (3.94 \pm 0.06)\%. \tag{4.16}$$

This value is significantly lower. Our observations suggest three possibilities

- Based on our method for the removal of electronic noise, it is possible the noise is not entirely removed in our analysis.
- There might be some additional unknown source of noise in the simulations.
- The measured electronic noise is not entirely added to the waveforms because of unknown and unresolved errors in the code.

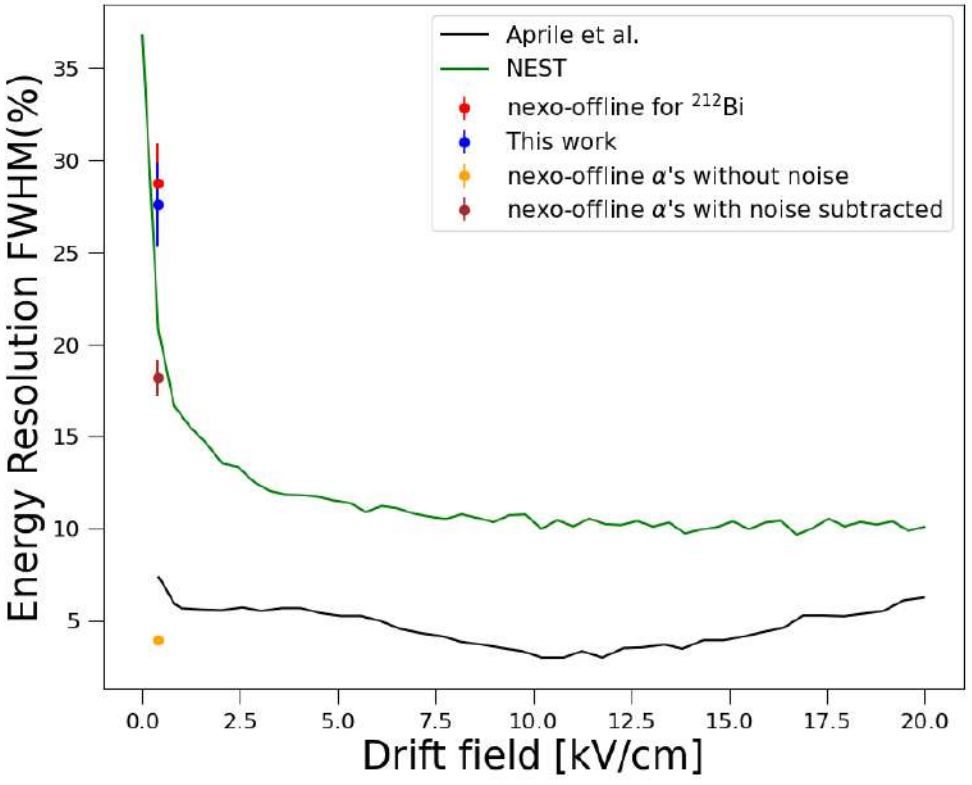

FIGURE 4.23: Our measured experimental resolution compared with previous measurements and various simulated values.

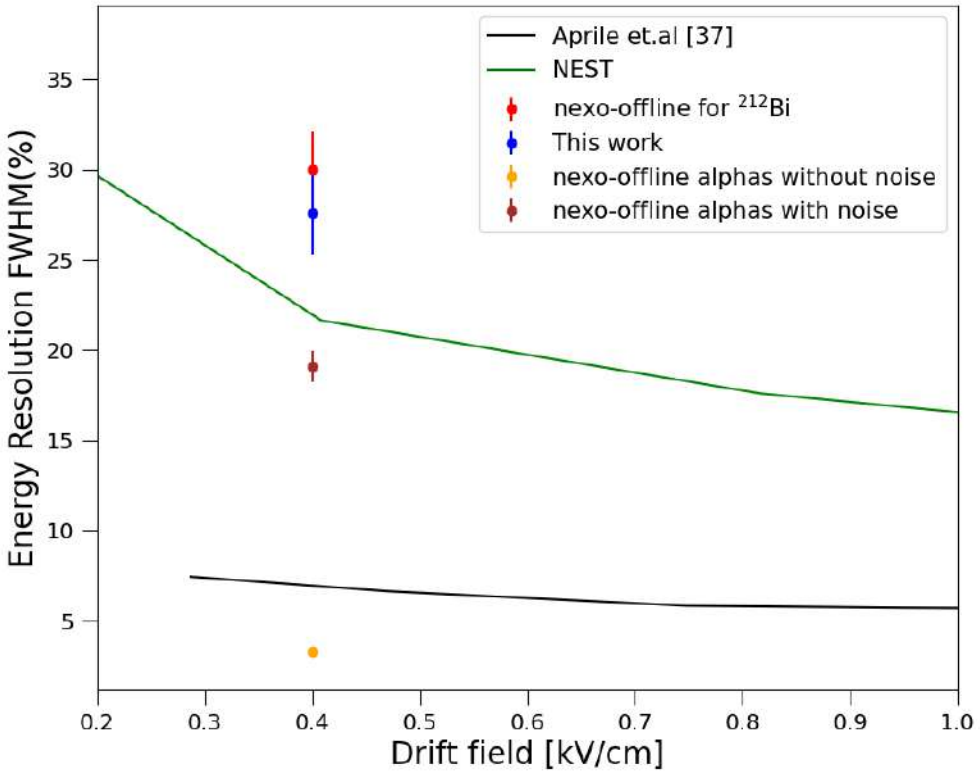

FIGURE 4.24: Zoomed version of Fig. 4.23, in the range $0 - 1$ kV/cm

Chapter 5

Conclusions and Future work

This work used radioactive source measurements in a LXe TPC to study the intrinsic charge-only energy resolution of 6 MeV α-signals. These α-particles are from a ^{232}Th calibration source, produced via the decay of ^{212}Bi $\rightarrow$ ^{208}Tl. We measured the charge-only energy resolution to be $(27.0 \pm 2.3)\%$ for this case. The obtained energy resolution is inconsistent with an independent measurement [46] with a ^{210}Po source in a parallel plate ionization chamber filled with LXe. We performed simulations with two programs, *nexo-offline* and NEST, which showed that one of the reasons for this discrepancy is that ^{212}Bi decays to excited states of ^{208}Tl, and the γ-rays emitted during the de-excitation of ^{208}Tl add a second unresolved charge-energy peak. Another likely contribution to this discrepancy is from a possible inefficient removal of electronic noise in our analysis.

5.1 Future work

Despite our efforts described here, the discrepancy between our simulated results, and the measurements by Aprile *et al.* [46] and our experimental measurement remains unresolved. To address this issue, in future work we plan to explore the charge-only energy resolution at different drift fields, with a possible investigation of how the simulations reproduce ^{210}Po α interactions with LXe in a TPC. Additionally, efforts will be made to find alternative methods to remove electronic noise more effectively, and to check if there is indeed any additional source of noise contribution in the simulation that was missed in our analysis. Another possibility is an inefficient method of noise addition to the simulated waveforms, which makes us underestimate the amount of noise that needs to be subtracted.

Appendix A

Electron lifetime measurement plots

A.1 Charge energy Spectrum

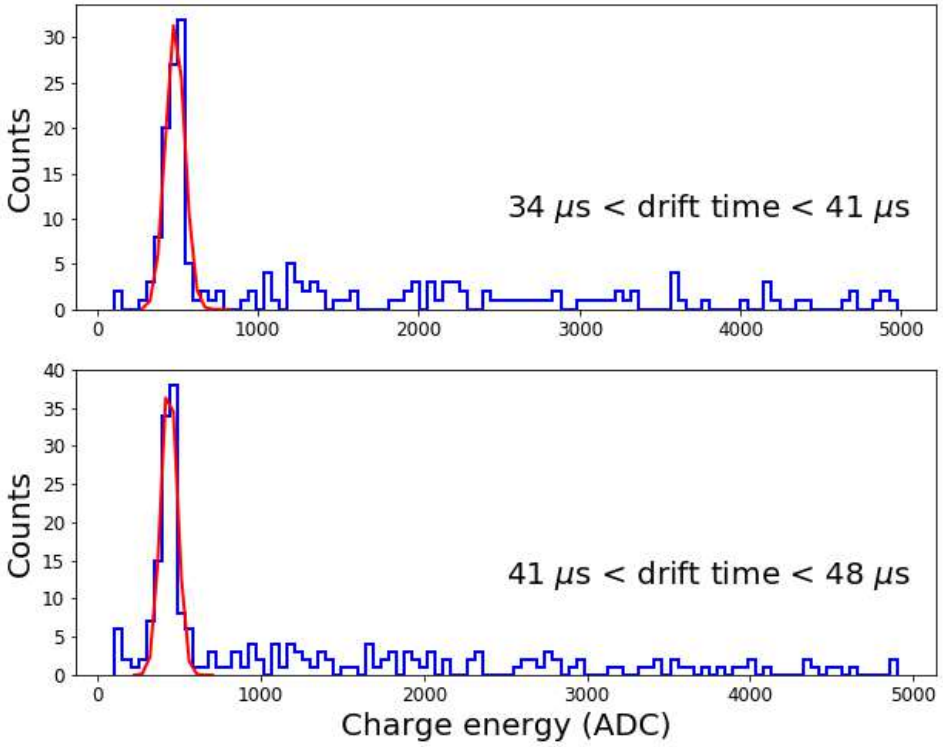

FIGURE A.1: This figure depicts a Gaussian fit to extract the peak centroid.

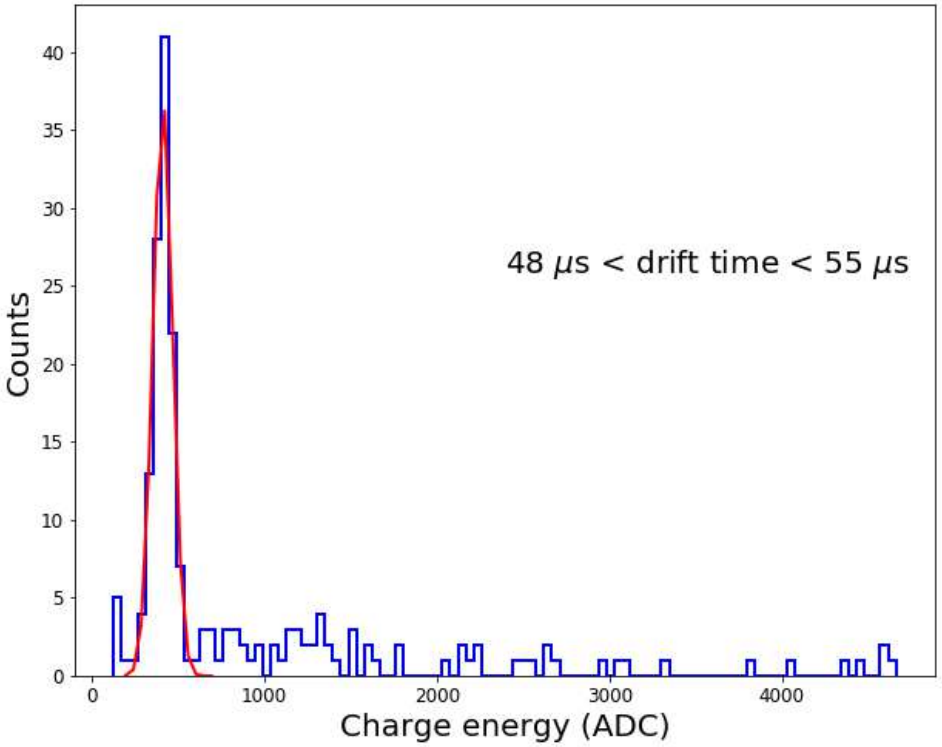

FIGURE A.2: This figure depicts a Gaussian fit to extract the peak centroid.

Appendix B

Noise Measurements

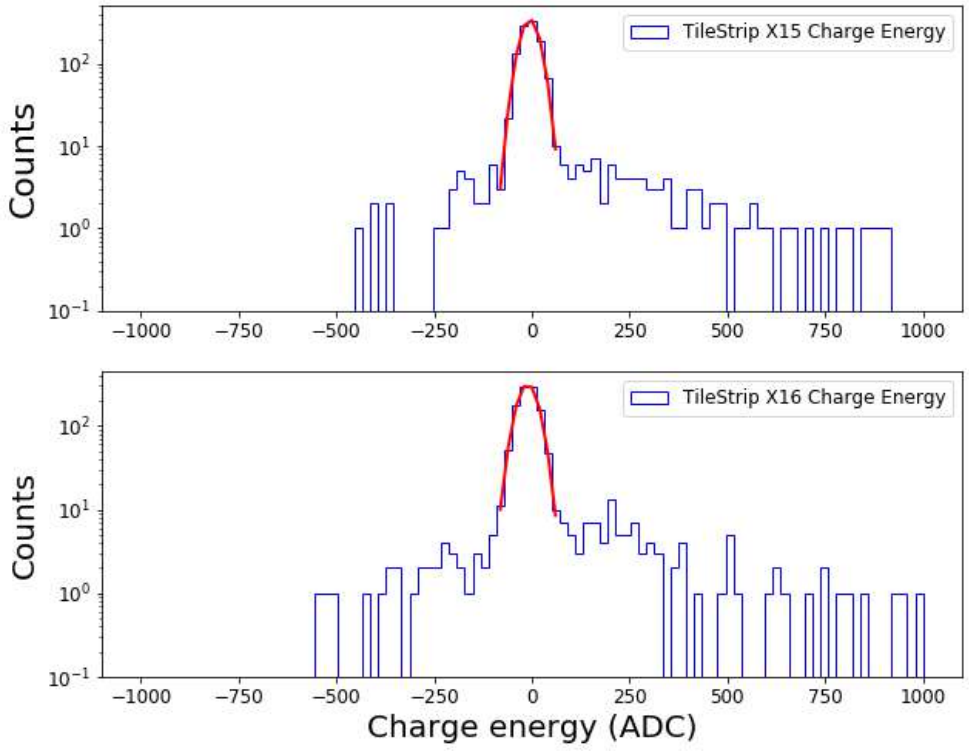

FIGURE B.1: This figure illustrates the charge energy spectrum for a single channel, with a Gaussian fit to the peak, centered at 0 ADC units.

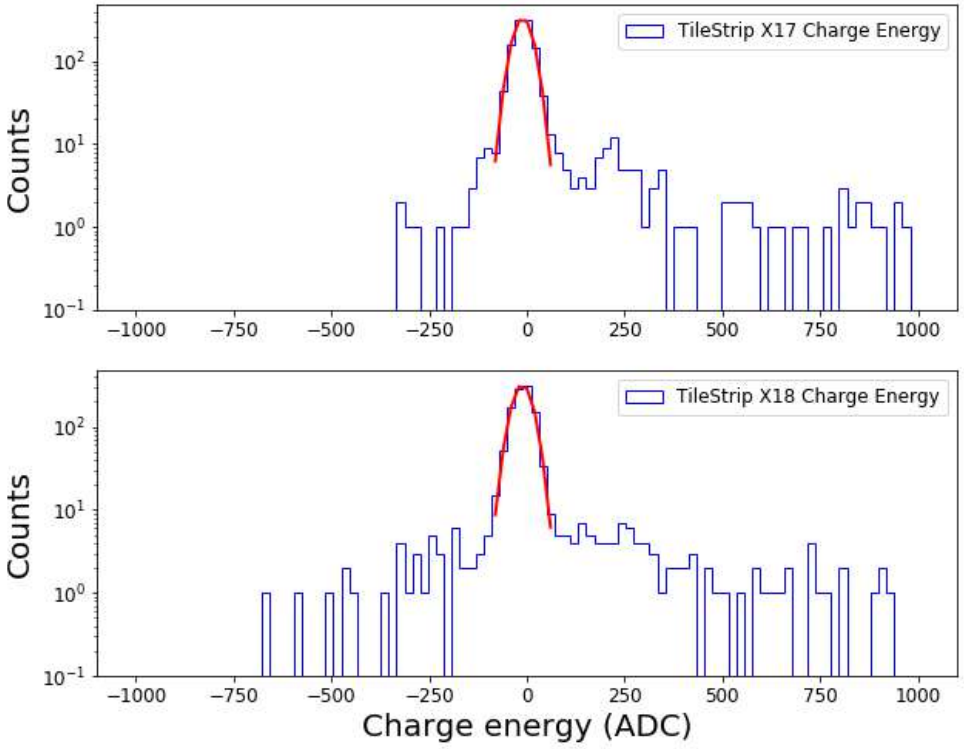

FIGURE B.2: This figure illustrates the charge energy spectrum for a single channel, with a Gaussian fit to the peak, centered at 0 ADC units.

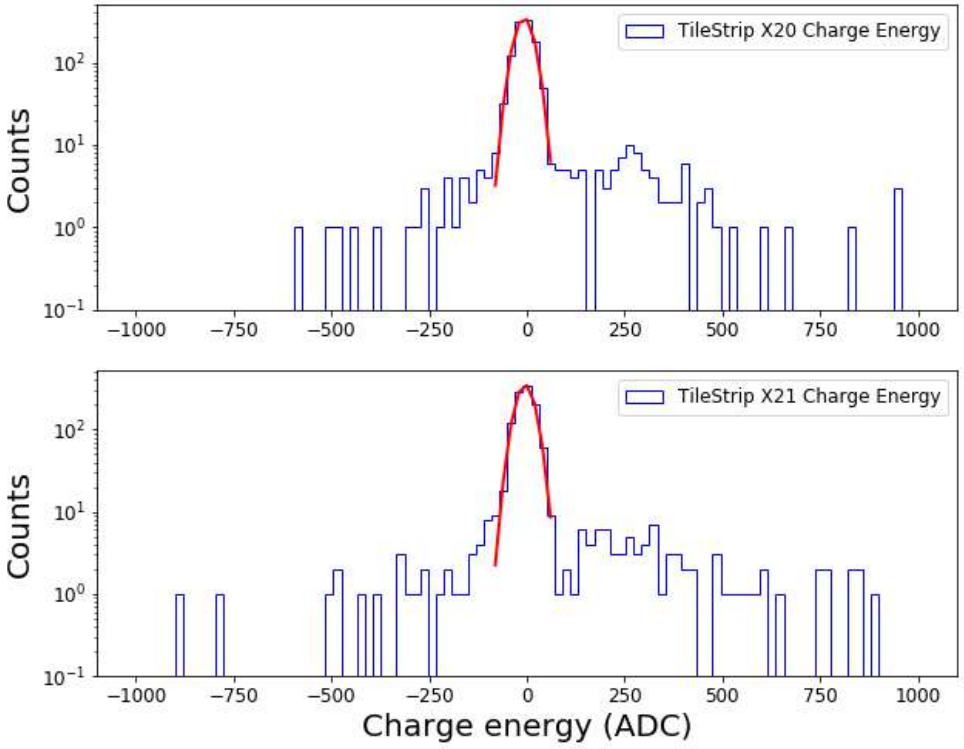

FIGURE B.3: This figure illustrates the charge energy spectrum for a single channel, with a Gaussian fit to the peak, centered at 0 ADC units.

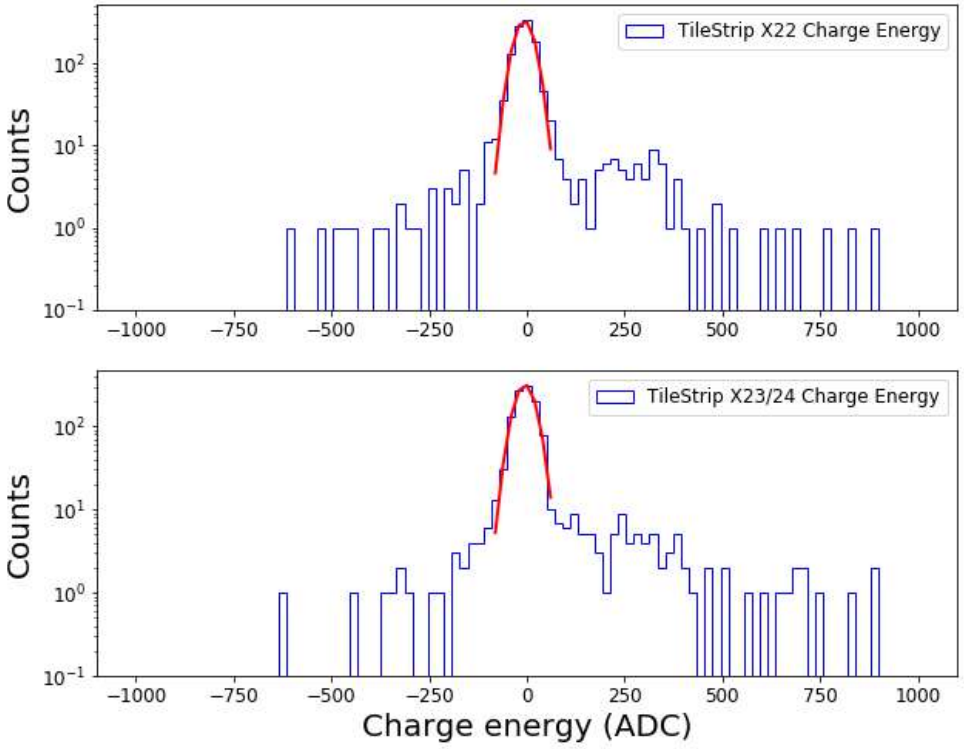

FIGURE B.4: This figure illustrates the charge energy spectrum for a single channel, with a Gaussian fit to the peak, centered at 0 ADC units.

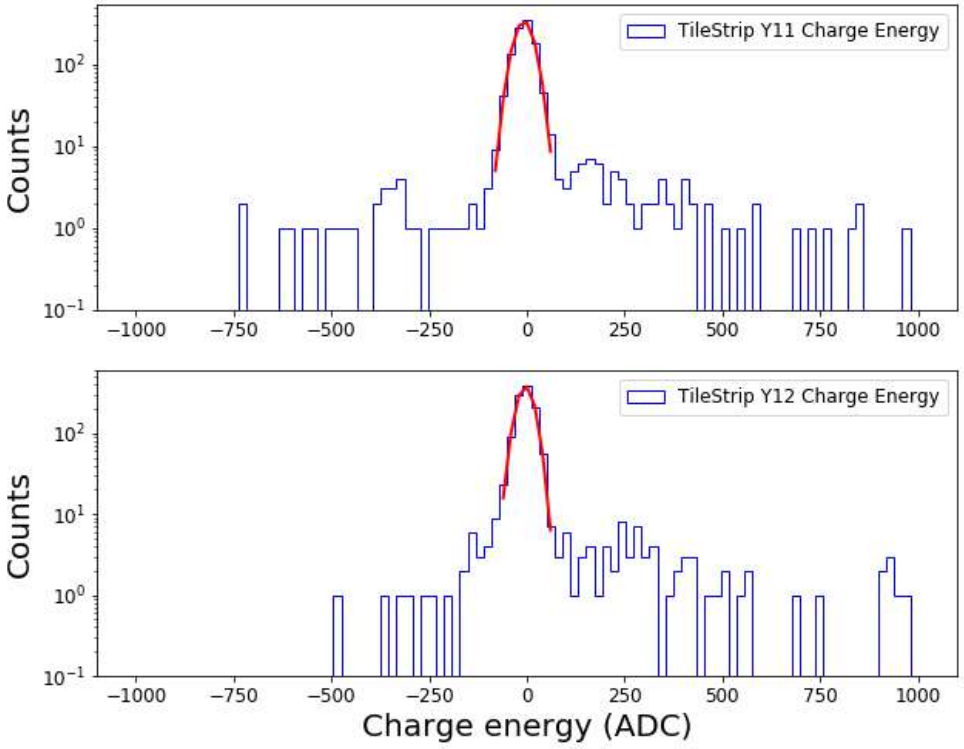

FIGURE B.5: This figure illustrates the charge energy spectrum for a single channel, with a Gaussian fit to the peak, centered at 0 ADC units.

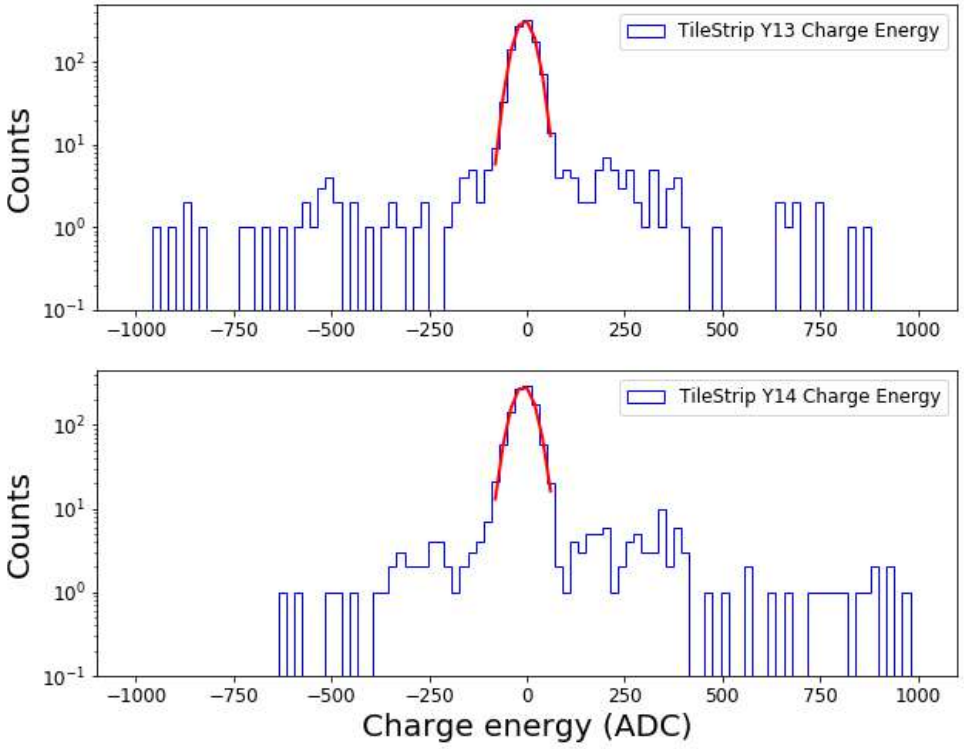

FIGURE B.6: This figure illustrates the charge energy spectrum for a single channel, with a Gaussian fit to the peak, centered at 0 ADC units.

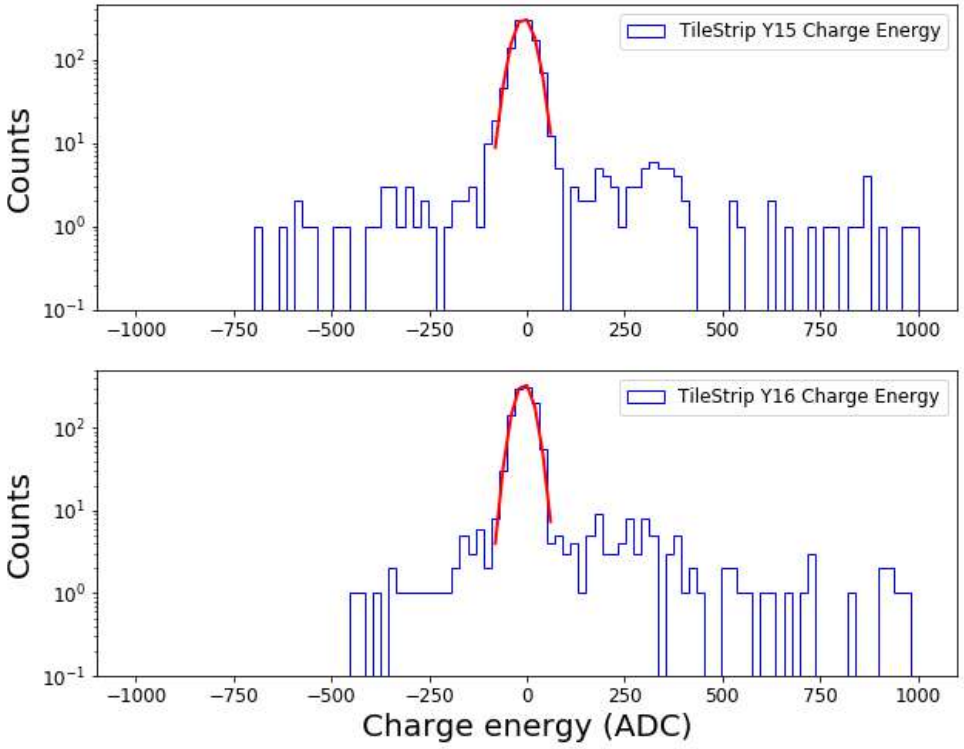

FIGURE B.7: This figure illustrates the charge energy spectrum for a single channel, with a Gaussian fit to the peak, centered at 0 ADC units.

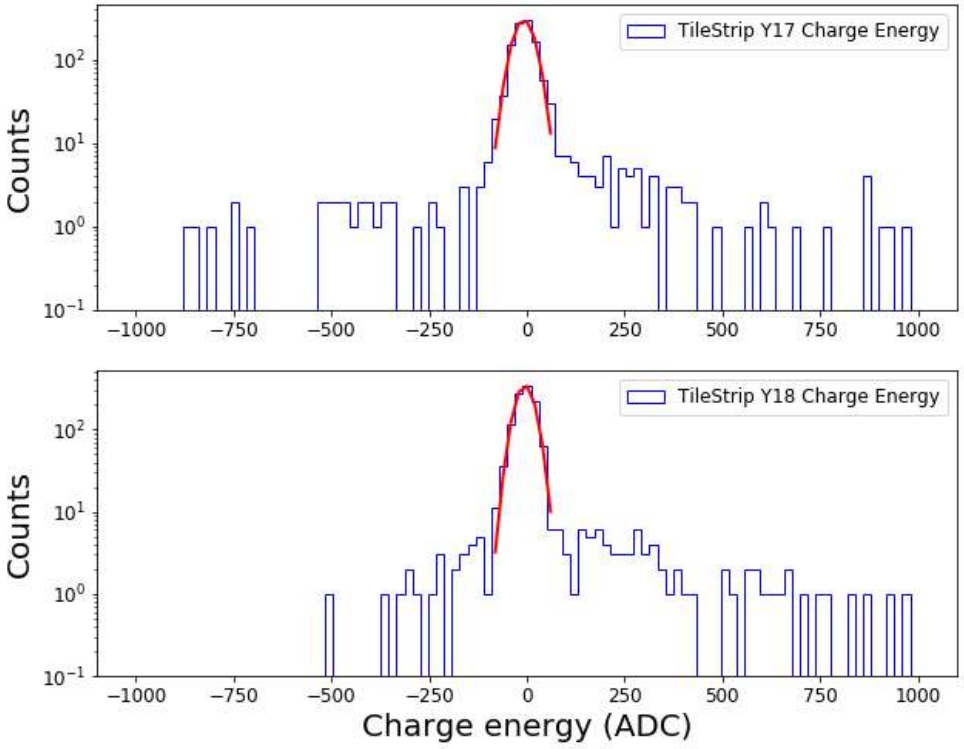

FIGURE B.8: This figure illustrates the charge energy spectrum for a single channel, with a Gaussian fit to the peak, centered at 0 ADC units.

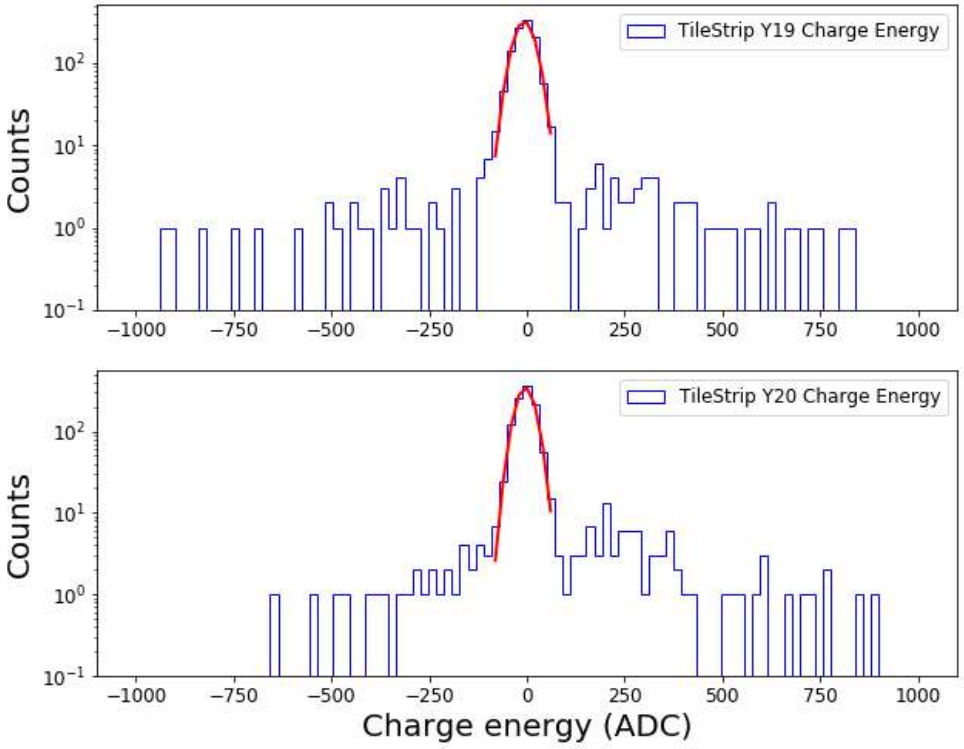

FIGURE B.9: This figure illustrates the charge energy spectrum for a single channel, with a Gaussian fit to the peak, centered at 0 ADC units.

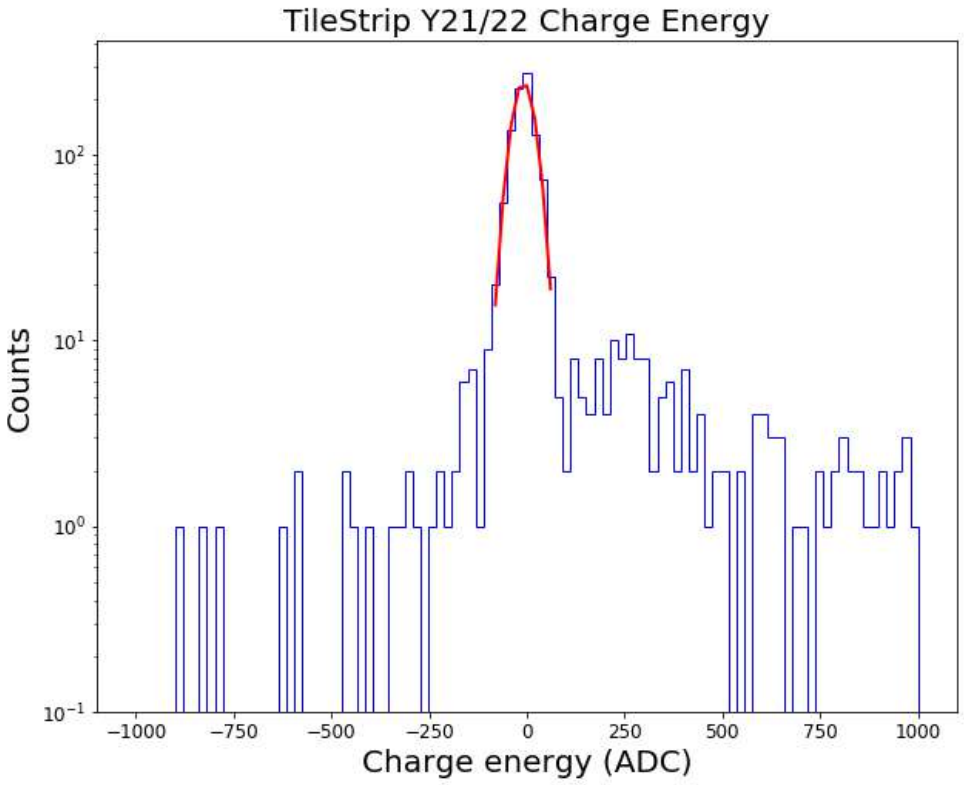

FIGURE B.10: This figure illustrates the charge energy spectrum for a single channel, with a Gaussian fit to the peak, centered at 0 ADC units.

Bibliography

[1] F. Halzen and A. D. Martin. *Quark & Leptons: An introductory course in modern particle physics*. John Wiley & Sons, 2008.

[2] C. D. Ellis and W. A. Wooster. The average energy of disintegration of radium E. *Proceedings of the Royal Society of London. Series A, Containing Papers of a Mathematical and Physical Character*, 117(776):109–123, 1927.

[3] E. M. Henley and A. Garcia. *Subatomic Physics*. World Scientific Publishing Company, 2008.

[4] M. Goldhaber, L. Grodzins, and A. W. Sunyar. Helicity of neutrinos. *Physical review*, 109(3):1015, 1958.

[5] J. N. Bahcall. Gallium solar neutrino experiments: Absorption cross sections, neutrino spectra, and predicted event rates. *Physical Review C*, 56(6):3391, 1997.

[6] J. N. Abdurashitov, V. N. Gavrin, V. V. Gorbachev, et al. Measurement of the solar neutrino capture rate with gallium metal. III. Results for the 2002–2007 data-taking period. *Physical Review C*, 80(1):015807, 2009.

[7] Y. Fukuda, T Hayakawa, E Ichihara, et al. Evidence for oscillation of atmospheric neutrinos. *Physical review letters*, 81(8):1562, 1998.

[8] T. Araki, K Eguchi, S Enomoto, et al. Measurement of neutrino oscillation with KamLAND: Evidence of spectral distortion. *Physical review letters*, 94(8):081801, 2005.

[9] Q.R. Ahmad, R.C. Allen, T.C. Andersen, et al. Measurement of the Rate of $\nu_e + d \rightarrow p + p + e^-$ Interactions produced by ^{8}B Solar Neutrinos at the Sudbury Neutrino Observatory. *Physical Review Letters*, 87(7), 2001.

[10] F.P. An, A.B. Balantekin, H.R. Band, et al. Spectral measurement of electron antineutrino oscillation amplitude and frequency at Daya Bay. *Physical review letters*, 112(6):061801, 2014.

[11] S. Gariazzo, M. Archidiacono, P. F. de Salas, et al. Neutrino masses and their ordering: Global Data, Priors and Models. *Journal of Cosmology and Astroparticle Physics*, 2018(03):011, 2018.

[12] J. Pade. Neutrino Oscillations. *Quantum Mechanics for Pedestrians 1: Fundamentals*, pages 99–108, 2018.

[13] K. N. Abazajian, M. A. Acero, S. K. Agarwalla, et al. Light sterile neutrinos: a white paper. *arXiv preprint arXiv:1204.5379*, 2012.

[14] M. A. Acero, P. Adamson, L. Aliaga, et al. First measurement of neutrino oscillation parameters using neutrinos and antineutrinos by NOvA. *Physical review letters*, 123 (15):151803, 2019.

[15] M. G. Inghram and J. H. Reynolds. Double beta-decay of ^{130}Te. *Physical Review*, 78(6):822, 1950.

[16] S. R. Elliott, A. A. Hahn, and M. K. Moe. Direct evidence for two-neutrino double-beta decay in ^{82}Se. *Physical Review Letters*, 59(18):2020, 1987.

[17] M. Moe. The first direct observation of double-beta decay. *Annual Review of Nuclear and Particle Science*, 64:247–267, 2014.

[18] R. Saakyan. Two-neutrino double-beta decay. *Annual Review of Nuclear and Particle Science*, 63:503–529, 2013.

[19] M. J. Dolinski, A. W. P. Poon, and W. Rodejohann. Neutrinoless double-beta decay: status and prospects. *Annual Review of Nuclear and Particle Science*, 69: 219–251, 2019.

[20] D. Fudenberg. *Improved discrimination for neutrinoless double beta decay searches with EXO-200 and nEXO*. PhD thesis, Stanford University, 2018.

[21] F.T. Avignone III, S.R. Elliott, and J. Engel. Double beta decay, Majorana neutrinos, and neutrino mass. *Reviews of Modern Physics*, 80(2):481–516, 2008.

[22] M. Agostini, G. Benato, J. Detwiler, et al. Toward the discovery of matter creation with neutrinoless $\beta\beta$ decay. *Reviews of Modern Physics*, 95(2):025002, 2023.

[23] S. Al Kharusi, A. Alamre, J. B. Albert, et al. nEXO pre-conceptual design report. *arXiv preprint arXiv:1805.11142*, 2018.

[24] G. Adhikari, S. Al Kharusi, E. Angelico, et al. nEXO: neutrinoless double beta decay search beyond 10^{28} year half-life sensitivity. *Journal of Physics G: Nuclear and Particle Physics*, 49(1):015104, 2021.

[25] G. Anton, I. Badhrees, P. S. Barbeau, et al. Search for neutrinoless double-β decay with the complete EXO-200 dataset. *Physical review letters*, 123(16):161802, 2019.

[26] E. Caden, P. Gorel, I. Lawson, et al. SNOLAB: The deepest clean lab in the world. *CERN Courier*, 58:20–26, 2018.

[27] S. R. Elliott and P. Vogel. DOUBLE BETA DECAY. *Annual Review of Nuclear and Particle Science*, 52(1):115–151, 2002. doi: 10.1146/annurev.nucl.52.050102.090641. URL https://doi.org/10.1146/annurev.nucl.52.050102.090641.

[28] E. Aprile and T. Doke. Liquid xenon detectors for particle physics and astrophysics. *Reviews of Modern Physics*, 82(3):2053, 2010.

[29] W. Shockley. Currents to conductors induced by a moving point charge. *Journal of applied physics*, 9(10):635–636, 1938.

[30] J. B. Albert, G. Anton, I. J. Arnquist, et al. Sensitivity and discovery potential of the proposed nEXO experiment to neutrinoless double-β decay. *Physical Review C*, 97(6):065503, 2018.

[31] D. S. Leonard, P. Grinberg, P. Weber, et al. Systematic study of trace radioactive impurities in candidate construction materials for EXO-200. *Nuclear Instruments and Methods in Physics Research Section A: Accelerators, Spectrometers, Detectors and Associated Equipment*, 591(3):490–509, 2008.

[32] E. Conti, R. DeVoe, G. Gratta, et al. Correlated fluctuations between luminescence and ionization in liquid xenon. *Physical Review B*, 68(5):054201, 2003.

[33] E. Aprile, K. L. Giboni, P. Majewski, et al. Observation of anticorrelation between scintillation and ionization for MeV gamma rays in liquid xenon. *Physical Review B*, 76(1):014115, 2007.

[34] E. Aprile, J. Aalbers, F. Agostini, et al. Energy resolution and linearity of XENON1T in the MeV energy range. *The European Physical Journal C*, 80:1–9, 2020.

[35] S Abe, S Asami, M Eizuka, et al. Search for the Majorana nature of neutrinos in the inverted mass ordering region with KamLAND-Zen. *Physical Review Letters*, 130(5):051801, 2023.

[36] A. Avasthi, T.W. Bowyer, C. Bray, et al. Kiloton-scale xenon detectors for neutrinoless double beta decay and other new physics searches. *Physical Review D*, 104 (11):112007, 2021.

[37] B. G. Lenardo, C. A. Hardy, R. H. M. Tsang, et al. Development of a ^{127}Xe calibration source for nEXO. *Journal of Instrumentation*, 17(07):P07028, 2022.

[38] R. Neilson, F. LePort, A. Pocar, et al. Characterization of large area APDs for the EXO-200 detector. *Nuclear Instruments and Methods in Physics Research Section A: Accelerators, Spectrometers, Detectors and Associated Equipment*, 608(1):68–75, 2009.

[39] M. Jewell, A. Schubert, W. R. Cen, et al. Characterization of an ionization readout tile for nEXO. *Journal of Instrumentation*, 13(01):P01006, 2018.

[40] J. Dalmasson. *Large detectors for rare searches*. PhD thesis, Stanford University, 2023.

[41] L. Fabris, N. W. Madden, and H. Yaver. A fast, compact solution for low noise charge preamplifiers. *Nuclear Instruments and Methods in Physics Research Section A: Accelerators, Spectrometers, Detectors and Associated Equipment*, 424(2-3):545–551, 1999.

[42] R. F. Lang, A. Brown, E. Brown, et al. A ^{220}Rn source for the calibration of low-background experiments. *Journal of Instrumentation*, 11(04):P04004, 2016.

[43] S. Tokonami. Characteristics of thoron (^{220}Rn) and its progeny in the indoor environment. *International Journal of Environmental Research and Public Health*, 17 (23):8769, 2020.

[44] E. V. Hansen. *Radon Injection for Light Response Calibration of the nEXO Detector*. PhD thesis, Drexel University, 2019.

[45] O. Njoya, T. Tsang, M. Tarka, et al. Measurements of electron transport in liquid and gas Xenon using a laser-driven photocathode. *Nuclear Instruments and Methods in Physics Research Section A: Accelerators, Spectrometers, Detectors and Associated Equipment*, 972:163965, 2020.

[46] E. Aprile, R. Mukherjee, and M. Suzuki. Ionization of liquid xenon by ^{241}Am and ^{210}Po alpha particles. *Nuclear Instruments and Methods in Physics Research Section A: Accelerators, Spectrometers, Detectors and Associated Equipment*, 307 (1):119–125, 1991.

[47] M. Szydagis, N. Barry, K. Kazkaz, et al. NEST: A comprehensive model for scintillation yield in liquid xenon. *Journal of Instrumentation*, 6(10):P10002, 2011.

[48] M. Szydagis, A. Fyhrie, D. Thorngren, et al. Enhancement of NEST capabilities for simulating low-energy recoils in liquid xenon. *Journal of Instrumentation*, 8(10): C10003, 2013.

[49] B. G. Lenardo, K. Kazkaz, A. Manalaysay, et al. A global analysis of light and charge yields in liquid xenon. *IEEE Transactions on Nuclear Science*, 62(6):3387–3396, 2015.

[50] S. Stephenson, J. Haefner, Q. Lin, et al. MiX: A position sensitive dual-phase liquid xenon detector. *Journal of Instrumentation*, 10(10):P10040, 2015.

[51] Q. Lin, J. Fei, F. Gao, et al. Scintillation and ionization responses of liquid xenon to low energy electronic and nuclear recoils at drift fields from 236 V/cm to 3.93 kV/cm. *Physical Review D*, 92(3):032005, 2015.

[52] D. S. Akerib, C. W. Akerlof, A. Alqahtani, et al. Simulations of events for the LUX-ZEPLIN (LZ) dark matter experiment. *Astroparticle Physics*, 125:102480, 2021.

[53] S. Agostinelli, J. Allison, K. Amako, et al. GEANT4 – A simulation toolkit. *Nuclear Instruments and Methods in Physics Research Section A: Accelerators, Spectrometers, Detectors and Associated Equipment*, 506(3):250–303, 2003.

[54] J. Allison, K. Amako, J. E. A. Apostolakis, et al. GEANT4 developments and applications. *IEEE Transactions on nuclear science*, 53(1):270–278, 2006.

[55] R. Brun and F. Rademakers. ROOT – An object oriented data analysis framework. *Nuclear Instruments and Methods in Physics Research Section A: Accelerators, Spectrometers, Detectors and Associated Equipment*, 389(1-2):81–86, 1997.

[56] Nudat3. ^{212}Bi α decay scheme, 2024. URL https://www.nndc.bnl.gov/nudat3/.

[57] G. E. P. Box and M. E. Muller. A note on the generation of random normal deviates. *The Annals of Mathematical Statistics*, 29(2):610–611, 1958.